Osaka University Knowledge Archive

Title	シリコン単結晶中の不純物および熱処理誘起欠陥の励起子発光に関する研究
Author(s)	中山, 弘
Citation	大阪大学, 1981, 博士論文
Version Type	VoR
URL	https://hdl.handle.net/11094/1982
rights	
Note	

Osaka University Knowledge Archive : OUKA

https://ir.library.osaka-u.ac.jp/

Osaka University

EXCITON LUMINESCENCE OF IMPURITIES AND THERMALLY INDUCED DEFECTS IN CRYSTALLINE SILICON

Hiroshi NAKAYAMA

EXCITON LUMINESCENCE OF IMPURITIES AND THERMALLY INDUCED DEFECTS IN CRYSTALLINE SILICON

Hiroshi NAKAYAMA

February, 1981

Osaka University
Faculty of Engineering Science
Toyonaka, Osaka

EXCITON LUMINESCENCE OF IMPURITIES AND THERMALLY INDUCED DEFECTS IN CRYSTALLINE SILICON

Hiroshi NAKAYAMA

Department of Electrical Engineering
Faculty of Engineering Science
Osaka University, Toyonaka, Osaka

February, 1981

ABSTRACT

Exciton luminescence due to impurities and thermally induced defects has been investigated in this thesis work. As concerns shallow impurities in silicon, the luminescence due to bound multiexciton complexes related to phosphorus, boron and lithium impurities has been studied with particular emphasis on their dynamical behaviors. We have proposed a model for the exciton-capture and Auger-recombination processes of bound multiexciton complexes in terms of the shell structure for these impurity species. Based on the coupled rate equations taking into account the exciton-capture and Auger-recombination processes of bound excitons and bound multiexciton complexes, the luminescence intensity of bound multiexciton complexes has been theoretically analyzed as a function of impurity concentration, photoexcitation intensity and time in the transient decay phenomena. As a result, it has been found that

the excitation, impurity concentration and transient decay behaviors of bound multiexciton luminescence observed for Si:P, Si:B and Si:Li are well explained in the framework of the proposed coupled rate equations. Combining the theoretical formula and the systematic experimental data of excitation-level and impurity-content dependence of the bound multiexciton luminescence intensity, the exciton-capture and Auger-recombination rates in phosphorus-, lithium- and boron-bound multiexciton complexes have been obtained for the first time. It has been found that the values of exciton-capture and Auger-recombination rates are closely related to the shell structure of these impurity species.

For the purpose of developing a photoluminescence characterization method for a small amount of impurities and heat-treatment induced defects in crystalline silicon used in LSI technology, several material characterization studies have been performed. In this work, we have succeeded in developing a new photoluminescence method to estimate a small amount of impurity contents and the dopant compensation ratio in high-purity silicon. Thermally induced defects in silicon crystals annealed at low temperatures around 400-600 °C have been also investigated. It has been found that photoluminescence spectra of annealed silicon crystals strongly depend on the contents of residual oxygen and carbon impurities involved in the as-grown crystals. Many sharp luminescence lines having the nature of the exciton luminescence due to an isoelectronic trap have been observed for annealed carbon-rich CZ-silicon, suggesting the existence of an isoelectronic trap related to carbon-oxygen associates. Through this thesis work, it has been found that photoluminescence spectroscopy is very promising for the characterization of impurities and defects in silicon crystals used in LSI technology as well as for exciton physics.

ACKNOWLEDGEMENT

The author would like to express his sincere thanks to Professor Y. Hamakawa for his kind advice and critical reading of this thesis. The author wishes to make his deep acknowledgement to Professors S. Namba, T. Makimoto, K. Fujisawa and T. Sueta for their kind guidance in the course of this study at Osaka University.

This work has been done at Semiconductor Laboratory, Faculty of Engineering Sience, Osaka University, Toyonaka, Osaka, under the direction of Professors Y. Hamakawa and T. Nishino. In particular, the author is much indebted to Professor Y. Hamakawa for his valuable and kind teaching, advice and encouragement throughout the course of this work. The author also wants to express his greatest thanks to Professor T. Nishino for his constant teaching, advice and encouragement throughout the course of this study and for the critical reading of this thesis. Professor T. Nishino kindly pointed out the importance of studies for the dynamical behaviors of bound multiexciton complexes and suggested the significance of material characterization utilizing photoluminescence techniques.

The author wishes to give his highest appreciation to Professor K. Cho for his useful teaching and discussion on exciton physics and his interest in our work and also to Professor M. Umeno and Mr. K. Yasutake for their useful discussion and advice on characterization studies of crystalline silicon. Thanks are also due to Professors S. Narita and Y. Nishida and Dr. M. Taniguchi for their kind teaching and discussion on impurity physics in silicon.

The author is much indebted to Dr. M. Okuyama and Dr. H. Takakura for their useful advice and discussion throughout the course of this study and also to Mr. C. Sada and Mr. H. Ohnish for their kind advice and encouragement during this thesis work.

Usual and enjoyable discussions with colleagues of the Semiconductor Laboratory, especially, Dr. H. Okamoto, Mr. Y. Yamazoe, Mr. K. Okamoto, Mr. Y. Matsui and Mr. S. Nonomura are much appreciated.

The author wishes to express his gratitude to his co-workers in the Semiconductor Laboratory , Mr. H. Sawada and Mr. K. Ohnishi for their valuable discussion and skillful technical assistance on the study of bound multiexciton luminescence and also to Mr. J. Katsura and Mr. K. Hatasako for their useful discussion and thechnical assistance on the material characterization study for crystalline silicon. Thanks are also due to Mr. Y. Sasai, Mr. Y. Matsui and Mr. H. Akiyama for their skillful assistance in the electrical measurements such as Hall effect and DLTS.

The author gratefully thanks Dr. T. Hasebe of Fukushima University and Mr. K. Takarabe of Okayama College of Science for their valuable and endless encouragement.

Finally, the author wishes to thank his wife and parents, and all his family for their endless encouragement and support.

TABLE OF CONTENTS

CHAPTER		Page
I.	INTRODUCTION	1
II.	BOUND MULTIEXCITON LUMINESCENCE IN SILICON	8
	II-1. free- and bound-exciton states in semiconductors	8
	II-2. bound multiexciton complexes in silicon	13
	II-3. experimental apparatus	17
	II-4. impurity-concentration dependence	19
	II-5. excitation-level dependence	25
III.	ANALYSIS OF BOUND MULTIEXCITON LUMINESCENCE INTENSITY	34
	III-1. a model for the formation and decay kinetics	34
	III-2. a method of determining exciton-capture and Auger-recombination rates	41
	III-3. exciton-capture and Auger-recombination rates of phosphorus, boron and lithium BMEC	44
	III-4. transient decay behaviors	53
	III-5. exciton-capture cross section at a neutral impurity	57
IV.	PHOTOLUMINESCENCE METHOD OF ESTIMATING IMPURITY CONTENTS AND DOPANT COMPENSATION RATIO	68
	IV-1. formulation of the luminescence-intensity ratio of BE and FE	69
	IV-2. determination of parameters involved in FE and BE recombination processes	75
	IV-3. excitation-level dependence of the luminescence-intensity ratio of BE to FE	76

IV-4. photoluminescence characterization of dopant impurity contents in silicon 82

IV-5. effects of dopant compensation 83

V. CHARACTERIZATION OF THERMALLY IMDUCED DEFECTS IN SILICON 90

V-1. procedures of thermal annealing and Hall-effect measurements 91

V-2. Hall-effect analysis of thermally induced oxygen donors 92

V-3. photoluminescence observation of oxygen donor states . 98

V-4. thermally induced luminescent centers 103

V-5. sharp luminescence lines of carbon-rich CZ-silicon ... 106

V-6. evidence for an isoelectronic luminescence center in silicon 113

VI. CONCLUSIONS 117

APPENDIX 122

REFERENCES 124

CHAPTER I

INTRODUCTION

Recent progress in the field of solid state spectroscopy has brought about a great deal of developments in both fundamental solid state physics and material characterization for semiconductor electronics. A part of this progress in solid state spectroscopy has been achieved by the appearance of various kinds of experimental techniques using high-power lasers operating in cw or pulse modes, high-resolution spectrometers, computer-controlled signal-processing systems and so on. Another part of the progress has been performed cooperatively with the advance in crystal-growth technology, which is closely related to recently developed various types of opto-electronic and LSI devices.

In connection with such circumstances, exciton physics in silicon has been greatly advanced in this decade, resulting in several new fields of exciton physics. The first topic is concerned with the high-density exciton system [1] induced by an intense photoexcitation using high-power lasers with a photon energy greater than the fundamental energy gap. In the photoexcited states of a crystal, excited carriers (electrons and holes) relax rapidly to the band extrema, emitting phonons. At low temperatures around liquid helium temperature, a free electron and a free hole are mutually attracted to form an exciton. Excitons in indirect-gap semiconductors such as silicon and germanium have the relatively long lifetime, about a few micro-seconds, and form the insulating exciton-gas phase in the photoexcited crystal. At more intense excitation levels, excitons begin to interact each other, resulting in the other

completely new phase of high-density exciton through a characteristic phase transition.

The idea of such a transition was proposed by Keldysh in 1968 at the Moscow conference on the physics of semiconductors[2]. He proposed that the insulating exciton gas condenses into a metalic electron-hole liquid (EHL) state under extremely high photoexcitation levels. At the intermediate excitation levels, the exciton gas and the spatially distributed condensate EHL phase (namely, electron-hole drops (EHD)) coexist in the crystal. Since then, extensive theoretical and experimental works have been achieved so as to verify the existence of the condensate phase of electron-hole system[3,4]. These works on the high-density exciton system are essentially concerned with a new type of many-body problem in solid state physics associated with the condensate phase of electrons and holes having finite lifetimes. Through these extensive studies, the existence of the EHL phase is presently well established in both elemental and compound semiconductors.

One of the recent controversial problems associated with such electron-hole condensation is the identification and classification of two types of phase transition involved in photoexcited semiconductors at low temperatures when the metalic EHL condenses from the insulating exciton gas[3,4]. One is the gas-to-liquid and the other is the insulator-to-metal (Mott) transition. Recent works on the temperature versus exciton density phase diagram of high-density exciton system by Thomas et al.[6] have shown that a separate Mott transition does not occur, but rather there appears a substantial distortion of the phase diagram from that of the simple gas-liquid phase transition near the top of the phase diagram, which is referred to as Mott distortion by them. However, this problem

still remains to be resolved in future investigations.

Another topic studied extensively during this decade in the field of exciton physics is the so-called bound multiexciton complexes (BMEC) problem concerned with the origin of newly observed satellite line series of well-known bound-exciton luminescence lines[7,8], which is one of the subjects of this thesis work. One of the controversial BMEC problem is concerned with the energetic stability of BMEC state having many excitons bound at an impurity center[9-11]. Another is associated with the difficulty in the explanation of Zeeman and uniaxial stress effect data of the satellite luminescence line series in the framework of BMEC model[12,13]. Namely, under either magnetic fields or uniaxial stress, such satellite luminescence lines split into several components with the identical behavior as the principal bound excitons.

The latter problem is presently well resolved [10,14] on the basis of the so-called shell model of BMEC proposed by Kirczenow [15] to describe the electronic structure of BMEC. As for the former problem, several theoretical considerations on the exciton-binding energy of BMEC have been carried out, [16-19] the results showing that correlation effects in the many-particle BMEC system contribute essentially to the energetic stability of BMEC and also the formation of such stable multi-exciton complexes bound to impurities should be a general phenomenon in semiconductors with degenerate band edges[17]. The calculated exciton-binding energy of the m-th BMEC (m is the number of localized excitons in BMEC and referred to as the order) increases with m and tends towards that of EHL for large m [17], which is consistent with experimental observations[11].

On the other hand, dynamical behaviors such as exciton-capture

(EC), Auger-recombination (AR), thermal dissociation processes associated with the BMEC system, which is the system composed of many electrons and holes localized around an impurity center with the high local density, have remained so far unknown for the most part in the theoretical and experimental aspects. In this thesis work, we have concentrated on investigations of such dynamical behaviors of BMEC[20-22]. Present works on the subject are constructed as follows. First, we propose a model for the EC and AR processes of bound exciton (BE) and BMEC considering the shell structure model. Second, the densities of BMEC in the photoexcited states of a crystal are theoretically analyzed as a function of photoexcitation intensity (namely, exciton-generation rate), impurity concentration and time (in the transient decay behavior) based on the rate equations taking into account EC and AR processes of the whole system consisting of neutral impurity center, free exciton (FE), BE and BMEC. Third, combining these theoretical considerations with systematic experimental data on the excitation-level and impurity-content dependences of the BMEC luminescence intensity, in phosphorus-, lithium- and boron-doped silicon, we determine some recombination parameters involved in the dynamical processes of BMEC. Finally, we discuss the dependence of such parameters, EC and AR rates, on the order m of BMEC in terms of the shell structure model for these impurity species[15].

In this decade, a great progress has been accomplished in the field of silicon LSI technology using high purity and dislocation-free single-crystal silicon wafers. To get further progress towards more advanced VLSI devices, nearly perfect silicon crystal wafers with large diameter are needed. For this purpose, the characterization and elimination of crystal defects in silicon introduced during both crystal-growth and

device fabrication processes are considered to be quite important[23,24]. In such viewpoint, optical characterization techniques such as the photoluminescence method are quite promissing because of the inherently high sensitivity to a small amount of impurities, especially electrically active shallow impurities and defects[25,26]. In this thesis work, we have performed several material characterization studies for dopant and residual impurities contained in as-grown silicon crystals[27] and also for heat-treatment induced defects[28-30]. In this study, as an application of the analysis method for the exciton luminescence intensity concerned with BMEC problems, we have succeeded in developing a new photoluminescence method to characterize the contents of a small amount of impurities and dopant compensation ratio in high-purity silicon[27].

This thesis is constructed as follows. In chapter II we first review the excitonic states in silicon with emphasis on the BMEC states. Basic experimental data of impurity-concentration and excitation-level dependence of FE, BE and BMEC luminescence are described in the next. In the low impurity concentration range below 10^{16} cm^{-3}, the exciton-luminescence spectrum is dominated by the sharp luminescence lines of FE, BE and BMEC , and their impurity-content and excitation behaviors are explained by the kinetics model proposed here. In contrast, at the high doping levels beyond 10^{17} cm^{-3}, such luminescence lines come to disappear and anomalously broad new luminescence bands appear near the photon-energy range of BMEC. In such high doping range, an inter-impurity interaction seems to play an important role in the excitonic states. In chapter III, we present a model for the formation and decay kinetics of FE, BE and BMEC. Based on the model, we theoretically calculate the FE, BE and BMEC densities, namely their luminescence

intensities, as a function of excitation level, impurity concentration and time. Combining the theoretical results with systematic experimental data on the excitation-level and impurity-content dependence of BMEC luminescence intensities, the EC and AR rates of BMEC in phosphorus-, lithium- and boron-doped silicon are determined. Theoretical calculations on the EC rate (EC cross section) at a neutral impurity center as a function of temperature, taking into account an exciton-acoustic phonon interaction, are also presented in the last part of this chapter.

In chapter IV, we describe a photoluminescence method of estimating a small amount of impurity content and the compensation ratio in high-purity silicon crystal as a somewhat application-side part of this thesis work. This method is based on theoretical considerations on the excitation-level dependence of the luminescence-intensity ratio of BE to FE and also on effects of dopant compensation on the luminescence intensity ratio of BE of a majority dopant relative to FE. Experimental data on the characterization of impurity content and compensation ratio by the presently developed method are compared with results from conventional electrical measurements.

In chapter V, we demonstrate a photoluminescence characterization of thermal-annealing induced defects in silicon crystals used for LSI technology. In the present study, so-called thermally induced oxygen donor states generated by low-temperature annealing around 450 °C[31,32], whose microscopic model is not established at the present stage, have been precisely studied by photoluminescence measurements combining infrared absorption and Hall-effect measurements. In this annealing study, we have also found new sharp luminescence lines having the nature of exciton luminescence due to an isoelectronic trap in annealed carbon-

rich silicon. Effects of temperature and annealing temperature and period on the new luminescence lines are presented in the last part of this section.

Finally, some conclusions obtained in this thesis work on the exciton luminescence of impurities and thermally induced defects are summarized in the final chapter VI.

CHAPTER II

BOUND MULTIEXCITON LUMINESCENCE IN SILICON

In this chapter, an exciton state in a covalent semiconductor such as silicon is first briefly postulated, with emphasis on the recent development of theoretical and experimental investigations on the internal structure of an exciton state. Secondly, following the brief description on the bound exciton (BE) states, the electronic structure of bound multiexciton complexes (BMEC) is described in terms of the shell structure model for the BMEC states. Then, the experimental apparatus used in this work and results of impurity-content and excitation-level dependence of free exciton (FE), BE and BMEC luminescence in silicon doped with phosphorus, lithium or boron are presented and discussed with a view point of reaction kinetics of the FE, BE and BMEC system.

II-1. free- and bound-exciton states in semiconductors

An exciton state in a covalent semiconductor such as silicon is well postulated as a composite particle of an electron and a hole both of which are mutually attracted according to the screened electron-hole Coulomb interaction[33-35]. An exciton has two modes of motion, that is internal and translational motion. The internal motion of an exciton is analogous to that of a hydrogen atom composed of a proton and an electron. From this picture, the electron-hole binding energy, described here as E_x, of an exciton is written by using the hydrogen Rydberg constant R_y as follows;

$$E_x = (\mu/\kappa^2)\ R_y \quad , \tag{2.1}$$

where μ is a reduced effective mass in units of free electron mass given by $\mu^{-1} = m_e^{-1} + m_h^{-1}$. κ is a phenomenological dielectric constant of a semiconductror medium. The value of the constant κ is in principle obtained from many-body calculations of a screening effect on the electron-hole Coulomb interaction and can be approximated by the static dielectric constant of a semiconducting medium in the case of covalent semiconductros such as silicon.

Concerning the translational mode, an exciton has the translational momentum $\hbar\vec{K}$ and the corresponding kinetic energy $\hbar^2K^2/2M$, where $\vec{K}$ is a translational wave vector of an exciton and $M=m_e+m_h$ is a translational mass of an exciton. Thus, these two modes of motion result in a energy level , namely excitation energy of an exciton relative to the electronic ground state of the host semiconductor, of an exciton state in the fundamental energy gap of a semiconductor described as

$$E(n,\vec{K}) = E_g - E_x/n^2 + \hbar^2K^2/2M \quad , \tag{2.2}$$

where E_g is the fundamental energy gap of a host semiconductor and n is a hydrogenic principal quantum number of an exciton. The value of E_x in silicon is estimated to be 14.7 meV[36].

The hydrogenic picture of an exciton is indeed usuful but is not enough to recognize the full body of exciton states in real semiconductors. That is, an exciton itself possesses the other internal degrees of freedom resulting in so-called internal structure of an exciton. [37]The internal structure comes from a degeneracy of valence

and conduction bands concerned, anisotropy of electron and hole effective mass (nonparabolicity of band edges), spin and orbital angular momenta of electron and hole, and so on. In the recent few years, theoretical and experimental works on the internal structure of an exciton and its behaviors under external perturbations such as magnetic field, uniaxial stress and electric field have been extensively performed[37,38]. Especially, in the case of silicon, the so-called mass-anisotropy splitting of an exciton level has been found both experimentally[40-43] and theoretically[44,45] based on an effective-mass Hamiltonian taking into account the degeneracy of j=3/2 valence band and the anisotropy of electron effective mass.

On the other hand, an exciton forms various types of complexes with impurities and defects involved in semiconductor crystals. Such exciton (electron-hole pair) states spatially localized at an impurity and a defect site are called bound exciton (BE). In contrast, the above-mentioned exciton state having translational motion is called free exciton (FE). Some types of stable BE states were proposed and classified in the early theoretical work by Lampert[46]. In silicon, BE states localized at a neutral donor or acceptor were considered to be stable. The existence of BE related to various kinds of group-V and group-III impurities was verified in 1960s mainly by photoluminescence spectroscopy [47-49] following the theoretical prediction by Lampert. The energy level of BE, which means the excitation energy of an electron-hole pair localized at an impurity center, lies below the free-exciton energy level and given by

$$E = E_g - E_x - E_{bx} \quad , \qquad (2.3)$$

where E_{bx} is exciton-binding energy at an impurity center. The value of E_{bx} depends on impurity species and corresponds to different transition energies in the photoluminescence spectrum of BE. This enables us to identify impurity species involved in as-grown and impurity-diffused semiconductors for the purpose of material characterization[26]. The value of E_{bx} in silicon is about 5 meV for common group-III and V impurities[48].

Figure 1 illustrates FE and BE states. We express here FE state by the symbol "X" and BE state associated with a neutral impurity center by "A^0X" and "D^0X" for acceptor and donor, respectively. A^0 and D^0 denote a neutral acceptor and donor center, respectively.

In irradiated states of a semiconductor by the interband photoexcitation, generated free electron-hole pairs rapidly relax to band extrema, subsequently resulting in FE at low temperatures around liquid helium temperature. Such FE recombines radiatively in a given lifetime characteristic for the host material emitting a phonon to conserve the crystal momentum in the case of indirect-gap semiconductors such as silicon. The luminescence spectral shape of FE is a Maxwell Boltzmann type [50] reflecting the thermal distribution for the kinetic energy of excitons, which is schematically shown in the insert of Fig. 1. A part of generated excitons are captured by impurities involved in the crystal, forming BE states. Since BE is spatially localized at an impurity center and this results in the formation of extended states in k (wave vector)-space as can be seen from a kind of uncertainty principle. This nature of BE states causes a characteristic sharp luminescence line with the Gaussian spectral line shape in the low-energy side of the corresponding phonon replicas of the FE luminescence line. On the

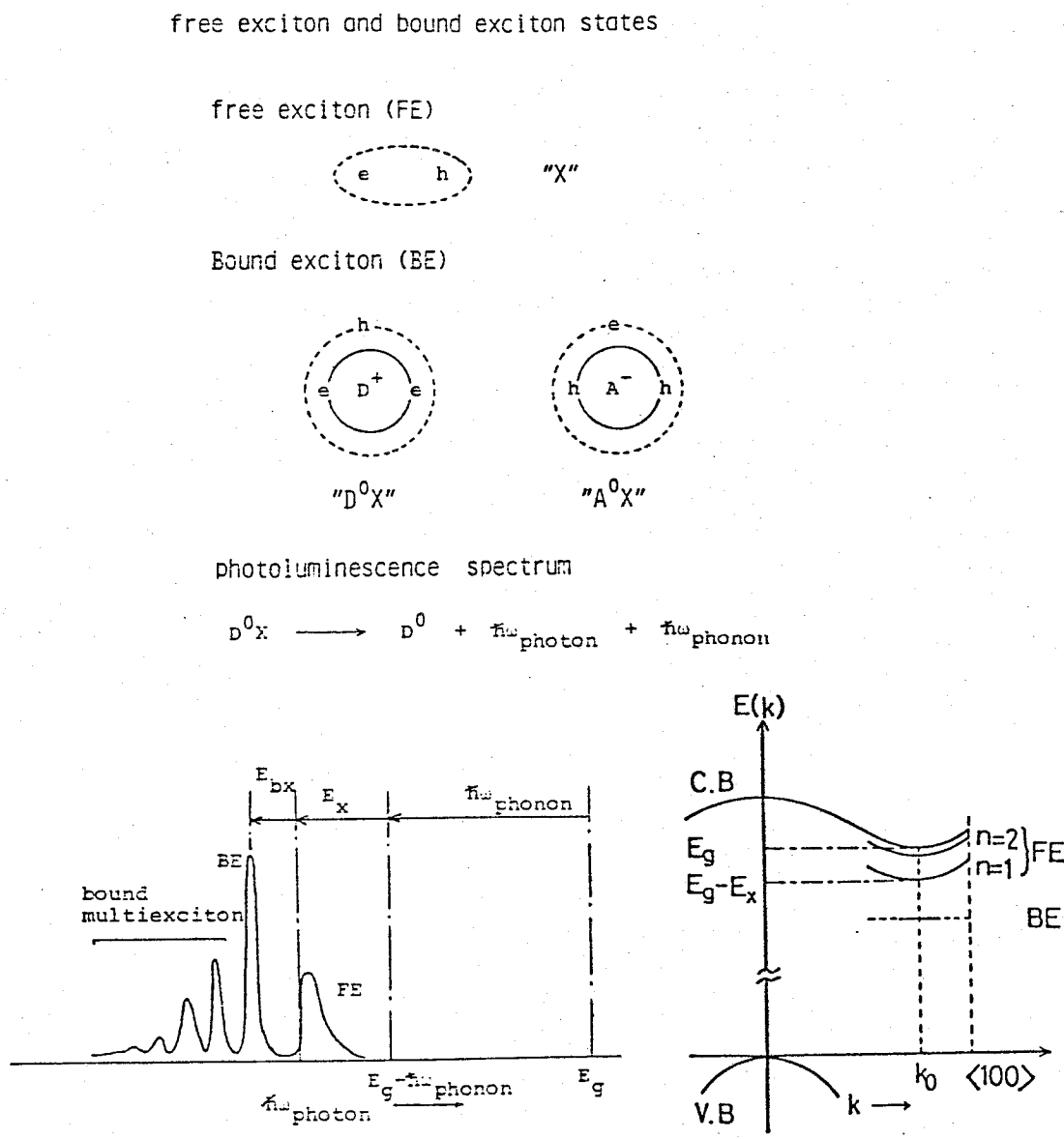

Fig. 1. A schematic representation of free- and bound-exciton states. Energy diagram (right-hand insert) and luminescence spectrum due to free exciton, bound exciton and bound multiexciton (left-hand insert) are also illustrated.

other hand, the existence of such extended states in k-space relaxes the momentum-conservation law, resulting in the occurance of so-called no-phonon recombination lines of BE.

Another significant feature of BE luminescence is the existence of satellite lines called two-electron (hole) recombination luminescence lines[48,51,52]. In this transition process, a BE radiatively recombines leaving a final neutral donor (acceptor) state in the bound excited states, in particular in the s-like even-parity excited states. The observation of two-electron (hole) satellite lines enables us to determine the s-like excited states levels, which can not be determined by the usual infrared absorption method because of the selection rule in electric dipole transitions, and further to estimate the ionization energy of the related impurity. Recently, several highly lying s-like excited states of donors and acceptors in silicon and germanium have been precisely investigated from the analysis of such two-electron (hole) satellite recombination lines[53-56].

II-2. bound multiexciton complexes in silicon

In low-temperature luminescence spectra from lightly doped silicon, a series of low-energy satellite lines of the principal BE recombination lines was first reported by Kaminskii and Pokrovskii [7,8] in their study for the nucleation phenomenon of EHL. At low-excitation levels, FE and BE luminescence lines are dominantly observed, and a series of satellite lines comes to appear as the excitation intensity increases. At more intense excitation levels, such satellite line series grow to be a broad luminescence band originated from EHL. These experimental

features led to an idea that the satellite line series are due to the formation of BMEC containing several excitons localized at an impurity center and such complexes play as a kind of nucleation center of EHD. Since then, a great deal of works has been made to verify and clarify the BMEC model. The first experimental verification of the existence of BMEC states as the origin of the satellite line series of principal BE lines was presented by Sauer [57] and Kosai and Gershenzon [58] in their detailed works on the satellite lines in phosphorus-, boron- and lithium-doped silicon.

After these works in the early stage of 1970s, [9,10,12,13,59] Kirczenow proposed the shell model of BMEC to postulate the electronic structure [15]. Through the extensive investigations [11,14,60-71] following the proposal of the shell structure model by Kirczenow, the shell model description of BMEC is presently well established to explain spectroscopic observations including Zeeman and uniaxial-stress effect data. The essential concept of the shell model [15] is that localised excitons in BMEC states lose their excitonic nature and rather each electron and hole individually occupy their one-particle impurity orbitals similarly to the atomic shell structure appeared in well-established atomic physics.

On the other hand, dynamical behaviors of BMEC having many electrons and holes localized at an impurity center have remained so far unknown for the most part. We have been studying for this few years the dynamical behaviors of BMEC system with particular emphasis on the exciton-capture (EC) and Auger-recombination (AR) processes of BMEC[20-22]. In the EC process of BMEC, several modes of process appear, reflecting the existence of several different electron and hole shells. Namely, two

types of processes can be considered; the first process in which an exciton is captured into the inner ground shell of an electron a hole leaving the resultant BMEC state in the ground stable state, and the second process in which an exciton is captured into the outer excited shell leaving BMEC in the excited shell state and the BMEC subsequently relaxes to the ground shell state.

As for the decay process of BMEC, the AR process is considered to be a quite probable and dominant recombination channel of BMEC in low temperatures around liqud helium temperature, where thermal dissociation process can be neglected, since the complexes possess many electrons and holes localized around an impurity center at the high local density and this situation is very suitable for the AR process. In the present work on the dynamical processes concerned with BMEC, we have found that the EC and AR rates strongly depend not only on the number of localized electrons and holes but also on the impurity-specific shell structure of BMEC. The detailed results are presented in this chapter and the next chapter.

Figure 2 illustrates the BMEC states associated with phosphorus, lithium and boron impurities in silicon. These impurity species are typical impurities of substitutional donor, interstitial donor and substitutional acceptor in silicon, respectively. In the shell model, the wave function of BMEC is composed by antisymmetrized products of one-electron and one-hole orbitals[15,72]. The impurity state wave function classified according to the irreducible representation of the tetrahedral symmetry group T_d concerned with the impurity site are chosen for the one-particle wave functions. In the case of substitutional phosphorus donor, the one-electron states are classified by Γ_1, Γ_3 and Γ_5 corresponding

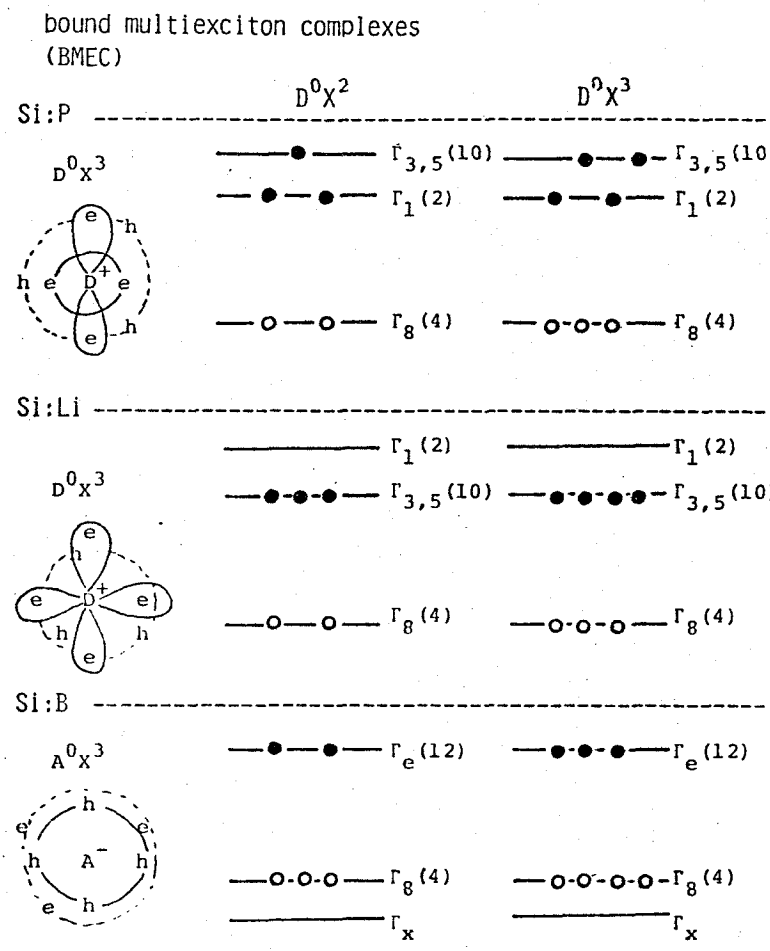

Fig. 2. A schematic representation of bound multiexciton complexes associated with phosphorus, lithium and boron in silicon. (•) indicates an electron and (o) a hole. Wave function of a bound multiexciton (third order) complexes is also illustrated, where p-like wave function schematically denotes $\Gamma_{3,5}$ electron wave function.

to the familiar symbols for the irreducible representation of T_d group. In the phosphorus neutral donor state, these one-electron states show a splitting due to so-called valley-orbit interaction, resulting in the ground Γ_1 state and the excited Γ_3 and Γ_5 states[73].

Following this order of one-electron orbitals of the neutral donor state, the one-electron wave functions of phosphorus BMEC are labelled Γ_1 for the ground state orbital and $\Gamma_{3,5}$ (this means approximately degenerate Γ_3 and Γ_5 states) for the lowest excited orbital. Considering the spin degeneracy, the Γ_1 state has two-fold and $\Gamma_{3,5}$ has ten-fold degeneracy. One-hole orbital is also labelled Γ_8 according to the irreducible representation of the j=3/2 valence band and this state has four-fold degeneracy. The lowest hole excited shell is usually referred to as Γ_x. The shell structure of BMEC D^0X^2 (A^0X^2) and D^0X^3 (A^0X^3) are illustrated in Fig. 2. In the case of interstitial lithium donor, the order of one-electron orbitals is inverted[74] from that of phosphorus BMEC, and hence the ground state orbital is ten-fold degenerate $\Gamma_{3,5}$ state. This difference in degeneracy of the ground state shell causes quite different behaviors of the BMEC luminescence between phosphorus and lithium, which will be shown in the following chapter.

II-3. experimental apparatus

Samples used in this work were commercially available silicon single crystals doped with various kinds of common group-III or V impurities. In particular, phosphorus-, boron- and lithium-doped silicon are extensively used for the present photoluminescence measurements. The

doping levels of the samples are ranging from 10^{11} to 10^{18} cm^{-3}. The samples doped with lithium are prepared as follows. Painting lithium dispersion in mineral oil, lithium impurities are diffused into a high-purity float-zone silicon crystal with the residual boron concentration of 6.5×10^{11} cm^{3}. Preheating was carried out to eliminate the oil for two hours at 200 °C and followed by diffusion of lithium for several different periods ranging from 10 minutes to several hours at 250-600 °C in a furnace with Ar ambient. After removing the sample from the furnace and cleaning the surface, the sample was heat-treated at 400-600 °C untill both surfaces of the sample show the same resistivity. By these processes we prepared lithium-doped silicon crystal in the lithium concentration ranging from 10^{13} to 10^{18} cm^{-3}. [21]

The samples used for photoluminescence measurements were lapped and soaked in hot trichloroethylene, hot aceton and hot methyl alcohol. After these soaking treatments, the sample was rinsed in deionized water and lightly etched in a solution of HNO_3 and HF. Immediately after such careful surface treatments, the sample was placed in a liquid helium optical dewar. The photoexcitation source of the present photoluminescence study was a cw mode Ar^+ laser operating at 5145 Å. The photoexcitation power was changed by using neutral-density filters as well as by controlling the laser current. Using such procedures, the excitation-intensity dependence of an exciton luminescence spectrum was measured in the excitation intensity range of 0.1 to 4 $W.cm^{-2}$.

The luminescence was taken from the irradiated surface, analyzed by a SPEX 1704 grating monochrometer and detected by a cooled photomultiplier RCA 7102. The output of the photomultiplier was amplified by a lock-in amplifier PAR HR-8 and processed with a computer-controlled signal-

averaging system. The block diagram of the averaging system is presented in Fig. 3. The scanning wavelength interval and the scanning speed was controlled by a mini-computer MELCOM 70/20 through the computer drive units attached to the monochrometer. The commonly used scanning speed was 10 Å/sec and the signal sampling interval was 0.1 sec. In such conditions, the time necessary for one scanning was 20 sec. for the scanning wavelength interval of 200 Å commonly used for the measurement for a TO-phonon replica of exciton luminescence of silicon. The analog output of the lock-in amplifier was digitally converted and averaged for many times to improve the signal to noise ratio through the analog interface of mini-computer and memorized in the RAM, and finally data of the obtained spectrum with well improved signal to noise ratio were storaged in a floppy disk memory. The obtained luminescence spectrum memorized in the RAM was displayed on a CRT simultaneously in the photoluminescence measurement through a digital to analog converter attached to the micro-processer NEC TK-80. The final spectrum storaged in the floppy disk memory was recorded on a chart by using a X-Y plotter through the digital to analog converter.

II-4. impurity-concentration dependence

Figure 4 shows typical exciton-luminescence spectra of phosphorus, boron and lithium-doped silicon in the doping level of 10^{14} ~ 10^{15} cm^{-3}. The spectra reveal the FE luminescence lines (FE_{TA}, FE_{LO} and FE_{TO}) and BE luminescence lines (BE_{NP}, BE_{TA}, BE_{LO} and BE_{TO}) associated with these dopant impurities. The subscripts TA, LO and TO denote the corresponding momentum-conserving phonon involved in the transition and NP indicates

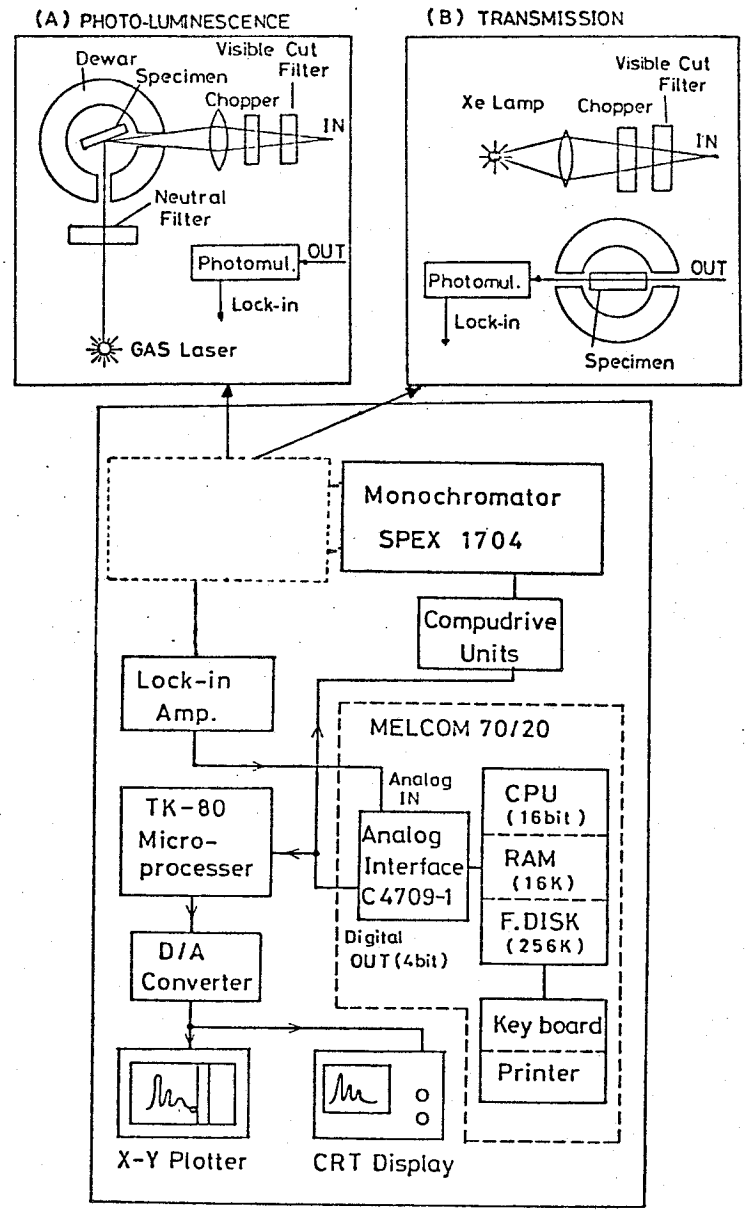

Fig. 3. Diagram of signal averaging system used in this work for high-resolution photoluminescence and transmission measurements.

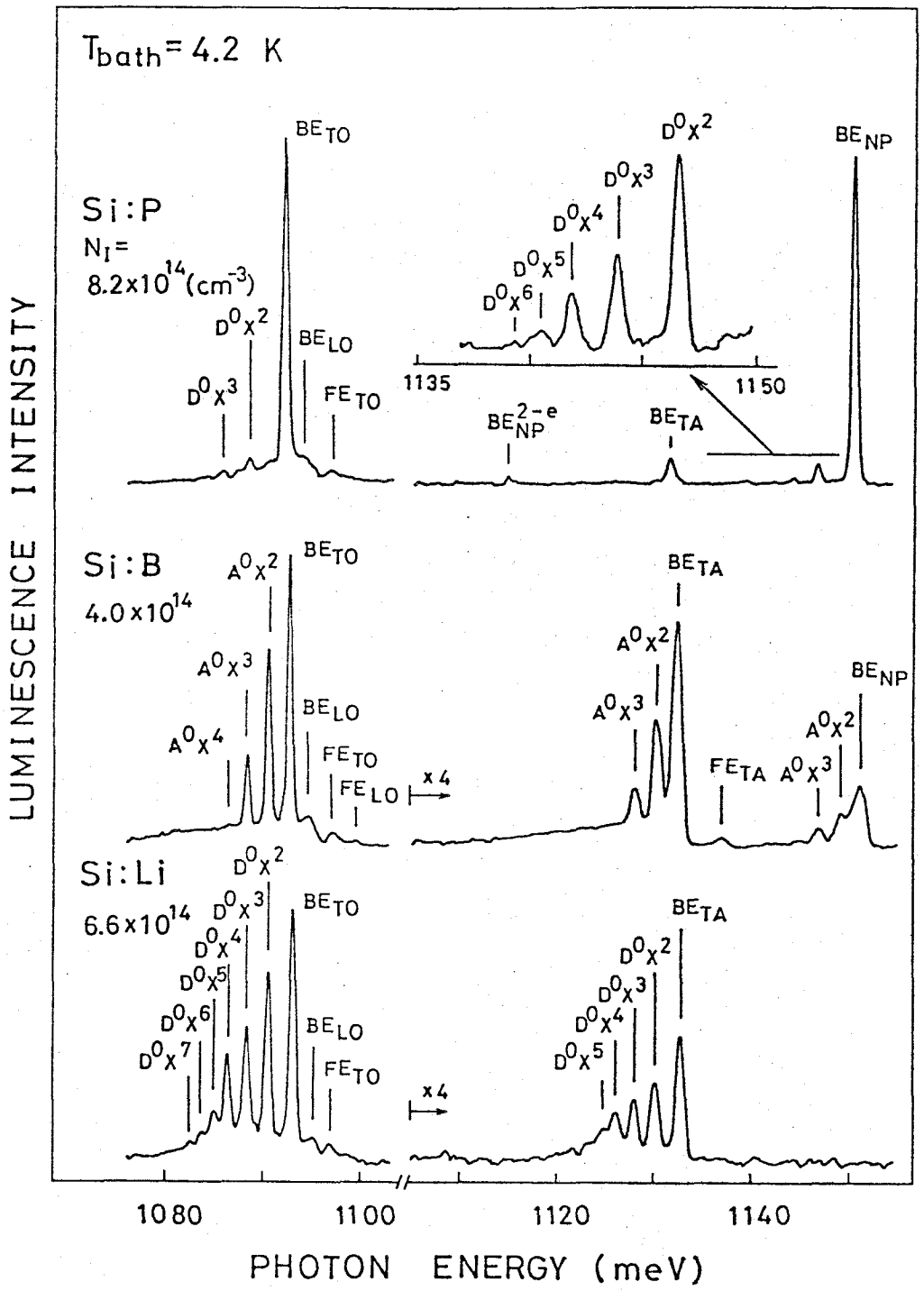

Fig. 4. Typical exciton-luminescence spectra of Si:P, Si:B and Si:Li. All the spectra were measured for the samples with the doping level around 5×10^{14} cm^{-3}.

no-phonon recombination lines. The two-electron satellite line (BE_{NP}^{2-e}) is also observed in the spectrum of Si:P. In addition to these FE and BE luminescence lines, a series of satellite luminescence lines labelled D^0X^m (m=2,3,...) for Si:P and Si:Li and A^0X^m (m=2,3,...) for Si:B appear in the low-energy side of the principal BE luminescence lines. These satellite lines are originated from BMEC related to phosphorus, boron and lithium impurities. As can be seen in the figure, many BMEC luminescence lines are strongly observed relative to the principal BE lines in Si:B and Si:Li, whereas the intensity of BMEC lines are rather weak compared with the BE lines in Si:P. We have measured systematically these exciton-luminescence spectra of impurity-doped silicon in the doping range of 10^{11} to 10^{18} cm^{-3}.

Figure 5 shows exciton-luminescence spectra in the TO-phonon region taken under the same excitation level for silicon containing boron with four different concentrations. In the lightly doped samples with the dopant content less than 10^{16} cm^{-3}, BE and BMEC luminescence lines are clearly observed although the intensity of BMEC lines becomes gradually weak compared with that of the principal BE luminescence line (BE_{TO}) as the impurity content increases. The intensity reduction of the BMEC luminescence lines in this doping region directly reflects the decrease of the steady-state density of FE, which can be seen also in the spectra, caused by the introduction of dopant impurity since BMEC contains several localized excitons and so the density of BMEC strongly depends on the FE density existing in the photoexcited crystal.

At high doping levels around 10^{16} cm^{-3}, the BMEC luminescence comes to be weaker, resulting in a low-energy tail of the principal BE line. At higher doping levels beyond 10^{17} cm^{-3}, the exciton-luminescence

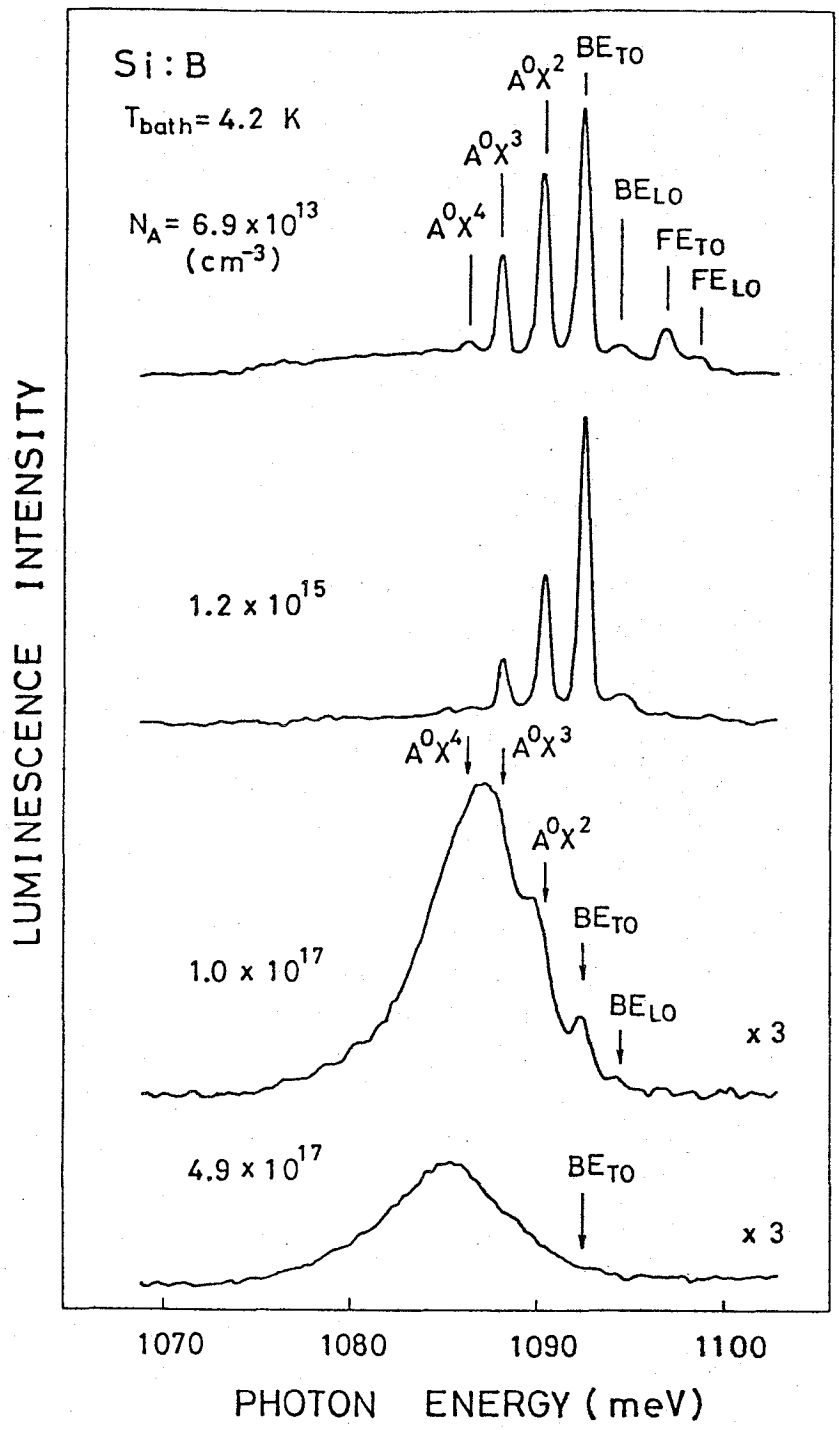

Fig. 5. Exciton-luminescence spectra from Si:B samples with four different boron contents in the TO-phonon region.

intensity greatly decreases and an anomalously broad luminescence band appears. In the sample with the boron content of 1.0×10^{17} cm^{-3}, the weak BE luminescence line still remains and a broad luminescence band is accompanied by several weak luminescence components near the peak-energy positions of BMEC lines denoted by arrows in the figure. For the sample of 4.9×10^{17} cm^{-3}, there appears only a single non-structural broad luminescence band, where the BE luminescence line completely disappears.

As can be seen in the figure, the peak-energy position of the broad luminescence band shifts to a low-energy side as the boron concentration increases[75,76]. We have observed such impurity-concentration behaviors of the broad luminescence band in exciton luminescence spectra of highly doped silicon with several species of donor (phosphorus, antimony, arsenic and lithium) and acceptor (boron and aluminum). It has been also found that the anomalously broad luminescence band shifts to a high-energy side and the principal BE luminescence line which is absent at liquid helium temperature comes to appear with increasing temperature[75]. This suggests the existence of another stable state of excitons different from the usual BE and BMEC as the origin of the broad luminescence band observed in high-doping range. Considering the above-mentioned impurity-concentration and temperature behaviors, we have reached a conclusion that the anomalously broad luminescence band is originated from radiative recombination of excitons localized at impurity complexes (pair and clusters) formed by the inclusion of a large amount of impurity around 10^{17}~$10^{18}$$cm^{-3}$. [75-79] The presence of such kinds of impurity complexes in this doping range below the so-called insulator-metal (Mott) transition of the impurity system has been

also verified in an infrared absorption study of impurity states in silicon[80].

The luminescence spectra of highly doped silicon with impurity contents around 3×10^{17} cm^{-3} for several species of donor and acceptor are shown in Fig. 6-(a) and (b). A broad luminescence band in the low-energy side of the principal BE line dominates over all the spectra. We have studied precisely the peak-energy shift of the broad luminescence band towards a low-energy side as a function of impurity concentration, the results showing that the peak-energy shift normalized by the exciton-binding energy of the principal BE of these impurity species strongly depends on the ionization energy of these impurities. It has been also found that the shift is larger for shallow impurity such as lithium compared with relatively deep impurity such as arsenic. This is another evidence for the role of inter-impurity interaction on the appearence of such an anomalously broad luminescence band and the characteristic peak-energy shift since overlapping of the impurity wave function is larger for shallow impurity like lithium.

II-5. excitation-level dependence

In the low-impurity concentration region below 10^{16} cm^{-3} where the inter-impurity interaction mentioned above can be neglected, exciton luminescence spectra of silicon are dominated by FE, BE and BMEC luminescence lines. In the photoexcited states of a ctystal, generated excitons recombine in some part and are captured by a neutral impurity and a formed BE, resulting in BE and BMEC, respectively. The formed BE and BMEC also decay in their given lifetimes. Thus the populations of

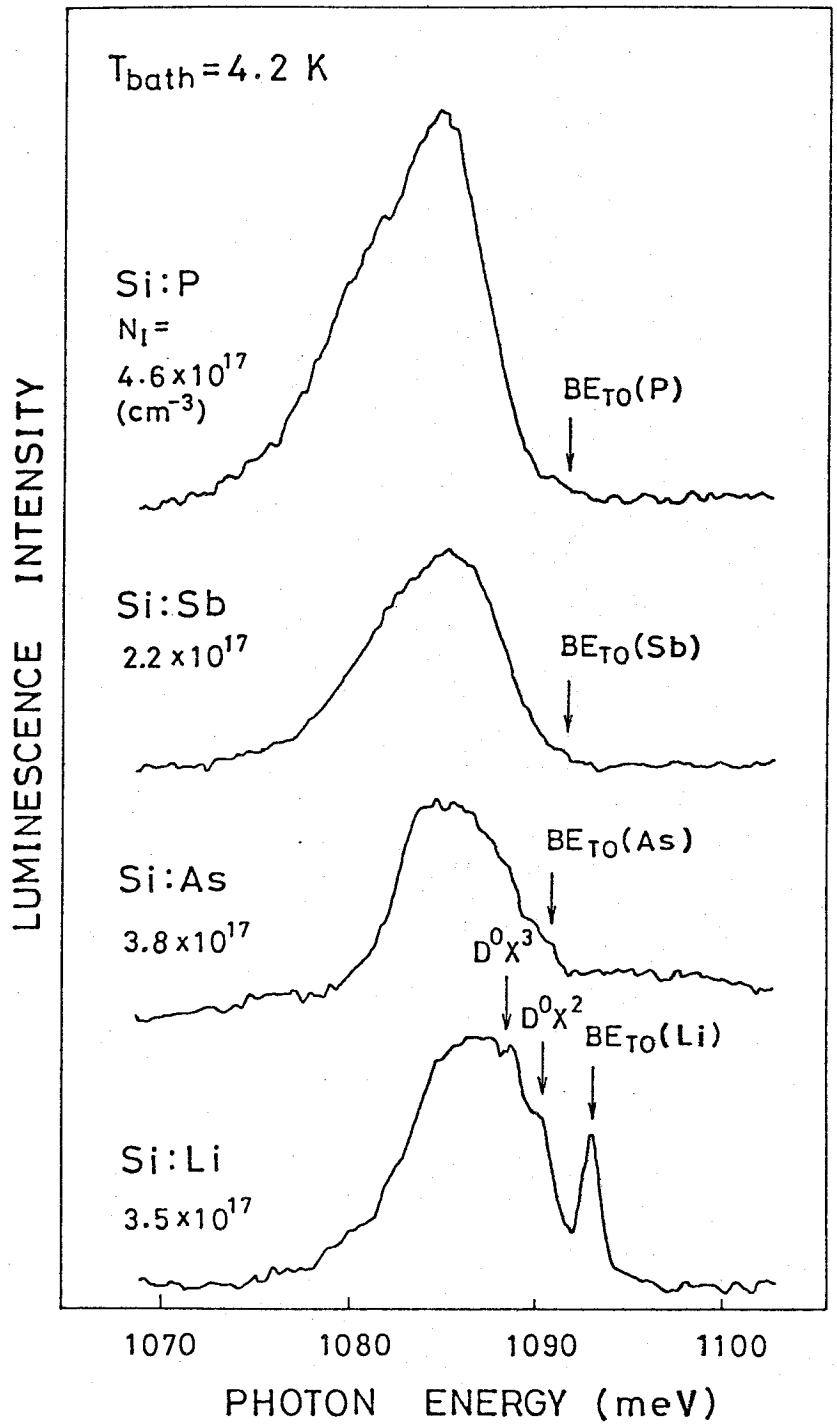

Fig. 6-(a) Broad luminescence bands in the TO-phonon region observed for highly doped silicon crystals with several species of donor.

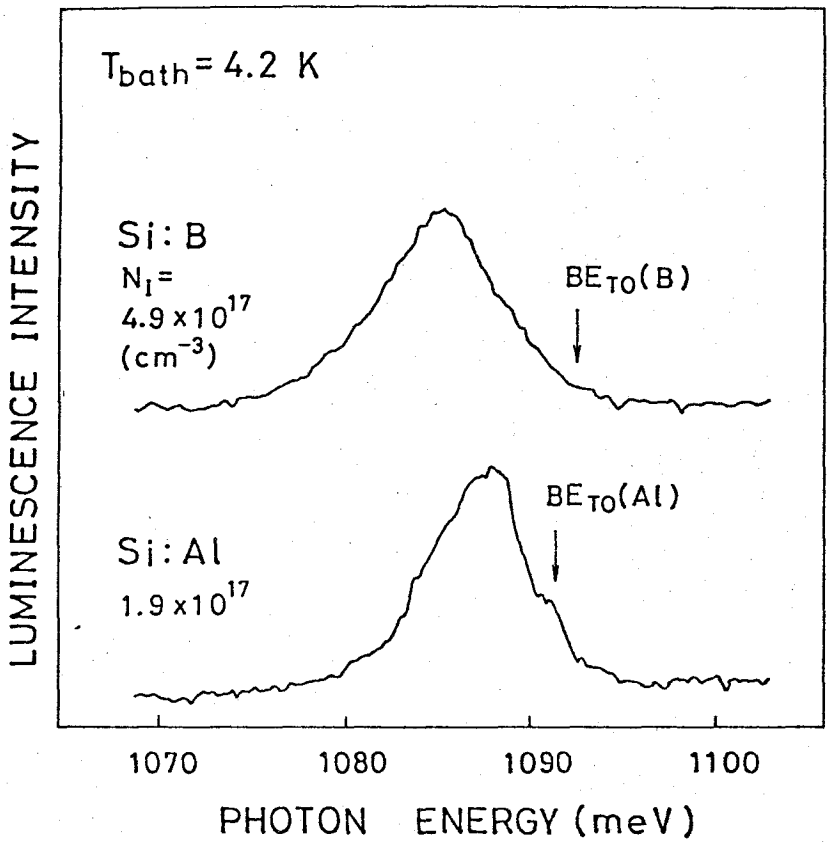

Fig. 6-(b). Broad luminescence bands observed for silicon crystals highly doped with acceptor species.

FE, BE and BMEC are in principle determined by the formation and decay kinetics of the system rather than by thermodynamics. In order to investigate the recombination kinetics of the FE, BE and BMEC system, we have measured precisely the excitation-level dependence of the luminescence intensities of FE, BE and BMEC in impurity-doped silicon with the content ranging from 10^{11} to 10^{15} cm^{-3}. These experimental data are analyzed on the basis of a model for the recombination kinetics of the system taking into account two physical processes determining the populations among FE, BE and BMEC, namely EC and AR processes.

Figure 7 shows the luminescence spectra of Si:B taken at several different excitation levels. The intensities of FE luminescence line (FE_{TO}) and BE line (BE_{TO}) increase approximately linearly with excitation level, while those of BMEC (A^0X^2 and A^0X^3) increase more rapidly with increasing excitation level than FE and BE. Figure 8 shows the plots of the luminescence intensities of FE, BE and BMEC as a function of excitation level for Si:B. At low-excitation levels, the slopes of the plots in Fig. 8 are approximately 1, 2 and 3, in the double-logarithmic scale, for BE, BMEC A^0X^2 and BMEC $^0X^3$, respectively. The slope is 1 for the FE luminescence intensity in this whole excitation range.

These excitation behaviors of the luminescence intensities of FE, BE and BMEC directly show the occurance of a successive reaction among the exciton system as follows.

$$A^0 + X \rightleftharpoons A^0X, \quad A^0 + 2X \rightleftharpoons A^0X^2, \quad A^0 + 3X \rightleftharpoons A^0X^3, \ldots \qquad (2.4)$$

This successive reaction causes a kind of mass-action law in the steady state given by

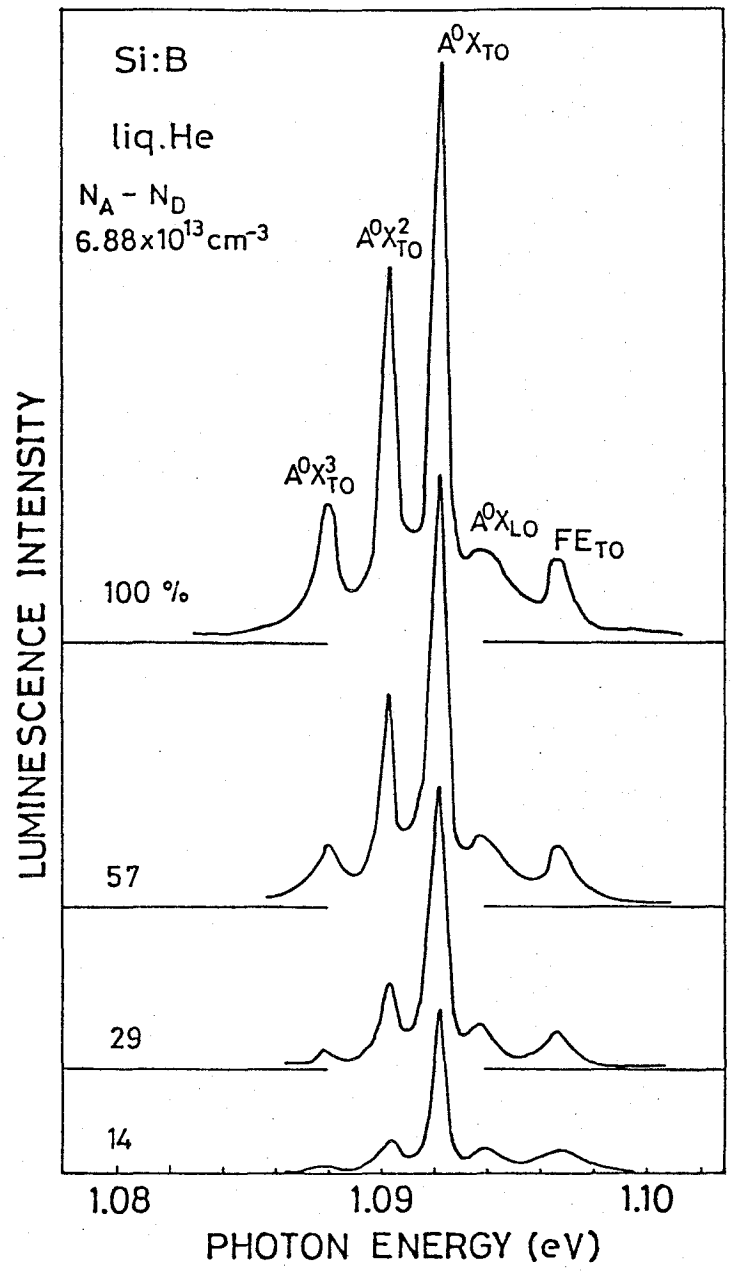

Fig. 7. Excitation-intensity dependence of exciton luminescence spectra of Si:B. 100 % excitation level corresponds to ∿ 1.5 $W.cm^{-2}$.

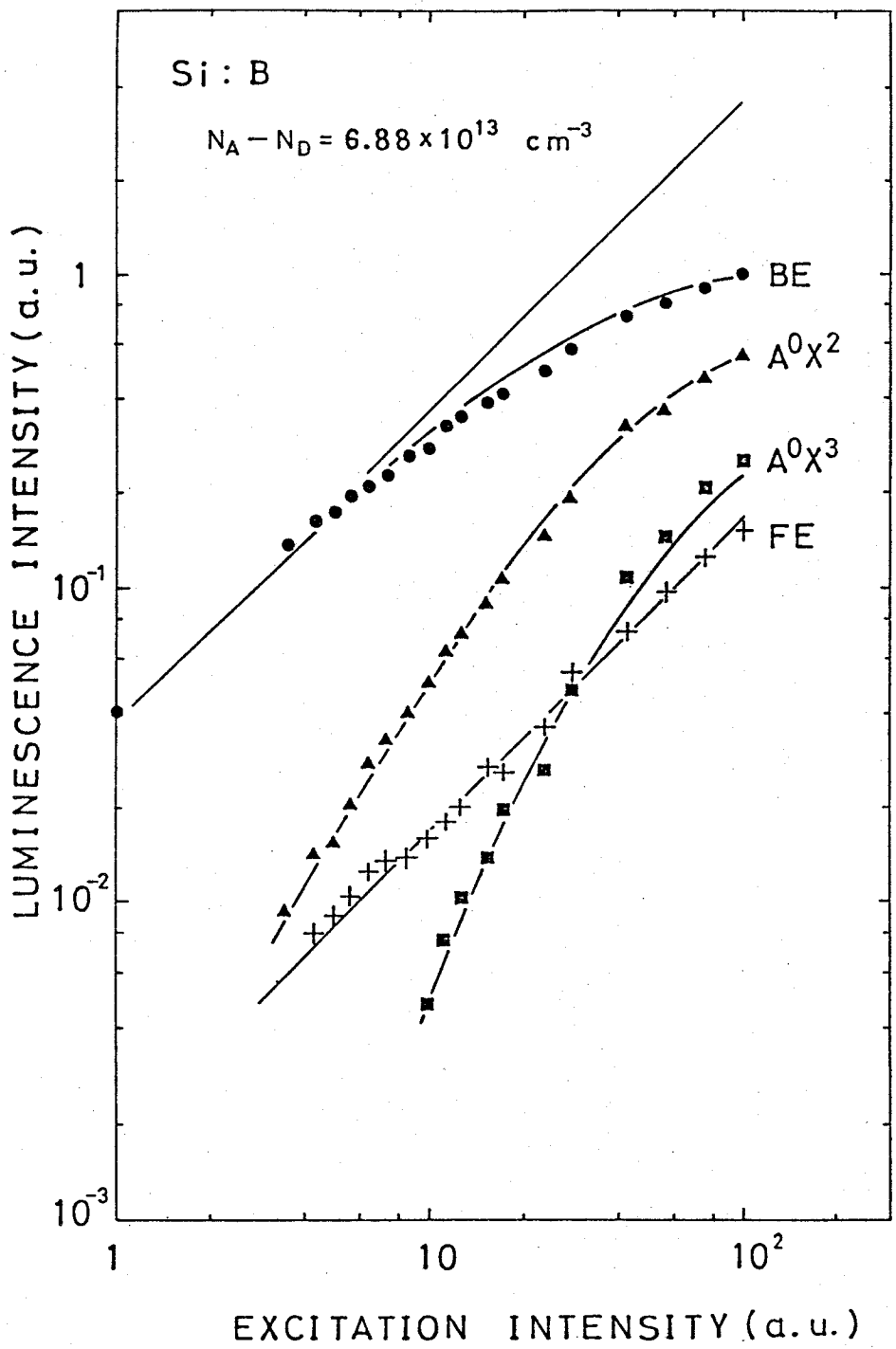

Fig. 8. Plots of the luminescence intensity due to free exciton, bound exciton and bound multiexciton complexes for Si:B as a function of excitation intensity.

$$[A^0X] = K_1[A^0][X],\ [A^0X^2] = K_2[A^0][X]^2,\ [A^0X^3] = K_3[A^0][X]^3,\ldots \tag{2.5}$$

where the brackets denote the density of the indicated center. The reaction constants appeared in Eq. (2.5) are in principle determined by dynamical parameters such as EC and AR rates, which will be discussed in detail in the following chapter. These excitation behaviors approximately described by Eq. (2.5) offer a direct evidence for the existence of BMEC containing several excitons localized at an impurity center as the origin of a series of satellite lines of principal BE luminescence line.

As can be seen in Fig. 8, the intensities of BE and BMEC gradually saturate at high excitation levels. This saturation behavior is considered as due to the fact that the concentration of impurity centers is finite and the densities of BE and BMEC localized at these impurity centers saturate at high excitation levels. Similar excitation behaviors are also observed for Si:P and Si:P, and the obtained results of Si:Li are presented in Figs. 9 and 10. In the spectrum of Si:Li, there appear many BMEC luminescence lines labelled D^0X, $D^0X^2,\ldots,D^0X^7$. Plotted in Fig. 10 are their luminescence intensities as a function of excitation intensity. Higher-order BMEC luminescence lines of Si:Li shows stronger dependence on excitation intensity, which is similar to the results of Si:B. We have systematically measured such excitation-intensity dependence for several Si:B, Si:P and Si:Li samples having the impurity content ranging from $10^{11} \sim 10^{15}$ cm^{-3}. These data will be analyzed in detail on the base of theoretical consideration on the formation and decay kinetics of FE, BE and BMEC system.

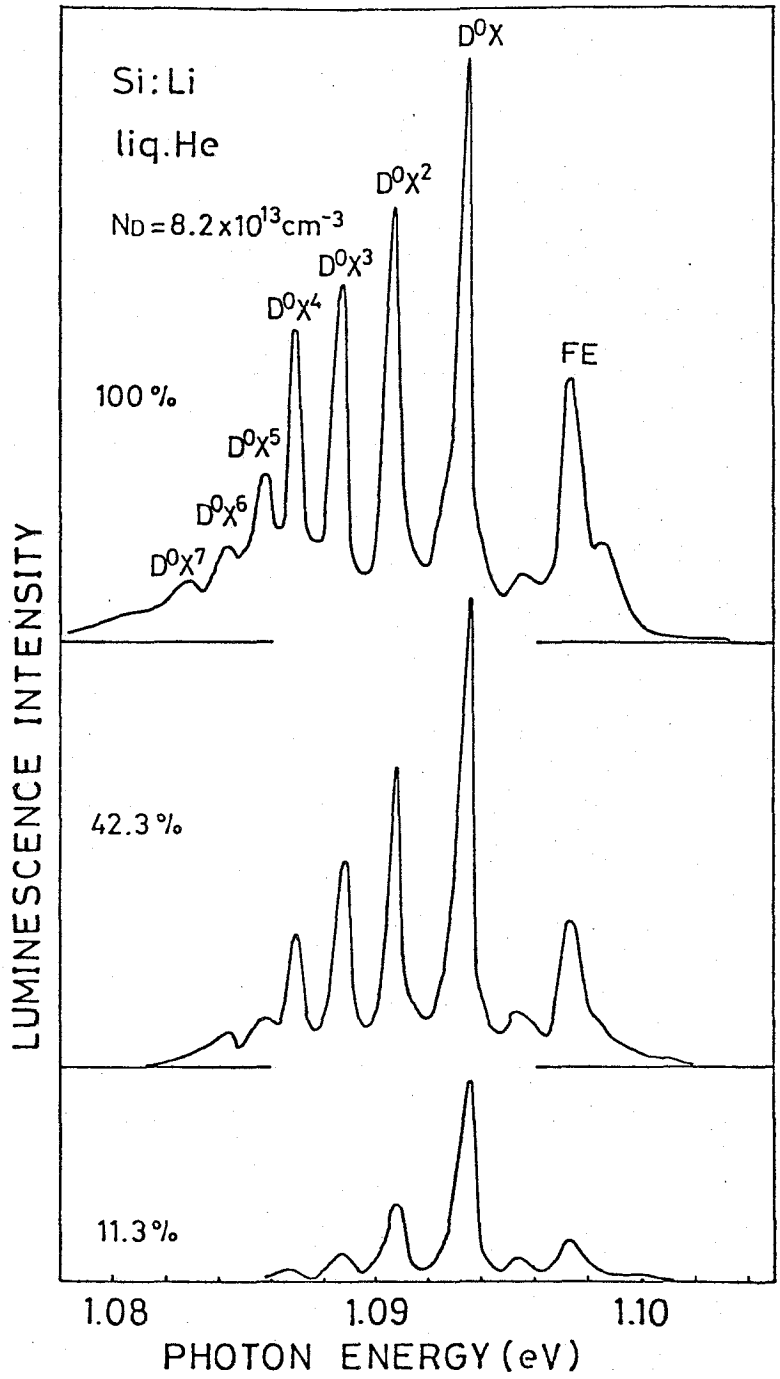

Fig. 9. Excitation-intensity dependence of exciton-luminescence spectra in the TO-phonon region of Si:Li.

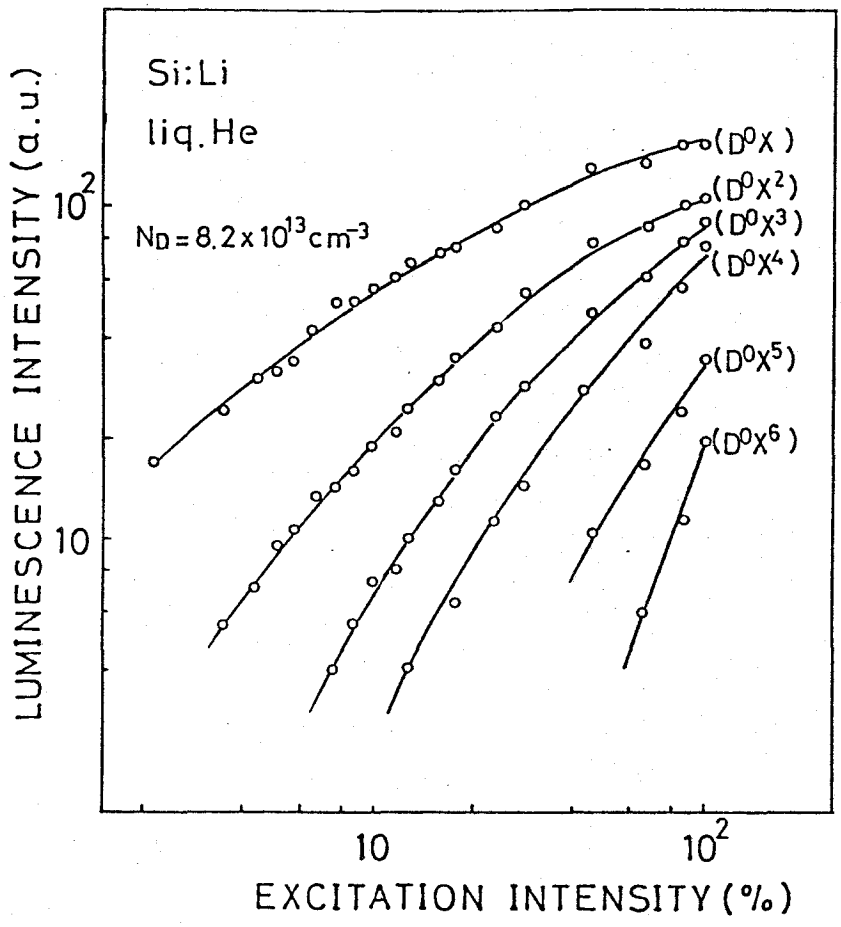

Fig. 10. Plots of the luminescence intensity of bound exciton (D^0X) and bound multiexciton complexes (D^0X^2-D^0X^6) as a function of excitation intensity for Si:Li.

CHAPTER III

ANALYSIS OF BOUND MULTIEXCITON LUMINESCENCE INTENSITY

In this chapter, we propose a model for the formation and decay kinetics of the FE, BE and BMEC system and analyze experimental data of the excitation-level dependence of the FE, BE and BMEC luminescence intensities by making use of coupled rate equations taking into account the EC and AR processes of BE and BMEC on the basis of the proposed model of kinetics. From a simple theoretical analysis of the experimental data, we can estimate recombination parameters such as EC and AR rates concerned with BMEC. The obtained values for Si:P, Si:B and Si:Li are discussed in terms of the shell structure model of BMEC for these impurity species. Finally, in the last of this chapter, theoretical considerations on the EC rate (cross section) at a neutral impurity center in silicon is presented in comparison with available experimental data.

III-1. a model for the formation and decay kinetics

In Fig. 11 we show the schematic diagram of the formation and decay processes of the FE, BE and BMEC system[20]. The notations used here are as follows: X and D^0X^m denote a FE and the m-th BMEC associated with donor, where we consider donor species here, however the essential points described is identical to the case of acceptor. g and W_f are the generation and recombination rate of FE, respectively. C_m is the EC rate of the m-th BMEC. W_m is the AR rate of the m-th BMEC. Here we assume that photoexcited electron-hole pairs become FE within

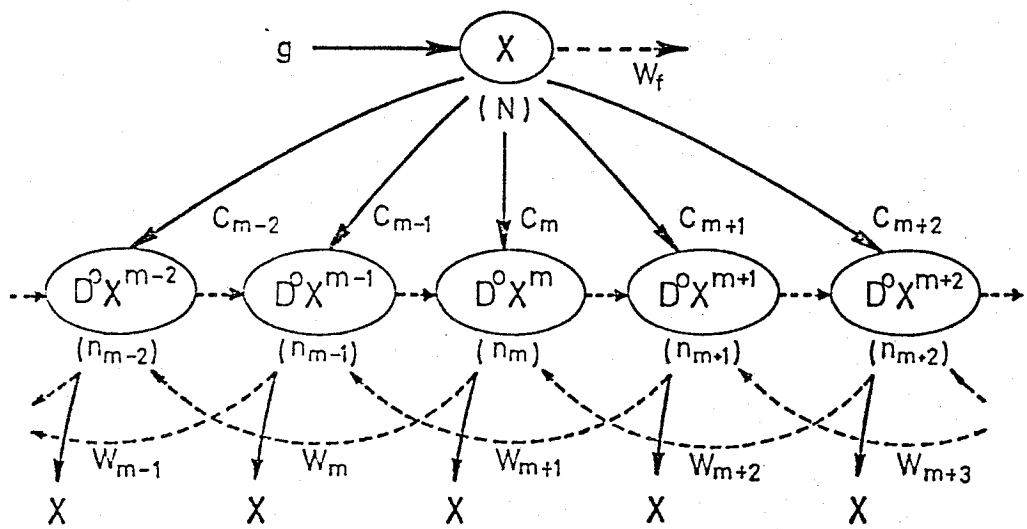

Fig. 11. Model of the formation and decay processes of the whole system consisting of free exciton, bound exciton and bound multiexciton complexes. In this model, exciton-capture and Auger-recombination processes are taken into consideration, where C_m and W_m denote the exciton-capture and the Auger-recombination rate concerned with the m-th bound multiexciton complex.

infinitesimal lifetime and therefore the density of free electron-hole pairs is negligible because all measurements have been performed at very low temperatures. As shown in Fig. 11, a part of generated FE recombines radiatively or nonradiatively. And the rest of the FE is captured by neutral donor centers (D^0) or BMEC centers with a help of phonon as in the case of the carrier capture process at an ionized impurity center. This process, EC process, is described as follows:

$$D^0X^m + X \longrightarrow D^0X^{m+1} + \text{phonon}. \qquad (3.1)$$

The D^0X^m center formed by the successive capture of FE decays in the finite lifetime through the following processes: (a) radiative recombination of an exciton within the D^0X^m complex. (b) nonradiative recombination of an exciton localized in the complex. (c) thermal dissociation of an exciton from the complex. Among these decay processes, the process (c) is considered to be negligible since the exciton-binding energy to the complex is a few meV and sufficiently larger than the thermal energy k_BT in the liquid helium temperature region where all measurements have been carried out in this work.

The nonradiative recombination process (b) is considered to be dominant among these processes by the fact that many electrons and holes are localized at high density around the impurity center in BMEC and this makes the AR process caused by electron-electron (hole-hole) Coulomb interaction quite probable. This type of AR process is called <u>localized Auger-recombination process</u>[81-83]. In this process, one bound electron recombines with a bound hole while exciting a second bound electron (hole) into the conduction (valence) band. In the case

of BMEC, the Auger process is considered as follows: An exciton (electron-hole pair) within BMEC D^0X^m recombines while exciting a second bound electron in the complex into the conduction band, leaving a "charged" complex described here as $D^0X^{m-2}h$, where h indecates a hole. This charged complex is unstable since the residual hole in the complex is subjected to repulsive potential from the positively charged impurity core screened by electron-hole pairs included in the complex. Therefore, this process is subsequently followed by the release of the residual hole from the charged complex, leaving the D^0X^{m-2} complex and a released free hole. Hence, this Auger process is described as

$$\begin{aligned} D^0X^m &\longrightarrow D^0X^{m-2} + e + h \\ &\longrightarrow D^0X^{m-2} + X \quad , \end{aligned} \tag{3.2}$$

where we consider that an exciton is reproduced immediately by the released electron and hole.

The kinetics of the BMEC system was briefly argued by Sauer [57] and Kosai and Gershenzon [58] in their original works on the verification of the BMEC model. Especially, Sauer formulated the simplified rate equations for BMEC[57]. However, the rate equations given by Sauer have been found to be inadequate in interpreting quantitatively the experimental results obtained in this work as was shown in our previous paper[20].

Here we consider the rate equations for BMEC, taking into account the EC and AR processes. At the steady-state condition the rate equations are described as follows:

$$0 = \frac{\partial n_m}{\partial t} = C_{m-1}Nn_{m-1} - C_m Nn_m + W_{m+2}n_{m+2} - W_m n_m \quad , \tag{3.3}$$

$$0 = \frac{\partial N}{\partial t} = g - W_f - \sum_{m=0}^{\infty} C_m Nn_m + \sum_{m=2}^{\infty} W_m n_m \quad , \tag{3.4}$$

where n_m is the density of D^0X^m complex (m=0 means the neutral impurity center) and N is the density of FE. In the right hand of Eq. (3.3), the first and second terms are due to the EC process, and the third and fourth are due to the AR process. The third term of Eq. (3.4) denotes the reduction of the FE density by EC process to a neutral impurity, BE and BMEC center. The fourth term of Eq. (3.4) indicates the FE density reproduced from the AR process of BMEC, where we consider in the case of the BE AR process that an excited carrier produced by AR is rapidly captured by an ionized impurity center simultaneously induced and therefore no FE is reproduced. In addition to Eqs. (3.3) and (3.4), n_m satisfies the following normalization equation given by

$$\sum_{m=0}^{\infty} n_m = N_I \quad , \tag{3.5}$$

where N_I denotes the concentration of dopant impurity concerned.
To solve these infinitely coupled rate equations, we make the assumption that under practical excitation levels as used in this experiments, the densities of sufficiently higher ordered complexes becomes negligibly small and therefore the infinitely coupled Eq. (3.3) can be cut off at a certain value of m, namely

$$C_m Nn_m = 0, \quad W_m n_m = 0 \quad \text{for} \quad m > k \quad , \tag{3.6}$$

where k is the critical value of m. Hence, the infinitely coupled Eqs. (3-3)-(3.5) reduces to a finite set of equations having k+2 unknown quantities (n_0, n_1,...., n_k and N). Using these coupled equations, we can numerically calculate the densities of a neutral impurity, FE, BE and BMEC as a function of FE generation rate g and impurity concentration N_I[27] if we can determine recombination parameters such as EC rate C_m and AR rate W_m involved in the kinetic equations.

As shown in Appendix, the solution of these equations is approximately given by the following form of the density ratio in BMEC,

$$\frac{n_m}{n_{m+1}} = \frac{W_{m+1}}{C_m}\frac{1}{N} + \frac{C_{m+1}}{C_m} \quad \text{for} \quad m=1,2,\ldots, k-1 \tag{3.7}$$

On the other hand, N is given from Eq. (3.4) by

$$N = \frac{g + \sum_{m=2}^{\infty} W_m n_m}{W_f + \sum_{m=0}^{\infty} C_m n_m} \simeq \frac{g}{W_f + \sum_{m=0}^{\infty} C_m n_m} , \tag{3.8}$$

where $\sum W_m n_m$ in Eq. (3.4) is neglected in relative to the FE generation rate g because it is the total density of FE reproduced from the AR process of BMEC complexes. Then, we define the effective lifetime τ_{eff} as $N=g\tau_{eff}$, resulting in the following expression from Eq. (3.8),

$$\tau_{eff} = 1 \,/\, [W_f + \sum_{m=0}^{\infty} C_m n_m] . \tag{3.9}$$

The effective lifetime of FE is determined by both the intrinsic recombination rate W_f and the total capture probability $\sum C_m n_m$. Strictly speaking, the latter term depends of the FE generation rate because the

density n_m is in principle determined by FE generation rate as well as dopant impurity content. However, it shoud be noted that the sum of the density n_m is fixed from the normalization Eq. (3.5), even if the FE generation rate highly increases. Hence it is roughly approximated as $\sum C_m n_m \simeq C_0 \sum n_m = C_0 N_I$.

Thus the total capture probability of a FE is considered to be hardly changed with the FE generation rate g, namely excitation intensity, which also means that the effective lifetime of FE is nearly independent of excitation intensity. Hence, the effective lifetime of FE is given by

$$\tau_{eff} \simeq 1 / [W_f + C_0 N_I] \quad . \tag{3.10}$$

For comparison with experimental results, we consider the lumimescence intensity ratio defined as $R_m = I(D^0X^m) / I(D^0X^{m+1})$. From Eq. (3.7), R_m is written by

$$R_m = \frac{I(D^0X^m)}{I(D^0X^{m+1})} = \frac{W_{r,m}}{W_{r,m+1}} \left\{ \frac{W_{m+1}}{C_m} \frac{1}{N} + \frac{C_{m+1}}{C_m} \right\} \quad . \tag{3.11}$$

Here $I(D^0X^m)$ is the luminescence intensity of the m-th BMEC given by $I(D^0X^m) = W_{r,m}\, n_m$ by using the radiative recombination rate $W_{r,m}$. Eq. (3.11) is rewritten as a function of excitation intensity I_e as follows,

$$R_m = \frac{W_{r,m}}{W_{r,m+1}} \left\{ \frac{W_{m+1}}{C_m} \frac{1}{\tau_{eff} K} \frac{1}{I_e} + \frac{C_{m+1}}{C_m} \right\} \quad , \tag{3.12}$$

where K is a proportional constant in the form of $g=KI_e$. Thus, the theoretical formura of the luminescence intensity of BMEC, in the form of the ratio, as a function of impurity concentration and excitation

intensity is established here.

III-2. a method of determining exciton-capture and Auger-recombination rates

In this section we obtain recombination parameters involved in the FE, BE and BMEC recombination processes on the basis of the theoretical formulas obtained here. The experimental results of the luminescence-intensity ratio R_m (m=1 and 2) of the m-th BMEC to the (m+1)-th BMEC as a function of inverse excitation intensity $1/I_e$ for Si:B are presented in Fig. 12. Essential features observed for these plots are as follows: (a) Data points of R_m (m=1,2) are well on straight lines for all the samples. (b) The slope of the straight line becomes larger with increasing impurity concentration. (c) All the straight lines have the same intersection at $1/I_e=0$. These features are well consistent with theoretical predictions from the formula of R_m, Eq. (3.12), introduced in the previous section.

From Eq. (3.12), it is found that the luminescence intensity ratio R_m is a linear function of inverse excitation intensity $1/I_e$, for τ_{eff} is nearly independent of I_e as mentioned above; see Eq. (3.10). The slope of the linear function $R_m(1/I_e)$ is written by substituting Eq. (3.10) into Eq. (3.12) as a function of impurity concentration N_I as

$$a_m(N_I) = \frac{W_{r,m}}{W_{r,m+1}} \frac{W_{m+1}}{C_m} \frac{W_f + C_0 N_I}{K} , \qquad (3.13)$$

where we define the slope in $R_m(1/I_e)$ as $a_m(N_I)$. Eq. (3.13) shows that the slope in R_m-$1/I_e$ plots increases with increasing impurity content N_I[20]. Another theoretical prediction from Eq. (3.12) is that the

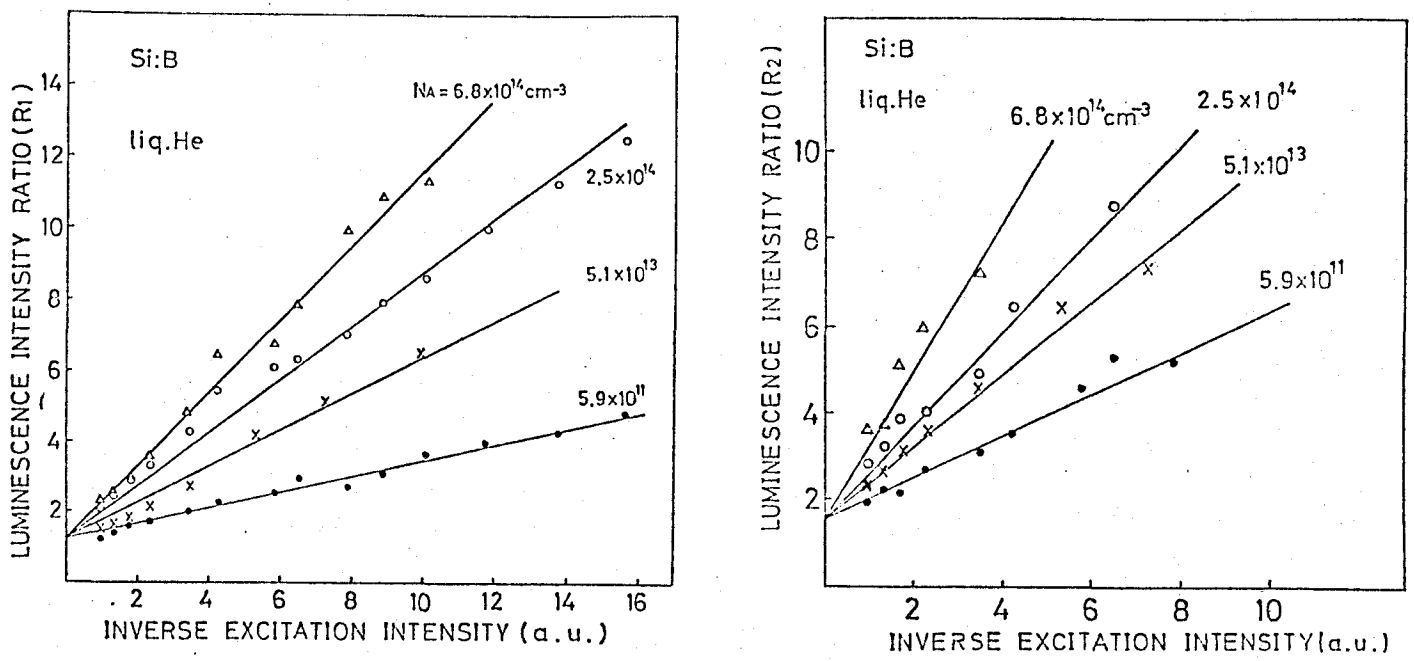

Fig. 12. Plots of the luminescence-intensity ratio $R_m = I(A^0X^m)/I(A^0X^{m+1})$ (m=1,2) of Si:B as a function of inverse excitation intensity.

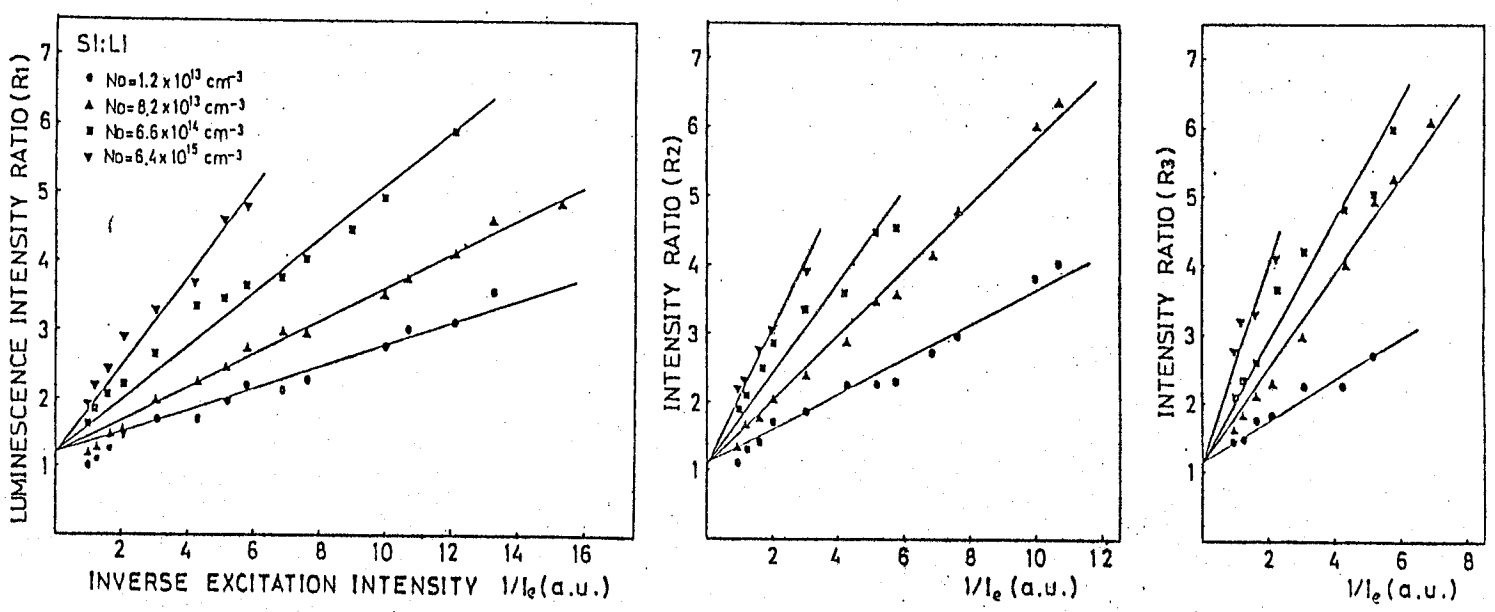

Fig. 13. Plots of the luminescence-intensity ratio $R_m = I(A^0X^m)/I(A^0X^{m+1})$ (m=1,2 and 3) of Si:Li as a function of inverse excitation intensity.

value of R_m at $1/I_e=0$ is given by $(W_{r,m}/W_{r,m+1})/(C_{m+1}/C_m)$ and therefore independent of impurity content. And hence, these features observed in the experimental data of R_m-$1/I_e$ plots are completely explained by the theoretical formula of Eq. (3.12). Similar results have been also observed for Si:P and Si:Li[21]. The typical results for Si:Li are shown in Fig. 13.

Thus, we can estimate EC and AR rates, in the form of their ratio, directly from R_m-$1/I_e$ plots on the basis of Eq. (3.12) by using the following relations[23].

$$\frac{C_{m+1}}{C_m} = \frac{W_{r,m+1}}{W_{r,m}} R_m(1/I_e \to 0) \quad \text{for} \quad m=1,2,\ldots \tag{3.14}$$

$$\frac{W_{m+1}}{W_m} = \frac{W_{r,m-1}W_{r,m+1}}{(W_{r,m})^2} \frac{C_m}{C_{m-1}} \frac{a_m(N_I)}{a_{m-1}(N_I)} \quad \text{for} \quad m=2,3,\ldots \tag{3.15}$$

Furthermore, the value of C_0, the EC rate at a neutral impurity center, can be also determined from an analysis of excitation-intensity dependence data of the luminescence-intensity ratio of BE to FE[27], which is presented in chapter IV.

III-3. exciton-capture and Auger-recombination rates of phosphorus, boron and lithium BMEC

Using Eqs. (3.14) and (3.15), we have obtained EC and AR rates of BMEC for Si:P, Si:B and Si:Li from the analysis of the systematic experimental data of excitation-level dependence of the luminescence-intensity ratio R_m for these impurity species. In the analysis of the BMEC luminescence intensity, so-called α-line series[15] in the no-phonon spectral region are taken into account for phosphorus. Principal BMEC

lines in the TO-phonon region, see Fig. 4, are used for boron and lithium. Here, the radiative recombination rate $W_{r,m}$ for the m-th BMEC is assumed to be proportional to the product of the numbers of electron and hole in the impurity-specific shell concerned with transitions of these BMEC-luminescence lines. The values of radiative recombination rate are presented in Table I. Making use of the value of $W_{r,m}$, we have obtained EC and AR rates from the R_m-$1/I_e$ plots as shown in Figs. 12 and 13.

Figure 14 shows plots of the AR rates of BMEC normalized by that of BE. As well known, the AR process which involves three particles, namely two electrons and one hole for the eeh-process or one electron and two holes for the ehh-process, is characterized by its carrier dependence of the recombination rate[82]. The eeh-process shows n^2p dependence and the ehh-process shows np^2 dependence, where n and p are the electron and hole density, respectively. We have calculated simply the AR rate of donor BMEC using the following formula[22].

$$W_m = A(n_{1,m})^2 p_{1,m} \quad , \tag{3.16}$$

where A is a proportional constant, and $n_{1,m}$ and $p_{1,m}$ are the local density of electron and hole localized in the m-th BMEC, respectively. These densities are defined here as

$$n_{1,m} = (m+1)[(4\pi/3)(a_{1,m})^3]^{-1}, \quad p_{1,m} = m[(4\pi/3)(b_{1,m})^3]^{-1}. \tag{3.17}$$

$a_{1,m}$ and $b_{1,m}$ is Bohr radius of electron and hole in the m-th BMEC, respectively. The value $a_{1,m}$ and $b_{1,m}$ have been recently estimated by Wünsche et al[16]. The calculated values of W_m by using Eq. (3.16) are

Table. I The value of radiative transition rate given by $W_{r,m} \sim n_e(\Gamma_\mu) \cdot n_h(\Gamma_\nu)$, where n_e and n_h are electron and hole number involved in the transition.

	Shell Structure	Transition	$W_{r,m} \sim n_e(\Gamma_\mu) \cdot n_h(\Gamma_\nu)$
Phosphorus	$\{2\Gamma_1, (m-1)\Gamma_{3,5}; m\Gamma_8\}$	$e(\Gamma_1) - h(\Gamma_8)$	$2 \times m$ $(m=1,2,3,4)$ 2×4 $(m=5,6,\ldots)$
Boron	$\{m\Gamma_e; (m+1)\Gamma_8\}$	$e(\Gamma_e) - h(\Gamma_8)$	$m \times (m+1)$ $(m=1,2,3)$ $m \times 4$ $(m=4,5,\ldots)$
Lithium	$\{(m+1)\Gamma_{3,5}; m\Gamma_8\}$	$e(\Gamma_{3,5}) - h(\Gamma_8)$	$(m+1) \times m$ $(m=1,2,3,4)$ $(m+1) \times 4$ $(m=5,6,\ldots)$

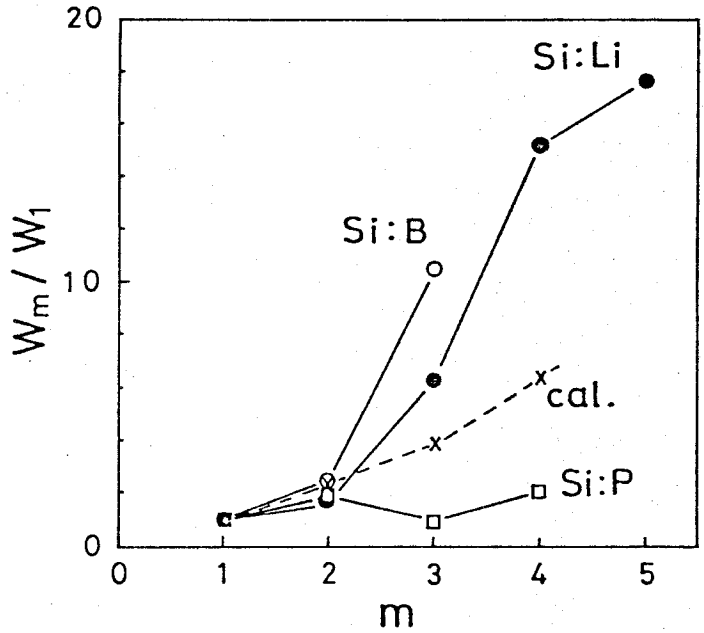

Fig. 14. Plots of Auger-recombination rates as a function of the order m of bound multiexciton complex, where m=1 means bound exciton. Dashed line shows the calculated values using the formula; $W_m = A(n_{1,m})^2 p_{1,m}$, where $p_{1,m}$ and $n_{1,m}$ are the "local density" of an electron and a hole localized in m-th bound multiexciton complex.

plotted in Fig. 14. As is shown in this figure, the variation of AR rates of phosphorus BMEC with the order m of BMEC is small as compared with those of lithium and boron and also calculated values. For phosphorus BMEC, as is expected by the shell model[15], two electrons in the first Γ_1 are highly localized in the central-cell region of an impurity center compared with remaining electrons in the next $\Gamma_{3,5}$ shell, and hence two electrons in the Γ_1 shell effectively contribute to the AR process of phosphorus BMEC. This makes the variation of the AR rate with the order m small, which is consistent with experimental observations. On the other hand, in the case of lithium all the electrons in the ten-fold degenerate $\Gamma_{3,5}$ inner shell contribute equally to the AR process and therefore the rate depend on the total numbers of electron and hole. This makes the change of AR rate with the order m of BMEC large. The difference between the experimental values of W_m and calculated values is considered to be as due to the fact that the shell structure of BMEC has not been taken into account in the calculation of $a_{1,m}$ and $b_{1,m}$ by Wünsche et al[16]. As can be seen in Fig. 14, the behavior of AR rate of boron BMEC having the highly degenerate inner shell like lithium is similar to that of lithium BMEC.

EC rates of phosphorus, lithium and boron BMEC obtained by the method described above are plotted in Fig. 15. The clear difference in the dependence of EC rate on the order m among these impurity species is also observed. Contrary to behaviors of AR rates, the EC rate of phosphorus BMEC shows strong dependence on m compared with lithium and boron. In the EC process of BMEC, it is considered that excited shells of BMEC play an important role for EC process in contrast to AR process. At least two types of EC process are considered and the details are

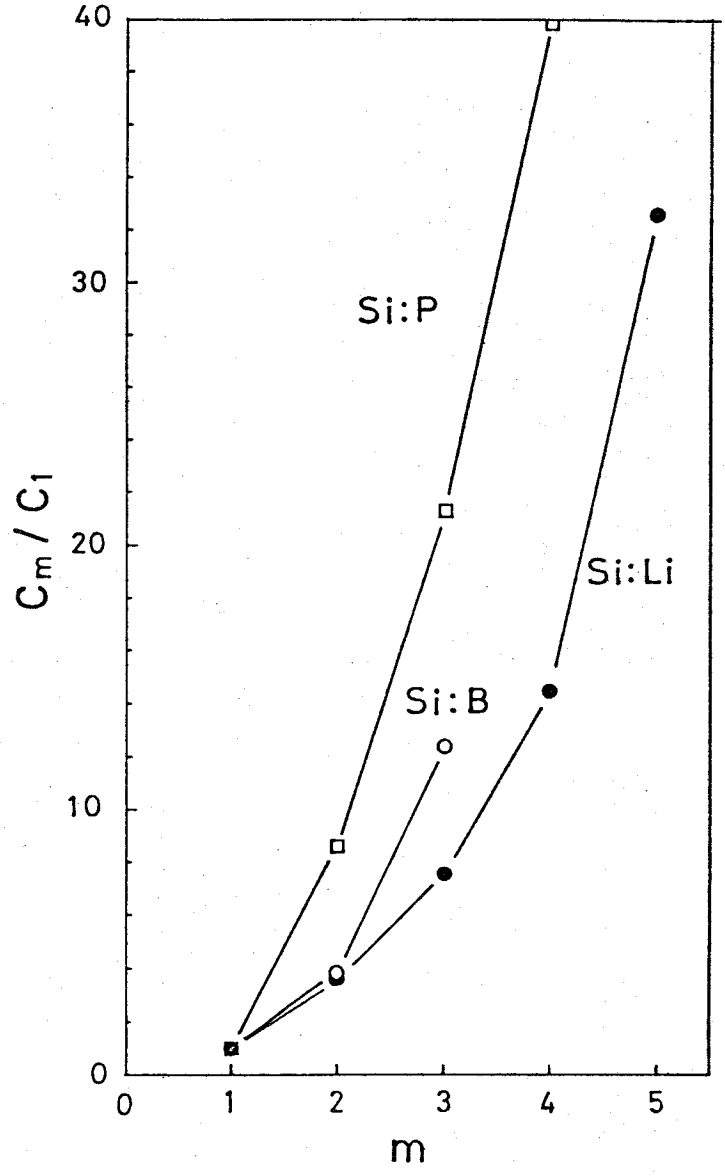

Fig. 15. Plots of exciton-capture rates as a function of the order m of bound multiexciton complex.

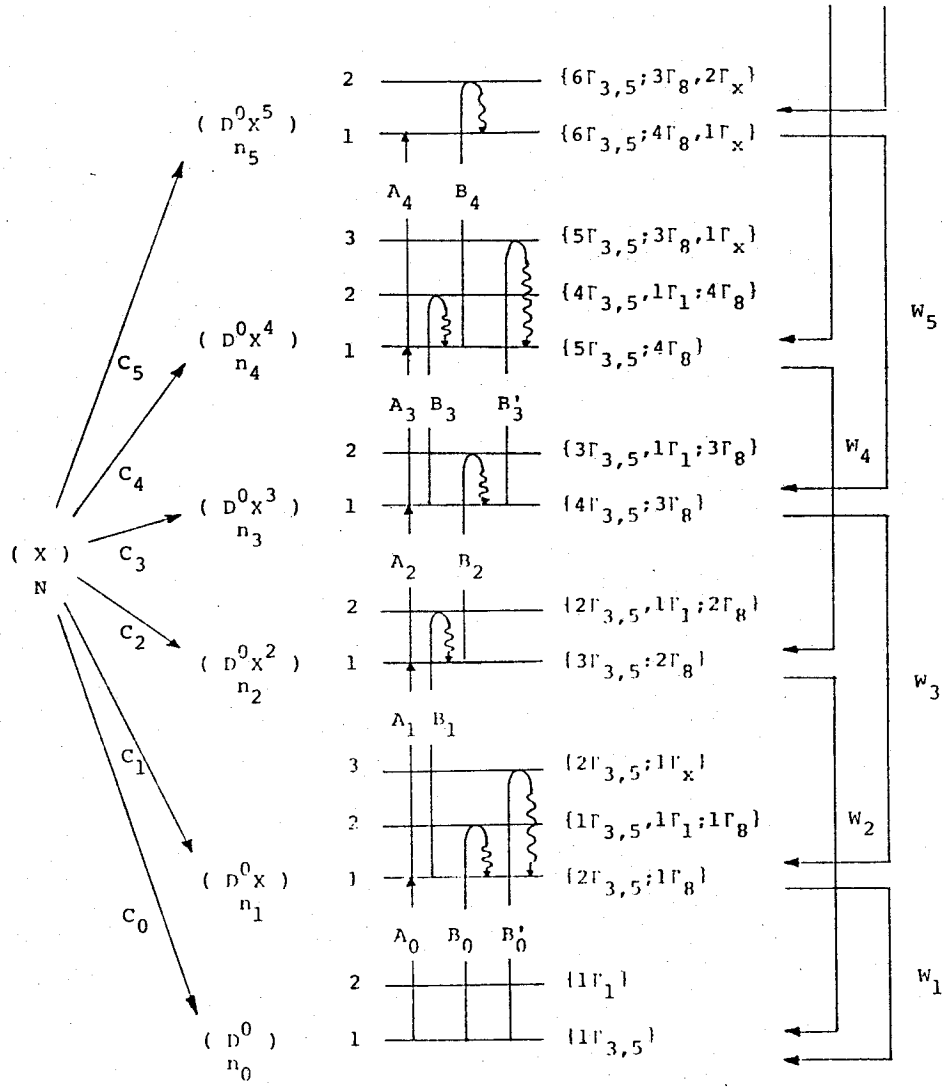

Fig. 16. Schematic representation of exciton-capture and Auger-recombination processes of lithium bound multiexciton complexes. Two types of exciton-capture processes, labelled A_m and B_m, are classified. In the A_m process, an exciton is captured directly into ground state of bound multiexciton complex, and in the B_m process an exciton is initially captured at excited states and relaxes to the ground state.

Table. II Auger-recombination rates obtained from rate-equation analyses for the excitation level dependence of BMEC luminescence intensity.

	Phosphorus	Boron	Lithium	calculation **
W_1 (s^{-1})	3.68×10^6 *	9.48×10^5 *	8.70×10^5 *	
W_2/W_1	1.89 *	2.46 *	1.61	2.36
W_3/W_2	0.52	4.28	3.94	1.66
W_4/W_3	2.14		2.40	1.63
W_5/W_4	∿ 5.61		1.16	

* Value obtained by Schmid, Ph. D Thesis, Stuttgart University, 1977 (ref. 84)

** These values are obtained by using the relation; $W_m = A(n_{l,m})^2 p_{l,m}$, where $n_{l,m}$ and $p_{l,m}$ are "local density" of electron and hole in the m-th BMEC.

Table. III Exciton-capture rate obtained from rate-equation analysis.

	Phosphorus	Boron	Lithium
C_0 (cm^3s^{-1})	2.54×10^{-7}	2.02×10^{-8}	5.0×10^{-10}
C_1/C_0		~ 3.50	
C_2/C_1	8.60	3.84	3.57
C_3/C_2	2.48	3.23	2.12
C_4/C_3	1.87		1.92
C_5/C_4	~ 0.78		2.24

schematically shown in Fig. 16 in the case of lithium BMEC.

In the EC process labelled A_m(m=0,1,2,..) in this figure, both of electron and hole go into their ground shell $\Gamma_{3,5}$ and Γ_8, respectively. In the case of BMEC D^0X^5, a hole is captured into the lowest excited shell labelled Γ_x. On the other hand, in the B_m(m=0,1,2,...) type process, either of electron or hole or both is initially captured into the outer excited shell, the Γ_1 shell for electron and the Γ_x shell for hole, and subsequently relaxes to the ground shell with emission of phonon. The B_m process is considered to be more effective than the A_m type process since in the B_m process momentum transferred from FE to phonon is smaller than A_m process. This is consistent with the so-called cascade-capture process of a carrier at an ionized impurity center[85]. Therefore, the energy level spacing and the degeneracy of the excited shell of BMEC in the excited state determine the value of EC rates. It should be noted that phosphorus BMEC has the highly degenerate excited electron shell $\Gamma_{3,5}$ with ten-fold degeneracy, whereas lithium BMEC has two-fold degenerate outer Γ_1 shell[15]. Hence, the difference in the degeneracy of excited shell between phosphorus and lithium is closely related to the difference in the behavior of EC rate observed in Fig. 15. The obtained values of EC and AR rates are summarized in Tables II and III.

III-4. transient decay behaviors

Transient decay measurements on BMEC luminescence lines of silicon have been made to examine the origin of BMEC lines[63,68,84,86], the results leading to the identification of the shell structure of BMEC. We have tried to generalize theoretical considerations on the kinetics

of BMEC from the steady-state to transient decay behaviors on the basis of the rate equations of Eq. (3.3) and (3.4). There are two available experimental data for the time transient measurement of BMEC lines in Si:Li[58,84]. For comparison with these data, we have calculated transient decay behaviors of BMEC, especially lithium BMEC, by solving numerically Eqs. (3.3) and (3.4) using the experimentally obtained values of EC and AR rates[21]. The theoretically calculated decay curves of BMEC (D^0X^m, m=1,2,..5) in Si:Li for two Li concentrations are presented in Fig. 17. In the calculation, we assumed that the exciton generation rate g is 10^{21} $cm^{-3}sec^{-1}$ in the initial condition. The essential feature in the decay curves does not change drastically with the value of g, but rather strongly depends on the impurity concentration[21].

Although a detailed fitting of the calculated decay curves to the previously reported data cannot be done here because of having no knowledge to their detailed experimental conditions, it has been found that the calculated decay curves of BMEC lines in Si:Li reveal some characteristic features observed in the previously reported decay curves[58,84]. As can be seen in the decay curves for the lithium concentration of 10^{15} cm^{-3}, the rounding is seen in all the BMEC lines at early times and their decay curves becom exponential for longer time[86]. At higher doping levels, the transient decay of BMEC lines becomes more rapid and shows two decay times for higher order BMEC lines, as shown in Fig. 17-(b). This behavior in the decay of BMEC luminescence lines is well consistent with data reported by Kosai and Gershenzon[58] for Si:Li with lithium concentration of 3×10^{16} cm^{-3}. The appearance of the first and second decay time presented in Fig. 17-(b) is considered to be as due to the existence of <u>reproduction</u> phenomenon of FE induced by the AR process of

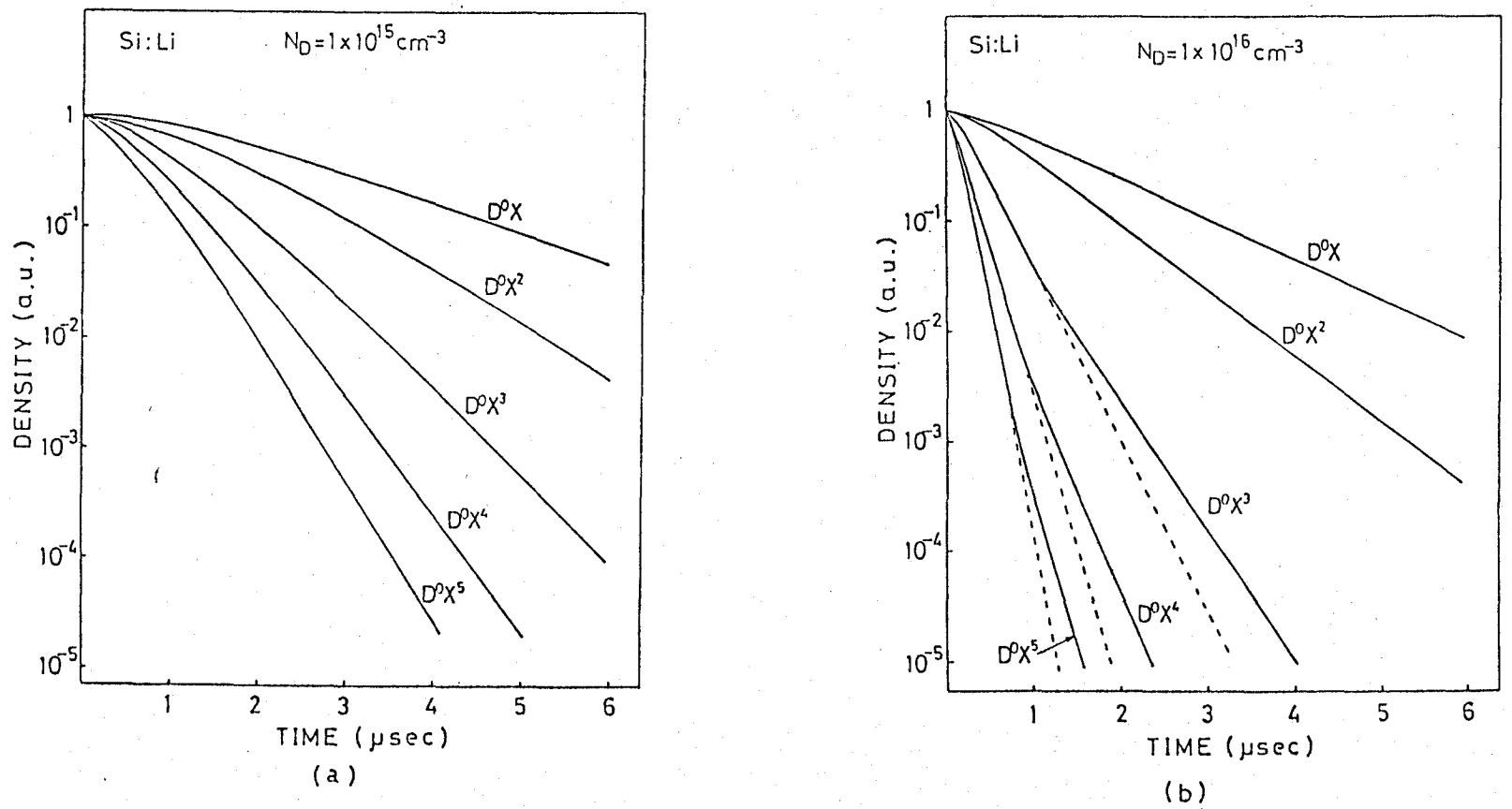

Fig. 17. Calculated transient-decay curves, based on the rate equations (3.3)-(3.5), of the bound exciton and bound multiexciton density of Si:Li for Li concentration of 10^{15} cm^{-3} (a), and 10^{16} cm^{-3} (b).

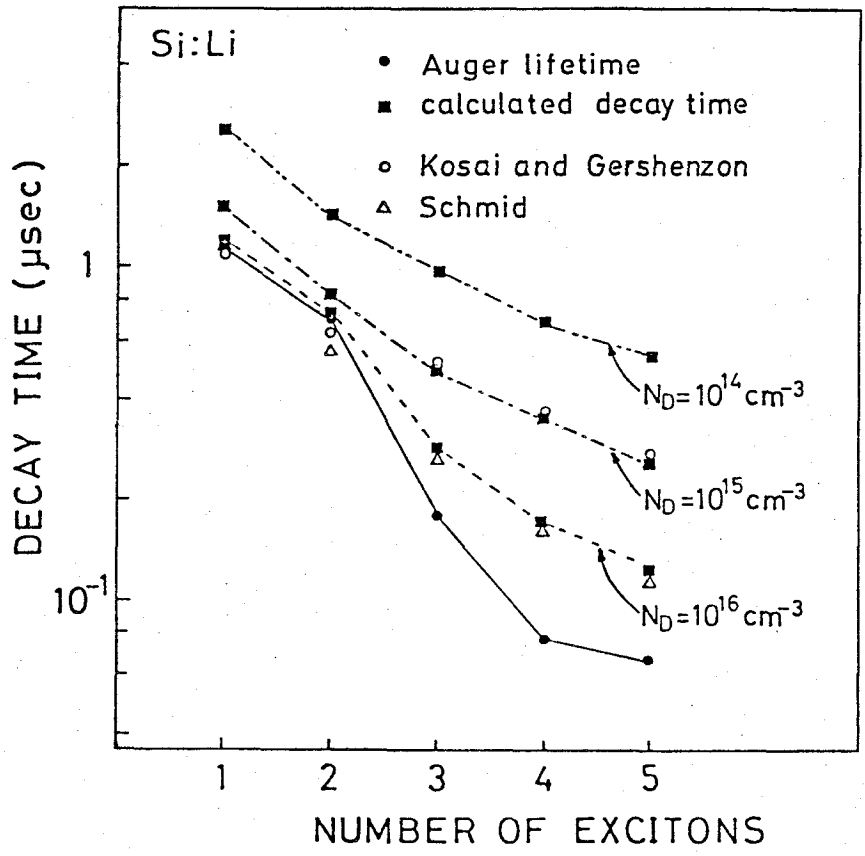

Fig. 18. Plots of the calculated decay times and Auger lifetime ($1/W_m$) experimentally obtained in this work. Decay times obtained by photoluminescence decay measurements by Schmid (ref. 84) and Kosai and Gershenzon (ref. 58) are also plotted.

BMEC as shown by Eq. (3.2). Actually, we have calculated the transient density of FE, denoted by N in Eq. (3.4), and found that the fourth term of Eq. (3.4) determines the decay characteristics of FE. Namely, a large amount of FE is reproduced from BMEC already formed in the initial (t=0) state and makes the decay constant observed in the usual transient measurement of FE large. This also causes the first (small decay constant) and second (long decay constant) decay times of BMEC luminescence lines as can be seen in Fig. 17-(b) and the experimental data of Kosai and Gershenzon[58].

The calculated decay times, estimated from plots as presented in Fig. 17, as a function of the order (number of localized excitons) m of BMEC are shown in Fig. 18. It should be noted that the decay times depend strongly on the impurity concentrations as mentioned above. The decay times vary gradually with impurity concentration and tend toward those of the AR lifetime, $1/W_m$, at higher impurity concentration. It shoud be also noted here that the decrease in decay time with the order m of BMEC agrees well with experimental data which are plotted in the figure.

Thus, it has been found that the kinetic Eqs. (3.3)-(3.5) of the FE, BE and BMEC system proposed in this work well explain both the steady-state photoexcitation behaviors, such as excitation-level and impurity-concentration dependence, and the transient decay behaviors.

III-5. exciton-capture cross section at a neutral impurity

As was shown in the previous sections, the EC process is the dominant

formation process of BE and BMEC. However, little is known about the EC process in both theoretical and experimental aspects. In the present work, we have obtained for the first time the EC rates of BE and BMEC as well as those of a neutral impurity center. There exist a few experimental data available in the case of the EC cross section on a neutral phosphorus, boron and indium impurities, which were obtained from luminescence decay measurements[87,88]. Recently, Elliot et al. have obtained the temperature dependence of the EC cross section on a neutral indium impurity from a study of photoluminescence decay of the indium BE, showing that the EC cross section decreases with increasing temperature. The temperature dependence is similar to that of the free carrier capture cross section at an ionized impurity[89].

In the case of free carrier capture process at an ionized impurity center, such a temperature dependence is explained in terms of so-called cascade capture process[85,89], in which a free carrier is initially captured into excited impurity states and cascades down a ladder of excited states with emitting phonons. The re-exciting process of a free carrier from the ladder of excited states, whose energy levels are quite close to the band edge, causes the decrease in EC cross section at high temperatures.

On the other hand, to our knowledge, we have no theoretical work on the EC process on a neutral impurity as well as that on BE and BMEC. Hence, in the present study, we have carried out a simple calculation for the phonon-assisted EC rate (cross section) at a neutral impurity in silicon. Figure 19 schematically shows the phonon-assisted EC process at a neutral impurity. In this process, an exciton $(1s,\vec{K})$, where we neglect "inter-band transitions" of an exciton such as the 1s to 2s

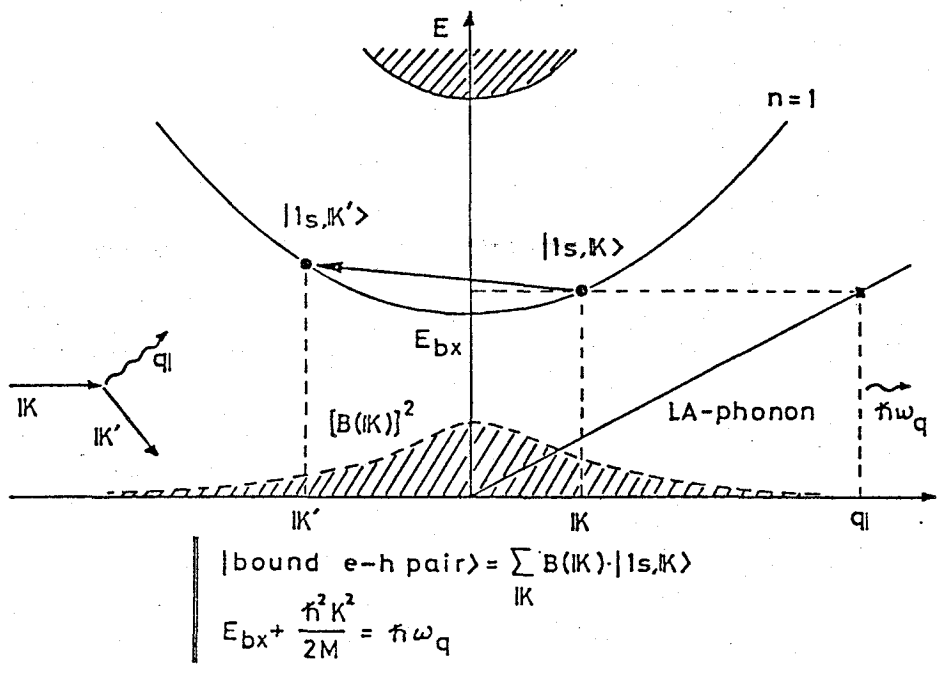

Fig. 19. Schematic representation of a LA-phonon assisted exciton-capture process at a neutral impurity center.

transition, is captured into a neutral impurity to form BE with emission of a phonon. Here, a longitudinal acoustic (LA) mode of phonon is taken into account. In the EC process involving one phonon emission to the ground BE state, the emitted phonon has the energy determined from the energy-conservation law given by $E_{bx} + \hbar^2 K^2/2M$. Simultaneously, in this process, the $(1s,\vec{K})$ exciton is scattered by the emitted phonon to the $(1s,\vec{K}-\vec{q}_f)$ exciton virtual state. It should be noted that a localized electron-hole pair state in BE, which is the final state of the EC process, can be composed of a superposition of free exciton states in the 1s exciton band.

Namely, the transition probability $W(\vec{K},\vec{q}_f)$ of the $(1s,\vec{K})$ exciton to a bound electron-hole pair state (BE state) with the emission of a phonon having the wave vector $\vec{q}_f$ is proportional to the superposition amplitude $[B(\vec{K}-\vec{q}_f)]^2$, where $B(\vec{K})$ is defined later by Eq. (3.24). Then we can get the EC cross section by averaging $W(\vec{K},\vec{q}_f)$ over $\vec{K}$ and $\vec{q}_f$, taking into account the thermal distribution function on the translational kinetic energy of an exciton and the phonon occupation number.

Here, we describe a FE creation (annihilation) operator $e^{\dagger}_{\lambda,\vec{K}}$ $(e_{\lambda,\vec{K}})$ as

$$e^{\dagger}_{\lambda,\vec{K}} = \sum_{\vec{k}_h} F_\lambda(\vec{K},\vec{k}_h)\, C^{\dagger}_{c,\vec{K}-\vec{k}_h} C_{v,\vec{k}_h} \quad , \tag{3.18}$$

where $C^{\dagger}_{\mu,\vec{k}}$ $(C_{\mu,\vec{k}})$ is an electron creation (annihilation) operator of μ-band (c indicates the conduction band and v the valence band). F_λ is a Fourier transformation of the wave function of FE $(\lambda,\vec{K})$, where λ is the hydrogenic quantum number and $\vec{K}$ is the translational wave vector. Here, we consider the 1s exciton state having the hydrogenic 1s wave function. Then, F_{1s} is written by

$$F_{1s}(\vec{K},\vec{k}_h) = \frac{8\pi^{1/2}}{(2\pi)^{3/2}a_x^{5/2}} \frac{1}{[(\beta\vec{K}-\vec{k}_h)^2+1/a_x^2]^2} \quad , \tag{3.19}$$

where a_x is the exciton Bohr radius and β is defined as $\beta = m_h/M$ ($M = m_h + m_e$, where m_e and m_h are the effective mass of an electron and a hole, respectively and we also define α as $\alpha = 1-\beta$) On the other hand, we define a creation (annihilation) operator $b^\dagger$ (b) of a electron-hole pair localized at a neutral impurity site, namely BE creation (annihilation) operator, as follows:

$$b^\dagger = \sum_{\vec{k}_e,\vec{k}_h} G(\vec{k}_e,\vec{k}_h)\ C^\dagger_{c,\vec{k}_e} C_{v,\vec{k}_h} \quad , \tag{3.20}$$

where G is a Fourier transformation of an appropriate wave function of a localized electron and a hole in the BE complex. In the definition of Eqs. (3.19) and (3.20), we consider the state composed of the filled valence band, empty conduction band and an additional neutral donor as the electronic ground state. Both spin and many-valley effects on the BE states are neglected here for simplicity.

Using the variational wave function of a bound electron and hole in the donor-BE state presented by Wünsche et al.[16] for the calculation of the exciton binding energy of BMEC, G is written by

$$G(\vec{k}_e,\vec{k}_h) = \frac{1}{(2\pi)^3} g_e(\vec{k}_e)\ g_h(\vec{k}_h)$$

$$g_e(\vec{k}_e) = \frac{8\pi^{1/2}}{a_{bx}^{5/2}} \frac{1}{[k_e^2 + 1/a_{bx}^2]^2} \quad , \tag{3.21}$$

$$g_h(\vec{k}_h) = \frac{8\pi^{1/2}}{3^{1/2}b_{bx}^{5/2}} \frac{3/b_{bx}^2 - k_h^2}{[k_h^2 + 1/b_{bx}^2]^2} \quad , \tag{3.22}$$

where a_{bx} and b_{bx} is the Bohr radius of an electron and a hole in the BE complex, respectively. The bound electron-hole pair creation operator $b^{\dagger}$ can be expanded in terms of the exciton creation operator $e^{\dagger}_{1s,\vec{K}}$ as

$$b^{\dagger} = \sum_{\vec{K}} B(\vec{K})\ e^{\dagger}_{1s,\vec{K}} \quad , \tag{3.23}$$

where the amplitude B is obtained by using Eqs. (3.18) and (3.20) as

$$B(\vec{K}) = \sum_{\vec{k}_h} F_{1s}(\vec{K},\vec{k}_h)\ G(\vec{K}-\vec{k}_h,\vec{k}_h) \quad . \tag{3.24}$$

Then, we introduce the transition probability of the $(1s,\vec{K})$ exciton to a bound electron-hole pair (BE state) based on the exciton-acoustic phonon interaction formula presented by Toyozawa[90,91]. The exciton-phonon interaction Hamiltonian H_{ex-ph} can be expresses in the second quantization formula as

$$H_{ex-ph} = i \sum_{\vec{q},\vec{K},\lambda,\lambda',\nu} V_{\nu}^{\lambda,\lambda'}(\vec{q})\ (a_{\vec{q}} - a^{\dagger}_{-\vec{q}})\ e^{\dagger}_{\lambda',\vec{K}+\vec{q}}\, e_{\lambda,\vec{K}} \quad . \tag{3.25}$$

Here, $a^{\dagger}_{\vec{q}}$ $(a_{\vec{q}})$ is a creation (annihilation) operator of a phonon with the wave vector $\vec{q}$. ν is a mode of the interacting phonon. When the LA mode of phonon is taken into account, the magnitude of the exciton-phonon coupling V is formulated as, based on the deformation potential approximation[92].

$$V_{LA}^{\lambda,\lambda'}(\vec{q}) = (\hbar q/2\rho C_s V_c)^{1/2}[D_v v_h(\vec{q}) - D_c v_e(\vec{q})] \quad , \tag{3.26}$$

where D_c and D_v is the deformation potential (dilatational) constant of

the relating valence and conduction band, respectively. ρ is the mass density and C_s is the sound velocity. v_e and v_h is written, in the case of "intra-band transition" of FE, namely $\lambda=\lambda'=1s$, as follows:[90]

$$v_e(\vec{q}) = [1 + (\beta q a_x/2)^2]^{-2} , \quad v_h(\vec{q}) = [1 + (\alpha q a_x/2)^2]^{-2} . \quad (3.27)$$

Taking into account the exciton-LA phonon interaction, the transition probability of the $(1s,\vec{K})$ exciton to a localized electron-hole pair state (BE state) is described as

$$W(\vec{K}) = \frac{2\pi}{\hbar} \int |M(\vec{K},\vec{q}_f)|^2 \, \mathcal{D}_{ph}(\vec{q}_f) \, \delta(E_f - E_i) \, d\vec{q}_f \quad . \quad (3.28)$$

$\mathcal{D}_{ph}$ is the phonon density of states given by $V_c/(2\pi)^3$, where V_c is the volume of the crystal. $M(\vec{K},\vec{q}_f)$ is the transition matrix element. Here, assuming the parabolic exciton band, we obtain

$$E_f - E_i = \hbar^2 K^2/2M + E_{bx} - \hbar\omega_{ph}(\vec{q}_f) \quad . \quad (3.29)$$

E_{bx} is the exciton-binding energy of BE concerned and $\hbar\omega_{ph}(\vec{q}_f)$ is the energy of the emitted phonon with the wave vector $\vec{q}_f$, which is approximated in the small wave vector limit (elastic approximation) as $\hbar C_s q_f$. The matrix element is calculated as

$$M(\vec{K},\vec{q}_f) = i \, B(\vec{K}-\vec{q}_f) \, V_{LA}^{1s,1s}(-\vec{q}_f) \, [n_j(\vec{q}_f) + 1]^{1/2} \quad , \quad (3.30)$$

where n_j is the phonon occupation number written, in the thermal

average, as

$$n_j(\vec{q}_f)_{av} = [\exp(\hbar\omega(\vec{q}_f)/k_BT) - 1]^{-1} \quad . \tag{3.31}$$

Using the transition probability $W(\vec{K})$, the change in the density of FE by the EC process at a neutral impurity center in a time Δt is obtained as

$$\Delta N(t) = \int [N_x(\vec{K},t+\Delta t) - N_x(\vec{K},t)]\, d\vec{K} \simeq \int [\frac{\partial N_x(\vec{K},t)}{\partial t}]\, \Delta t\, d\vec{K}$$

$$= - \int [W(\vec{K})N_x(\vec{K},t)N_I]\, \Delta t\, d\vec{K} \quad . \tag{3.32}$$

Here, $N_x(\vec{K},t)$ is the <u>occupied</u> density of the $(1s,\vec{K})$ exciton state at time t and N_I is the density of the <u>empty</u> neutral impurity center. Then, $N_x(\vec{K},t)$ is written in the conventional formula described as

$$N_x(\vec{K},t) = N(t)\, \zeta_0 \exp[-\varepsilon_{kin}(\vec{K})/k_BT] \quad , \tag{3.33}$$

where $\varepsilon_{kin}(\vec{K}) = \hbar^2K^2/2M$ is the kinetic energy the of $(1s,\vec{K})$ exciton. N(t) is the total FE density given by

$$N(t) = \int N_x(\vec{K},t)\, d\vec{K} \quad . \tag{3.34}$$

ζ_0 is described as

$$\zeta_0 = \frac{h^3}{(2\pi Mk_BT)^{3/2}} \quad . \tag{3.35}$$

Here, we define the EC rate at a neutral impurity center which satisfies the following relation;[93]

$$\frac{\Delta N(t)}{\Delta t} = - C_0 N(t) N_I \quad , \tag{3.36}$$

as appeared in the kinetic equation of (3.4). Thus, substituting Eqs. (3.33) and (3.35) into Eq. (3.32), the EC rate at a neutral impurity C_0 is given as a function of temperature T by

$$C_0(T) = \frac{h^3}{(2\pi M k_B T)^{3/2}} \int W(\vec{K}) \exp[-\varepsilon_{kin}(\vec{K})/k_B T] \, d\vec{K} \quad . \tag{3.37}$$

Furthermore, the average EC cross section $\sigma_0(T)$ at a neutral impurity is obtained as

$$\sigma_0(T) = C_0(T)/V_{th}(T) = \frac{h^3}{8\pi M (k_B T)^2} \int W(\vec{K}) \exp[-\varepsilon_{kin}(\vec{K})/k_B T] \, d\vec{K}, \tag{3.38}$$

where $V_{th}(T)$ is the average thermal velocity of FE given by

$$V_{th}(T) = (8 k_B T/\pi M)^{1/2} \quad . \tag{3.39}$$

Typical results of the calculated values of the square of the superposition amplitude $[B]^2$ of BE defined by Eq. (3.24) and the transition probability W of the $(1s,\vec{K})$-exciton to the bound electron-hole pair (BE) state in Si:P as a function of K along the (100) direction are shown in Fig. 20. Here, in these calculations, we consider the A_0 type process (See Fig. 16) in which an exciton is captured into a neutral phosphorus impurity to form a BE in the ground state, namely ground

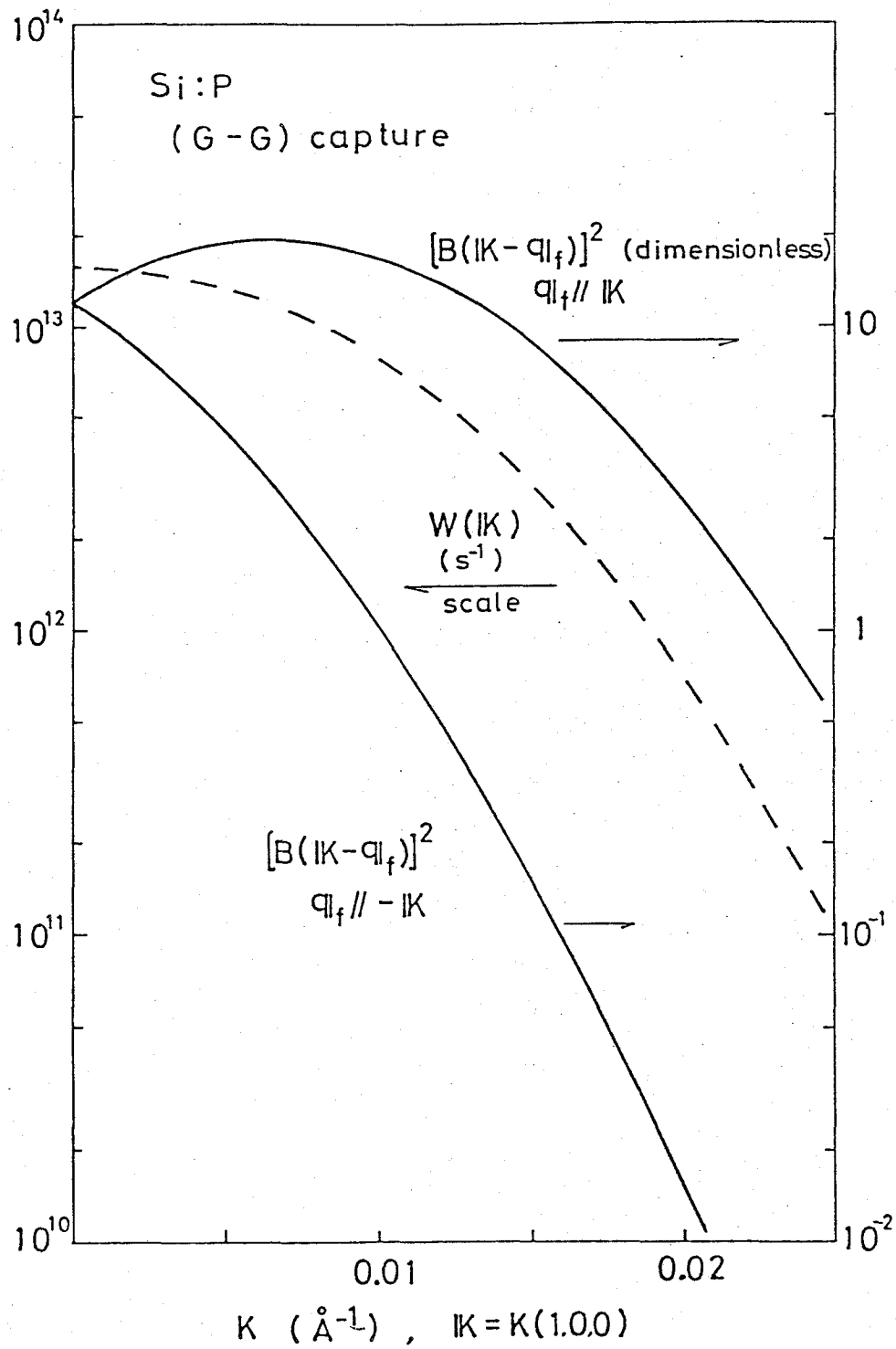

Fig. 20. Calculated results of transition (capture) probability W(K) of (1s,K) exciton state to a bound exciton (localized electron-hole pair) state. Calculated curve of $[B(K)]^2$, the square of an expansion coefficient in the form of Eq. (3.23) is also shown (solid curve) .

state (neutral impurity) to ground state (BE state) capture process denoted as (G-G) captute. Although we have to take into account the cascade type EC process shown by B_0 in Fig. 16 to get the reliable value of the EC cross section, it is found that the calculated EC cross section of Si:P taking into account the A_0 type transition decreases with increasing temperature, varying in about one order of magnitude from 4.2K to 30K, which is consistent with the experimental observation[88].

CHAPTER IV

PHOTOLUMINESCENCE METHOD OF ESTIMATING IMPURITY CONTENTS AND DOPANT COMPENSATION RATIO

Characterization of semiconductor materials is particularly important in the development of semiconductor devices[23,24]. Various kinds of electrical [94] and optical [25,26] techniques of semiconductor material characterization have been utilized so far. Especially, recent progress in LSI technology demands nearly-perfect silicon single crystals and therefore great improvement of analysis methods for a small amount of impurities and defects involved in silicon crystal is required. For this purpose, optical techniques such as photoluminescence are promising because of its inherently high sensitivity to impurities and defects[25]. Photoluminescence has been previously used for the identification of impurities involved but rarely used for the quantitative characterization of the impurity concentration except that an attempt of determining the dopant impurity concentration of relatively high-purity silicon has recently been reported.[95] This is due to the fact that photoluminescence spectra of silicon change drastically with excitation level, dopant concentration, compensation ratio and so on. Hence, in order to utilize photoluminescence for the characterization of silicon crystal, a through understanding for the relations between observed photoluminescence and such parameters as mentioned above is neccessary.

In the previous chapter, we have proposed a model for the recombination kinetics in the whole system including FE, BE and BMEC, and found that the excitation-level and dopant-concentration dependence of

these luminescence intensities can be consistently explained by the results calculated from the rate equations based on the model. In the limit of very low excitation level, some of FEs generated by the irradiation of the excitation light recombine radiatively, that is the FE luminescence, and the rest of generated FEs is captured by donor or acceptor impurities involved, resulting in BE whose radiative recombination is the BE luminescence. In this simple case, the density of BE is approximately proportional to the density of FE and impurity center. Therefore, if we measure the luminescence-intensity ratio of BE to FE taken at very low excitation levels, we can estimate the impurity content involved in the sample from a simple analysis of the ratio.

However, this simple relation is not always valid over a wide range of excitation level. At high excitation levels, some of FEs are captured by impurity centers and other FEs are also captured by BE formed already, leading to the formation of BMEC. Hence the problem becomes more complicated in the case of such high excitation levels. To clarify the details of the exciton luminescence of silicon and to develop an analysis method of photoluminescence for the purpose of characterization of silicon single crystal, we have studied theoretically and experimentally the FE and BE luminescence as a function of excitation intensity and dopant impurity content[27]. As a result, we have found a method of determining directly the dopant (boron and phosphorus) content and the compensation ratio in relatively high-purity silicon single crystals.

IV-1. formulation of the luminescence-intensity ratio of BE to FE

In this section, we express the luminescence-intensity ratio of BE to FE in the analytical form on the basis of the model for the formation and decay kinetics of FE, BE and BMEC, which was proposed in the previous chapter for the interpretation of the excitation-intensity and dopant-content dependence of the BMEC luminescence of silicon. The rate equation at the steady-state condition for the density of BE is written as follows:

$$0 = \frac{\partial n_1}{\partial t} = C_0 N n_0 - (C_1 N + W_1) n_1 + W_3 n_3 \quad , \tag{4.1}$$

where n_m is the density of the m-th BMEC (n_0 denotes that of neutral impurity and n_1 that of BE) and N is the density of FE. C_m is the EC rate on the m-th BMEC. W_m is the AR rate of the m-th BMEC.

Here we define the luminescence-intensity ratio of BE to FE as

$$R_{b/f}(q,q') = I(\,BE_q\,)/I(\,FE_{q'}) \quad . \tag{4.2}$$

$I(BE_q)$ and $I(FE_{q'})$ indicate the luminescence intensity of BE with emission of a momentum-conserving phonon q and that of FE with emission of a phonon q', respectively. When we estimate the luminescence intensity ratio from the peak heights of the luminescence lines for both BE and FE, $R_{b/f}$ is expressed as

$$R_{b/f} = \frac{n_1}{N} W_{b/f}(q,q') \quad . \tag{4.3}$$

Here, $W_{b/f}$ denotes the ratio of the radiative recombination rate of BE to FE, which can be written as

$$W_{b/f}(q,q') = \frac{|M_{bx}(q)|^2}{|M_x(q')|^2}\frac{\hbar\omega_q}{\hbar\omega_{q'}}\frac{\pi^{1/2}(k_BT)^{3/2}}{2(2\pi)^{1/2}\sigma_{bx}(q)}\frac{1}{\mathcal{F}(\hbar\omega_{q'};\sigma_x)}, \quad (4.4)$$

where $M_{bx}(q)$ and $M_x(q')$ are the momentum matrix element for BE recombination with emission of phonon q and that for FE recombination with emission of a phonon q', respectively. $\hbar\omega_q$ and $\hbar\omega_{q'}$ are the corresponding transition energy at the peak position of the luminescence spectra of BE and FE. The factor $(\sqrt{\pi}/2)(k_BT)^{3/2}$ is introduced by considering the thermal distribution function on the kinetic energy of FE , the details of which was discussed by Williams and Bebb[96], and the factor disappears if we consider the integrated luminescence intensity of FE instead of the peak height of the luminescence line. σ_{bx} is the Gaussian-broadening factor inherent to the BE-recombination line with emission of a phonon q. Then, we define a line-shape function of FE recombination line as[39,50]

$$\mathcal{F}(\hbar\omega;\sigma_x) = \int_{E_{th}}^{\infty} (E-E_{th})^{1/2}\exp[-(E-E_{th})/k_BT]\,\mathcal{G}(\hbar\omega-E)\,dE \quad . \quad (4.5)$$

In this formula, we consider a Gaussian-broadening function written by

$$\mathcal{G}(\hbar\omega-E) = \frac{1}{(2\pi)^{1/2}\sigma_x(q')}\exp\frac{-(\hbar\omega-E)^2}{2[\sigma_x(q')]^2} \quad , \quad (4.6)$$

where $\sigma_x(q')$ is the Gaussian-broadening factor inherent to the FE recombination. E_{th} is the threshold energy of a FE luminescence line associated with the momentum-conserving phonon q' described as

$$E_{th} = E_{gx} - \hbar\omega_{ph}(q') \quad , \quad (4.7)$$

where E_{gx} is the exciton energy gap and $\hbar\omega_{ph}(q')$ is the energy of the momentum-conserving phonon q'. The calculated values of $W_{b/f}(q,q')$ for both boron and phosphorus are shown in Table IV. Parameters used in the calculations are also listed in Table V.. Here remark should be made for the slit width and resolution of the spectrometer employed. It is not practical to measure luminescence spectra with extremely high resolution for the analysis of the weak exciton luminescence intensity in the range of low excitation levels. Therefore the slits of the spectrometer should be set to an appropriate width for measurements. In this case, the intrinsic broadening factors, σ_{bx} and σ_x, in $W_{b/f}$ defined by Eq. (4.4) should be replaced by those including spectrometer broadening.

On the other hand, the density ratio of BE to FE, n_1/N, can be obtained by solving Eq. (4.1) and written as

$$\frac{n_1}{N} = \frac{C_0 N_1}{W_1} \frac{1}{1 + [(C_0+C_1)/W_1]\, N} \quad , \tag{4.8}$$

in the low-excitation condition, where one can approximate as $n_0+n_1 \simeq N_1$ and $C_0 N n_0 >> W_3 n_3$ in Eq. (4.1). From Eqs. (4.3) and (4.8), the luminescence intensity ratio $R_{b/f}$ is expressed as a function of impurity content and excitation intensity I_e as follows:

$$R_{b/f}(q,q') = \frac{C_0 N_1}{W_1} W_{b/f}(q,q') \frac{1}{1 + [(C_0+C_1)/W_1] K\tau_{eff} I_e} \tag{4.9}$$

As mentioned in the previous section, τ_{eff} is the effective lifetime of FE and it depends on dopand content (See Eq. (3.10)). Here we define $R^0_{b/f}$, which is the value of $R_{b/f}$ in the limit of I_e=0, as

Table. IV Calculated values of $W_{b/f}(q,q')$ defined by Eq.(4.4).

Boron-BE	Phosphorus-BE
$W_{b/f}(TO,TO) = 6.073$	$W_{b/f}(TO,TO) = 1.482$
$W_{b/f}(TA,TA) = 34.34$	$W_{b/f}(NP,TA) = 176.8$

Table. V Parameters for the exciton luminescence in silicon used for determination of $W_{b/f}(q,q')$.

	Boron-BE			Phosphorus-BE			FE	
	TO	TA	NP	TO	TA	NP	TO	TA
$\hbar\omega_q$ (meV)	1092.9	1132.2	1150.9	1092.3	1131.5	1150.2	1097.0	1136.2
$\sigma(q)$ * (meV)	0.117	0.0820	-	0.0909	0.0692	0.0212	0.31	0.21
$\lvert M(q)\rvert^2 \times 10^8$ ** $(\hbar/\mathring{A})^2$	201	24.9	4.83	38.0	3.57	32.6	132	3.47

* Value of $\sigma(q)$ for BE recombination luminescence is calculated from the half width of the BE luminescence line(ref. 98 and 65). And the broadening parameter obtained from the analysis of the wavelength derivative spectra(ref. 97) is used for $\sigma(q)$ of FE luminescence.

** The square of momentum matrix element $\lvert M(q)\rvert^2$ for BE recombination is calculated from the oscillator strength of BE transition measured by Dean et al.(ref. 49). And that for FE recombination is calculated from the interband-transition matrix element of indirect absorption obtained by Nishino et al(ref. 97).

$$R^0_{b/f} = \frac{C_0 N_I}{W_I} W_{b/f}(q,q') \quad . \tag{4.10}$$

Thus, we have obtained the theoretical formula of luminescence-intensity ratio of BE to FE, defined here as $R_{b/f}$, as a function of excitation-level I_e and dopant content N_I, and therefore we can characterize the dopant impurity content on the basis of the theoretical formula, which will be shown in the following sections.

IV-2. determination of parameters involved in FE and BE recombination processes

To analyze the dopant impurity content based on Eq. (4.9), some recombination parameters in EC and AR processes need to be determined. Recently, the recombination rates of BE in silicon have been precisely studied by Schmid[81] and Osbourn et al.[99,100] for various kinds of common group-III and V impurities. The results show that the recombination rate of BE in silicon is essentially determined by a phononless Auger recombination process and strongly depends on the ionization energy of a donor and an acceptor.

On the other hand, we have no available data of such EC rates concerned with common group-III and V impurities in silicon. Hence, in this work, we have determined the EC rates at neutral impurities, boron and phosphorus, which are common dopants used for IC technology, from the analysis of excitation-level dependence of the BE and FE-luminescence intensity. These measurements have been made for high-purity (standard) samples. For this purpose, Eq. (4.9) is rewritten as

$$[R_{b/f}(q,q')]^{-1} = [R^0_{b/f}(q,q')]^{-1}[1 + \frac{C_0+C_I}{W_I} K\tau_{eff} I_e] \quad , \tag{4.11}$$

This equation shows that the inverse luminescence-intensity ratio, $R_{b/f}^{-1}$, is a linear function of the excitation intensity I_e. The experimental data of excitation-level dependence of $[R_{b/f}(TA,TA)]^{-1}$ for boron and $[R_{b/f}(NP,TA)]^{-1}$ for phosphorus taken at liquid helium temperature are shown in Fig. 21. Note that the data points of $R_{b/f}^{-1}$ are well on straight lines for both boron and phosphorus. This fact shows that the excitation-level dependence of $R_{b/f}$ is well described by Eq. (4.11). Hence, from the intersections on the vertical scale in the figure, we can estimate the value of $R_{b/f}^{0}$. Using the value of $R_{b/f}^{0}$, the EC rate C_0 at a neutral boron and phosphorus impurity can be determined on the basis of Eq. (4.10). The obtained values of C_0 are shown in Table III of the previous chapter.

IV-3. excitation-level dependence of the luminescence-intensity ratio of BE to FE

In this section, the excitation-level dependence of the luminescence intensity ratio of BE to FE is analyzed in detail on the basis of the theoretical formula shown in the previous sections. Figure 22 shows the plots of the measured luminescence intensity of BE and FE as a function of excitation intensity in a Si:B sample having the relatively large amount of compensating phosphorus impurity. It should be noted that there is a clear difference in the excitation-intensity dependence between the BE and FE luminescence lines. The luminescence intensity of FE varies linearly with excitation intensity in this range of excitation levels, while that of BE increases linearly only at low excitation levels and gradually saturates with increasing excitation intensity for both phosphorus and boron BE. This difference in the

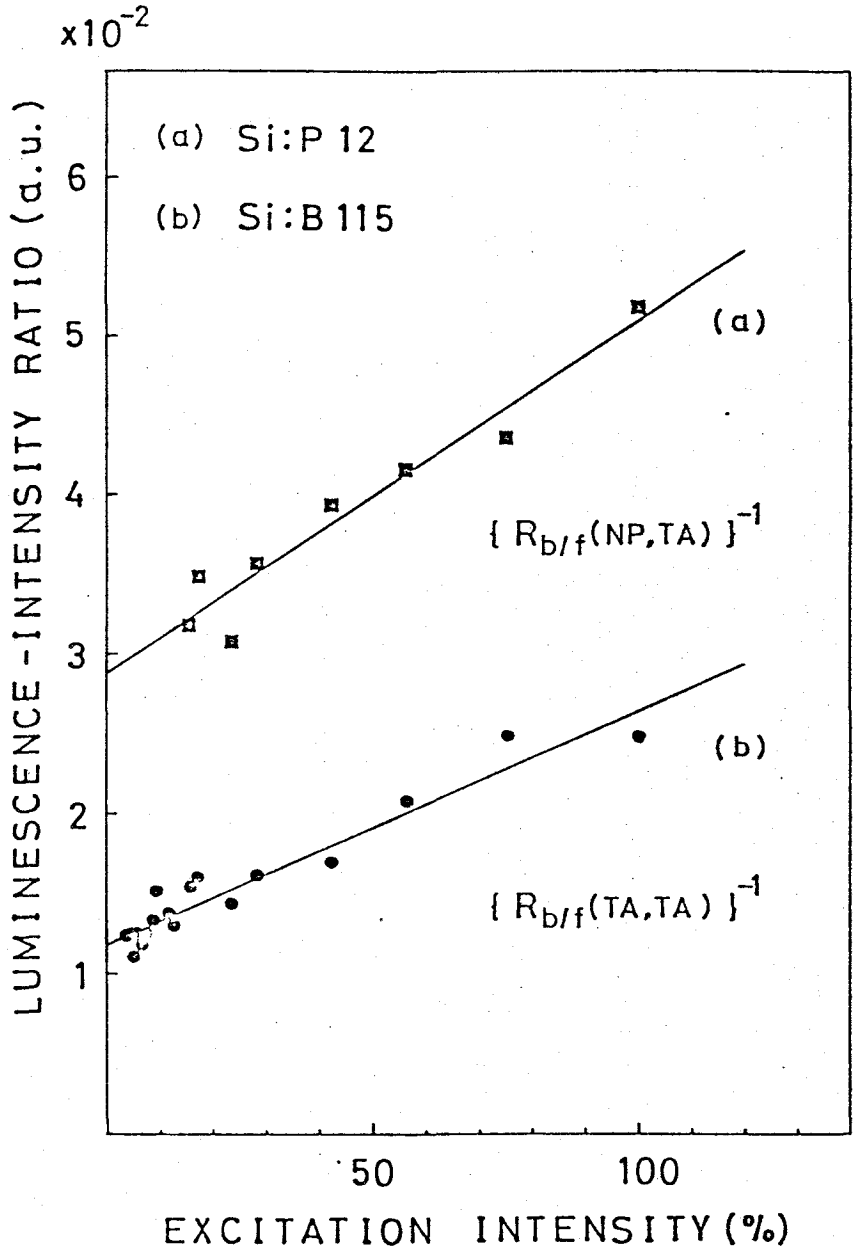

Fig. 21. Plots of the luminescence-intensity ratio $[R_{b/f}(q,q')]^{-1}$ as a function of excitation intensity. Straight lines are drawn by a least-square fitting to the data points.

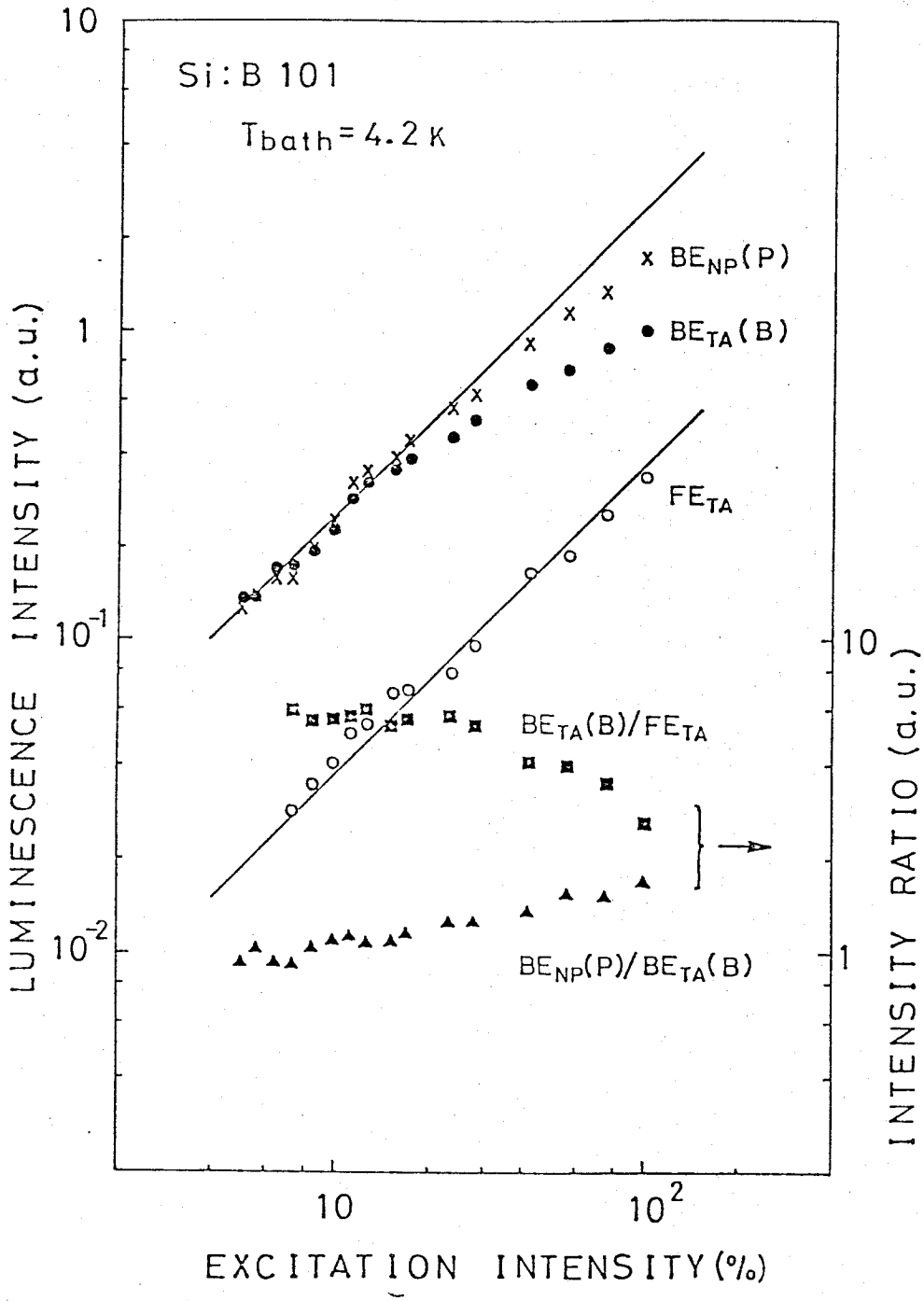

Fig. 22. Plots of the luminescence intensity of bound exciton, free exciton and their ratio for Si:B as a function of excitation level. Straight lines with the slope of 1 are shown to demonstrate the difference in the excitation-level dependence between free exciton and bound exciton luminescence.

excitation-level dependence between the BE and FE luminescence lines causes their ratio $R_{b/f}$ to decrease with increasing excitation intensity.

The density of FE is described as $N = K\tau_{eff} I_e = K(W_f + C_0 N_I)^{-1} I_e$ under the range of low excitation levels employed here, as discussed in the previous chapter. Therefore the FE luminescence intensity increases linearly with excitation level I_e in the excitation range under consideration. However, it is not the case at sufficiently high excitation levels where luminescence bands due to EHD are observed, probably two orders of magnitude higher excitation levels than the 100 % excitation level (1.5 $W.cm^{-2}$) in this work. Under such high excitation levels, the FE-luminescence intensity also saturates while the EHD luminescence grows rapidly[8].

The saturation behavior of BE luminescence at high excitation levels as observed in Fig. 22 is due to the fact that the most part of impurity centers contained in the crystal become saturated by the formed BE and BMEC at high excitation levels. We have theoretically calculated the luminescence intensity ratio $R_{b/f}$ of BE to FE as a function of excitation intensity in the wide range of excitation intensity, which is shown in Fig. 23. The calculated curves in Fig. 23 are obtained by numerically solving the rate equations (3.3)-(3.5), taking into account BMEC A^0X^2 and A^0X^3 as well as FE and BE, for Si:B with two different boron contents.

Strictly speaking, the present rate equations do not consider effects of EHD formation and therefore are not applicable to the high excitation regime where the EHD luminescence appeares. However, the caluculated curves shown in FIg. 23 is still useful for the explanation of the excitation behavior of the luminescence-intensity ratio of BE to FE in this excitation range. As can be seen in this figure, the value of

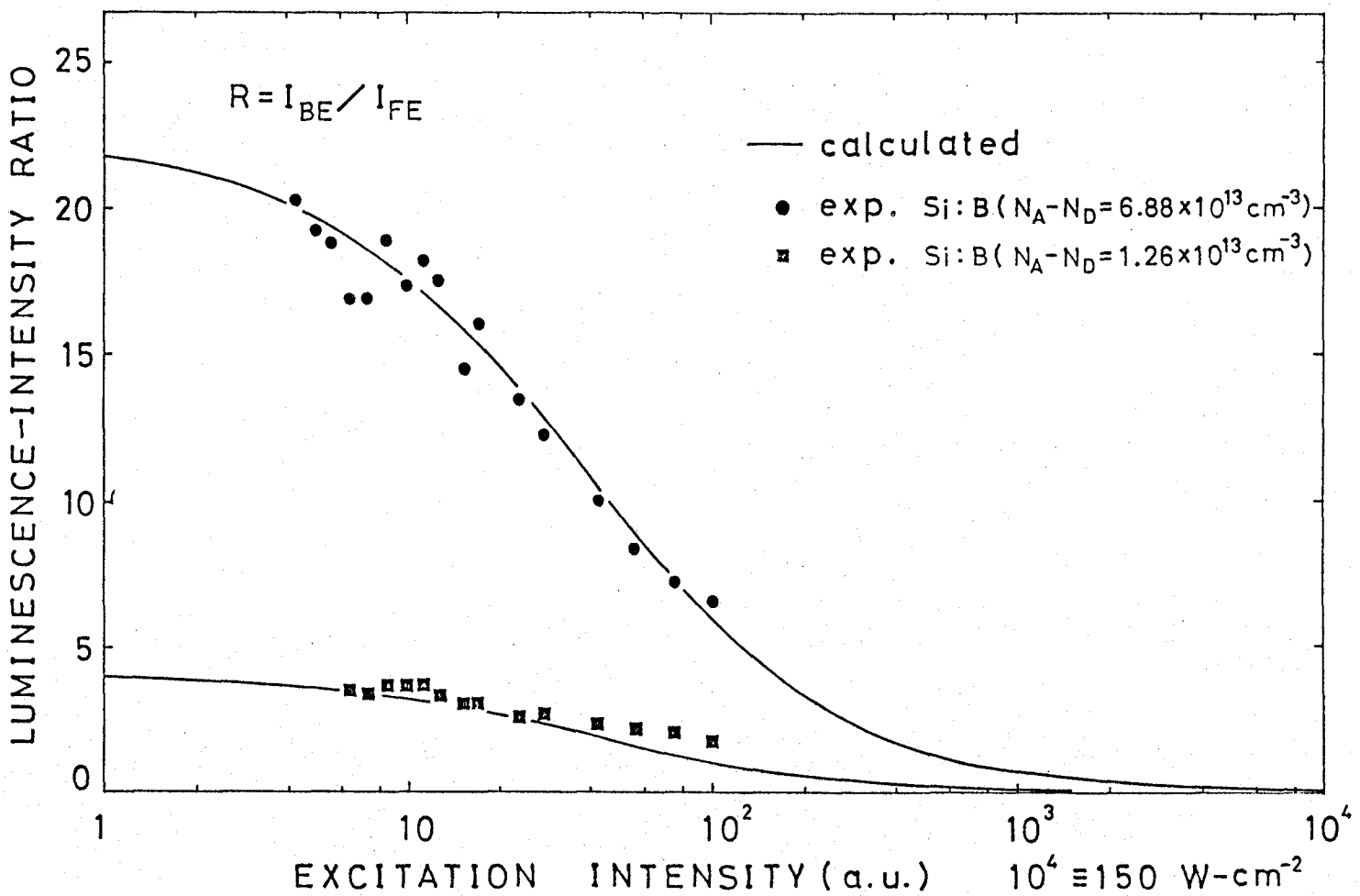

Fig. 23. Plots of luminescence-intensity ratio of bound exciton to free exciton as a function of excitation intensity. Solid curves are theoretically calculated values of the luminescence-intensity ratio.

$R_{b/f}$ is nearly constant at low excitation levels ranging from 0.015 to 0.15 $W.cm^{-2}$ and rapidly decreases with increasing excitation intensity from this low excitation range. Excellent agreement between theoretically calculated curves of $R_{b/f}$ and the experimental data is obtained at the excitation levels below 1.5 $W.cm^{-2}$, showing that the luminescence intensity ratio $R_{b/f}$ is well described by the present rate equations or the derived formula (4.9). Therefore, we can estimate dopant contents by analyzing such plots of $R_{b/f}$ in the excitation range below 1.5 $W.cm^{-2}$ on the basis of the theoretical formula Eq. (4.9) for the luminescence intensity ratio $R_{b/f}$ of BE to FE.

Recently, Tajima[95)] has studied the dopant-concentration dependence of the luminescence-intensity ratio of BE to FE at relatively high excitation levels, 100 - 200 $W.cm^{-2}$, for boron- or phosphorus-doped silicon. He found that plots of the luminescence-intensity ratio of BE to FE versus the net dopant concentration are well on certain specific lines in double-logarithmic scale for both boron- and phosphorus-doped silicon, and proposed that such plots can be used as calibration curves for determining the dopant concentration of silicon. However, at high excitation levels around 100 $W.cm^{-2}$ the EHD luminescence components are generally observed. In such a high excitation region where EHD is formed in the crystal, the luminescence intensities of FE and BE are strongly influenced by the density of EHD as previously reported by Pokrovskii[8)], and hence the luminescence-intensity ratio of BE to FE becomes a complicated function of excitation intensity and impurity concentration. The theoretical analysis is unfortunately impossible because a through understanding for the influence of EHD formation to the luminescence of FE and BE or their ratio is not established at the

present stage. Therefore, it is impossible to examine theoretically the calibration curves proposed by Tajima[95]. Furthermore, as he pointed in his paper, such calibration curves cannot be used for samples with large dopant compensation ratio.

On the other hand, the theoretical background for the excitation-intensity and dopant-content dependence of the luminescence-intensity ratio of BE to FE measured at low excitation levels is well established in terms of the rate equations proposed in this work[27]. Therefore, data of the luminescence intensity ratio of BE to FE can be analyzed for the purpose of characterization of the content of impurity involved in high-purity silicon single crystals even if those contain a large amount of compensating impurities, which is shown in the following sections.

IV-4. photoluminescence characterization of dopant impurity contents in silicon

As mentioned in the previous sections, the luminescence-intensity ratio of BE to FE is described by Eq. (4.9) in the range of low-excitation levels below 1.5 $W.cm^{-2}$. From plots of $R_{b/f}^{-1}$ versus I_e, we can estimate precisely the value of $R_{b/f}^0$ from the intersection on the vertical scale of the plots (See Fig. 21). It should be noted here that the value of $R_{b/f}^0$ is essentially determined by dopant concentration N_I and independent of the compensating impurities as can be seen from Eq. (4.9). Hence, using the value of $R_{b/f}^0$, the dopant content can be easily estimated by using Eq. (4.10) as

$$N_I = \frac{W_I}{W_{b/f}(q,q')C_0} R_{b/f}^0(q,q') \quad . \qquad (4.12)$$

The numerical factors in Eq. (4.12) are calculated from the data in Table II, III and IV. Here, we obtain the calibration relations for dopant phosphorus and boron contents in silicon as follows:

$$N_{boron} = 1.368 \times 10^{12} \; R^{0}_{b/f}(TA,TA) \quad cm^{-3} \quad , \tag{4.13}$$

$$N_{phos.} = 8.171 \times 10^{10} \; R^{0}_{b/f}(NP,TA) \quad cm^{-3} \quad . \tag{4.14}$$

For simplicity, $R^{0}_{b/f}$ values can be also approximately obtained directly by the measured luminescence-intensity ratio taken at sufficiently low excitation levels below 0.15 $W.cm^{-2}$ without using plots shown in Fig. 21. As is shown in Figs. 22 and 23, the luminescence intensity ratio $R_{b/f}$ remains nearly constant in the excitation range below 0.15 $W.cm^{-2}$. If we use the value of $R_{b/f}$ at the 10 % excitation level (0.15 $W.cm^{-2}$) in place of $R^{0}_{b/f}$, it causes the error of about 15 % for the dopant contents (underestimation) in silicon crystals. The data of the dopant content of silicon measured by the above-mentioned calibration relations are listed in Table VI.

IV-5. effects of dopant compensation

The existence of compensating impurities primarily induces an additional decay channel of FE and consequently causes the reduction of the steady-state FE density. In this case, the FE recombination rate W_f should be replaced by W_f' described as

$$W_f = W_f + \sum C_m' n_m' \simeq W_f + C_0' N_I' \quad , \tag{4.15}$$

Table. VI Results of photoluminescence analysis for the dopant concentration (N_A, N_D) and compensation ratio(N_D/N_A) of silicon single crystals.

Sample	Photoluminescence			Van der Pauw
	N_A (cm^{-3})	N_D/N_A (%)	$N_A - N_D$ * (cm^{-3})	$N_A - N_D$ (cm^{-3})
B112	2.29×10^{11}			4.56×10^{11}
B101	4.00×10^{13}	34.2	2.63×10^{13}	1.26×10^{13}
B111	1.03×10^{14}	27.6	7.46×10^{13}	2.04×10^{13}
B113	1.67×10^{14}	4.05	1.60×10^{14}	6.88×10^{13}
B114	3.15×10^{14}	2.43	3.07×10^{14}	1.65×10^{14}
B115	4.64×10^{14}	2.43	4.53×10^{14}	5.50×10^{14}
B116	9.72×10^{14}	0.466	9.67×10^{14}	1.15×10^{15}
P12	4.31×10^{13} (N_D)			4.60×10^{13} ($N_D - N_A$)

* These values are calculated using the values of N_A and N_D/N_A obtained from photoluminescence analysis.

where C_m' and n_m' are the EC rate and the density of the m-th BMEC concerned with a compensating impurity, respectively. N_I' is the content of the compensating impurity.

Effects of the inclusion of compensating impurities on the excitation-intensity dependence of the luminescence-intensity ratio of BE to FE concerned with majority impurity (boron) are shown in Fig. 24. Solid curves in the figure were theoretically calculated by the rate equations (3.3)-(3.5) taking into account the densities of BMEC A^0X^2 and A^0X^3 as well as those of FE and BE. Phosphorus impurity is considered to be a compensating impurity here. Calculations were done for several values of compensation ratio. It has been found that experimental points are well fitted to a calculated curve with the compensation ratio N_D/N_A = 0.321, where N_A and N_D denote the dopant boron content and the compensating phosphorus content, respectively The data of Fig. 24 show several significant facts; (1) The luminescence-intensity ratio $R_{b/f}$ remains nearly constant at low excitation levels below 0.15 $W.cm^{-2}$ and further it is nearly independent of the dopant compensation ratio in this excitation range. (2) The $R_{b/f}$ value decreases with increasing excitation intensity beyond this excitation range and the decrease rate strongly depends on the compensation ratio.

Agreement between the calculated curve of $R_{b/f}$ and the experimental data obtained in this figure shows that we can estimate the compensation ratio of the sample from this fitting procedure to the $R_{b/f}$ versus I_e plots although this technique is somewhat complicated. Therefore we consider more simple method of estimating the dopant compensation ratio directly by the BE luminescence intensity ratio of majority dopant to compensating impurity.

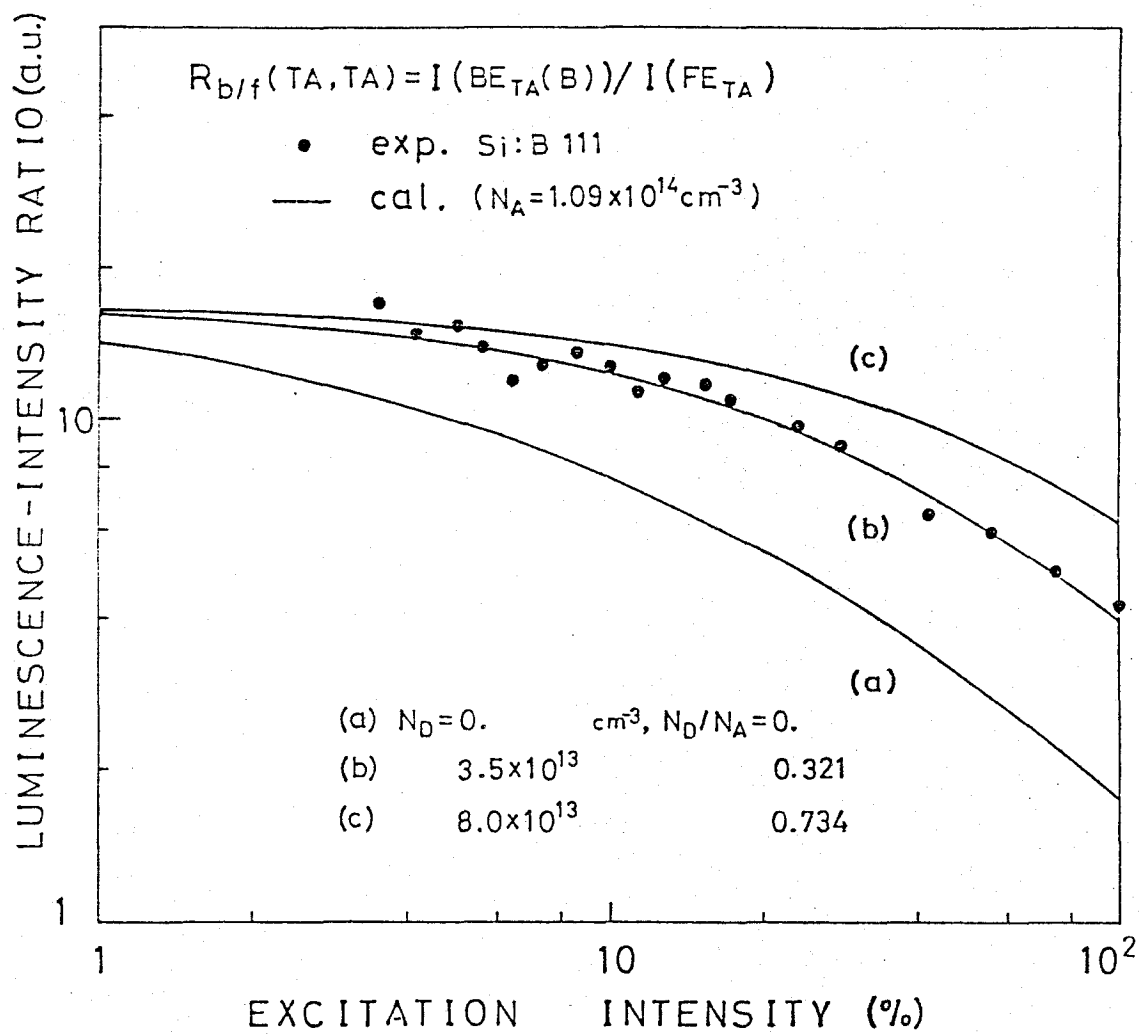

Fig. 24. Plots of the luminescence-intensity ratio of bound exciton to free exciton as a function of excitation intensity. Solid curves are theoretically calculated for several values of dopant comensation ratio.

Here we consider a compensated Si:B crystal with the inclusion of phosphorus impurity since phosphorus is one of the most probable compensating impurity in Si:B crystals. Then we define the luminescence-intensity ratio of phosphorus and boron BE luminescence lines given by

$$r_{P/B}(q',q) = I(\ BE_{q'}(P)\ )/I(\ BE_q(B)\ ) \quad . \tag{4.16}$$

The ratio $r_{P/B}$ is written similarly to the ratio $R_{b/f}$ as follows:

$$r_{P/B}(q',q) = r^0_{P/B}(q',q)\ \frac{1 + [(C_0+C_1)/W_1]K\tau_{eff}I_e}{1 + [(C_0'+C_1')/W_1']K\tau_{eff}I_e} \quad , \tag{4.17}$$

where $r^0_{P/B}(q',q)$ is defined as

$$r^0_{P/B}(q',q) = \frac{N_D}{N_A}\ \frac{C_0'W_1W_{b/f}'(q',q'')}{C_0W_1'W_{b/f}(q,q'')} \quad . \tag{4.18}$$

As already shown in Fig. 22, the luminescence-intensity ratio $r_{P/B}$ is nearly independent of the excitation intensity in the low excitation range below 0.15 $W.cm^{-2}$ though it slightly changes at higher excitation levels, which is also consistent with the theoretical prediction from Eq. (4.17). Therefore the value of $r^0_{P/B}$ can be easily estimated from the $r_{P/B}$ versus I_e plots. Using Eq. (4.17), the compensation ratio N_D/N_A can be obtained as follows.

$$\frac{N_D}{N_A} = \frac{C_0W_1'W_{b/f}(q,q'')}{C_0'W_1W_{b/f}(q',q'')}\ r^0_{P/B}(q',q) \quad . \tag{4.19}$$

The numerical factors in Eq. (4.19) are calculated by using the data in Tables II, III and IV, and Eq. (4.19) is rewritten as

$$\frac{N_D}{N_A} = 5.975 \times 10^{-2}\, r^0_{P/B}(NP.TA) \quad . \tag{4.20}$$

Form this simple relation for the BE-luminescence ratio, we can easily estimate the compensation ratio of phosphorus to boron or vice versa in silicon.

Figure 25 shows high-resolution luminescence spectra of Si:B with extremely low compensation ratio in the no-phonon spectral region. Weak BE luminescence lines of the compensating phosphorus impurity (BE(P)) are clearly resolved for these samples. Hence, the compensation ratio of these samples can be determined from the luminescence-intensity ratio of phosphorus BE to majority boron BE on the basis of the calibration relation of Eq. (4.20). The obtained values of the compensation ratio in Si:B used in this characterization study are presented in Table VI.

As is well known, the accurate dopant compensation ratio in a semiconductor can be determined only by a detailed analysis of the temperature dependence of free carrier concentration or mobility obtained from Hall-effect measurements by using parameter-fitting techniques[101]. However this method is very complicated and rather difficult for the high-purity crystals partially because of difficulty in obtaining good ohmic contacts to such samples at low temperatures around liquid helium temperature. On the contrary, the present photoluminescence method is essentially nondestructive (contactless) and highly sensitive to the small amount of compensating impurities. Therefore, this photoluminescence method of estimating directly the dopant compensation ratio from the BE-luminescence spectrum is considered to be very useful and simple compared with the conventional electrical measurements.

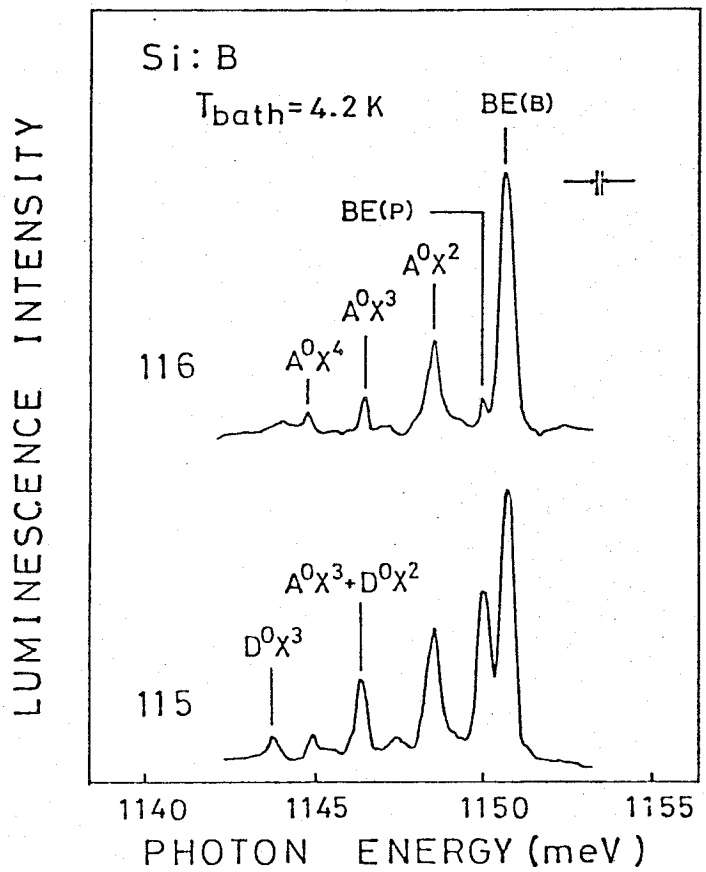

Fig. 25. Luminescence spectra in the no-phonon region of Si:B. Bound exciton luminescence (BE(P)) and the bound multi-exciton luminescence (D^0X^2 and D^0X^3) related to compensating phosphorus donors are clearly observed.

CHAPTER V

CHARACTERIZATION OF THERMALLY INDUCED DEFECTS IN SILICON

Oxygen and carbon, which are principal residual impurities in silicon crystals used for LSI technology, play a significant role for the formation of grow-in and IC-process induced crystal defects. Especially, various types of microdefects are introduced in silicon crystal during high-temperature heat treatments performed for many times in silicon-device processing[23,24]. These microdefects, which are generally detrimental to the device properties, are presently considered to be closely related to precipitation phenomena of excess oxygen impurity contained beyond the solid solubility in the case of Czochralski-grown (CZ) silicon crystals. Recent works by Kishino et al.[102-104] using transmission electron microscopy and infrared (IR) absorption methods on the heat treatment behaviors of thermally induced microdefects have also shown that carbon impurity participates in the formation of the microdefects and acts as a kind of nucleation center of oxygen precipitates. This suggests the existence of cooperative interaction between oxygen and carbon impurities in heat-treatment process of silicon ctsytals. However, little is known about the physical mechanism of the formation of these microdefects.

In the viewpoint of physics on impurity states in silicon, the elctronic structures of first-row impurities such as group-IV carbon and group-VI oxygen in silicon have remained so far unknown, compared with common group-III and V impurities having the shallow impurity levels in

silicon. As for the oxygen in silicon, it has been predicted by Pantelides [105] in his theoretical calculation of deep impurity levels concerned with these first row impurities, based on a pseudo impurity theory, that the electron binding energy of oxygen in silicon is about 3.0 eV and it can bind two (neutral oxygen state) or even three (negatively charged oxygen state) electrons.

On the other hand, in CZ-silicon crystals, it is well known that oxygen-related donors (OD) having rather shallow donor levels around 0.1 eV are induced by heat treatments in the temperature range between 300 and 500 °C[31,32]. Kaiser et al.[32] observed that the formation rate of OD depends on the fourth power of the interstitial oxygen concentration $[O_i]$ and the maximum concentration depends on the third power of $[O_i]$. These experimental observations led to the so-called SiO_4 model of OD. Indeed, this SiO_4 model explains well the reaction kinetics of OD. However, little is known for the formation mechanism of such shallow donor states from the isolated oxygen impurity having rather deep impurity levels as shown by Pantelides. Recently, some new experimental results have been reported and it has been pointed out that the electrical activity cannot be explained by the SiO_4 model, suggesting an association of lattice vacancies with the OD formation[106,107]. In the present work, we have studied in detail thermally induced defect states, especially the correlation with oxygen and carbon impurities, by photoluminescence, Hall-effect and IR absorption methods[28,30].

V-1. procedures of thermal annealing and Hall-effect measurements

Samples used in this annealing study were various kinds of commercial CZ and float-zone (FZ) silicon crystal doped with boron or phosphorus. The interstitial oxygen content $[O_i]$ and the substitutional carbon content $[C_s]$ involved in the samples were determined from the IR absorption method using the well known calibration relations; $[O_i] = 2.73\times10^{17}\alpha_{max}$ cm^{-3} and $[C_s] = 1.10\times10^{17}\alpha_{max}$ cm^{-3}, where α_{max} is the maximum absorption coefficient of the absorption line at 9 μm for oxygen[108] and 16.5 μm for carbon[109]. These values of $[O_i]$ and $[C_s]$ are listed in Table VII. Heat treatment for the samples was carried out at temperatures ranging from 430 and 600 °C in Ar ambient.

Hall-effect measurements have been made by using the conventional van-der Pauw method [110] under the magnetic field with the strength of 10^4 Gauss. The values of free-carrier concentration n were calculated by using the well-known relation given by $n = 1/R_h q$, where R_h and q are Hall coefficient and electron charge, respectively. Therefore, the present data of n estimated by the above-mentioned formula generally include small errors introduced by the neglection of scattering factor.

V-2. Hall-effect analysis of thermally induced oxygen donors

Hall-effect measurements have been precisely made for CZ-Si:B samples. The typical results are shown in Fig. 26. Figure 26 shows plots of resistivity (a) and thermally induced donor density (b) as a function of annealing period at 450 and 500 °C. As is shown in this figure, the conduction type of the sample CZ-Si:B is converted from p to n-type conduction within a few hours. Commercially available silicon crystals are, in general, subjected to heat treatment around 650 °C before shipping

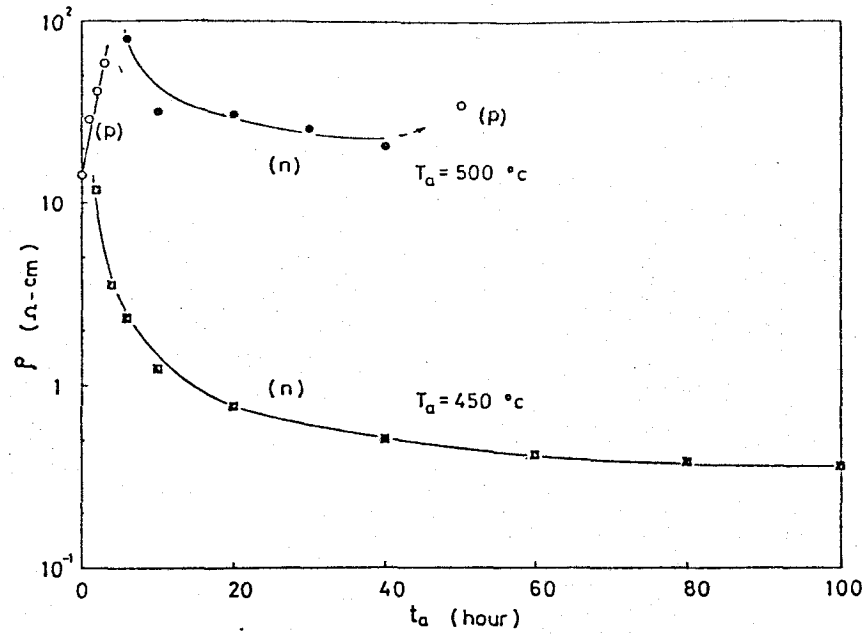

(a)

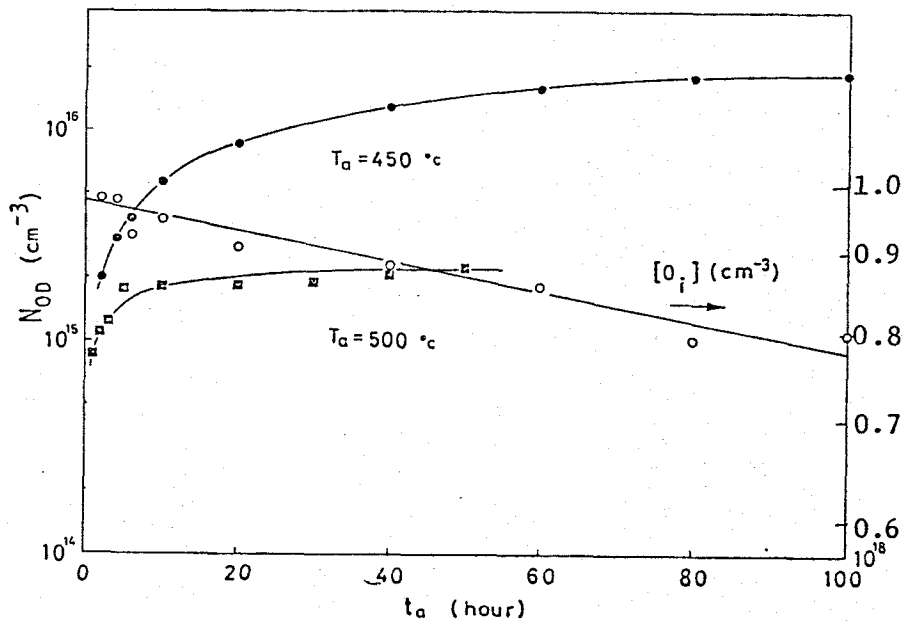

(b)

Fig. 26. Plots of resistivity ρ as a function of annealing time at 450 °C and 500 °C (a). Figure (b) shows plots of thermally-induced oxygen donor density and interstitial oxygen content as a function of annealing time.

of silicon crystals so as to eliminate thermally induced donors generated during the crystal growth process. However, as can be seen in this figure, a large amount of donors are reproduced by subsequent heat treatments even in silicon crystals already subjected to such a donor-elimination process, which is one of the serious problems in silicon crystal growth technology.

The difference in the generation rate of thermally induced donors, here we call OD, between 450 °C annealing and 500 °C annealing shows the existence of a chemical reaction in the crystal, and actually the formation and migration energy involved in the reaction have been obtained by the analysis of these plots[32]. The density of interstitial oxygen impurity obtained by IR measurements for these annealed samples as a function of the annealing period is also presented in Fig. 26(b). The interstitial oxygen content decreases with incresing annealing period, the result suggesting that supersaturated oxygen impurities precipitate even at low temperatures employed here. Hence, it is straightforward to consider on the basis of above-mentioned results that oxygen precipitation phenomenon is closely related to the formation of thermally induced donors (OD) generated at such low temperatures.

Figure 27 shows the temperature dependence of the electron density obtained by Hall-effect measurements for CZ-Si:B crystals type-converted by heat treatment at 430 °C. As can be seen in the figure, several carrier-saturations are observed for each sample. For samples annealed for short periods less than 20 h, at least four distinct donor levels, which are described here as ODj (j=1,2,...) in order from the shallowest donor level OD1. When the annealing time t_a is longer than 40 h, the third and fourth saturations around 300 K come to converge. Earlier

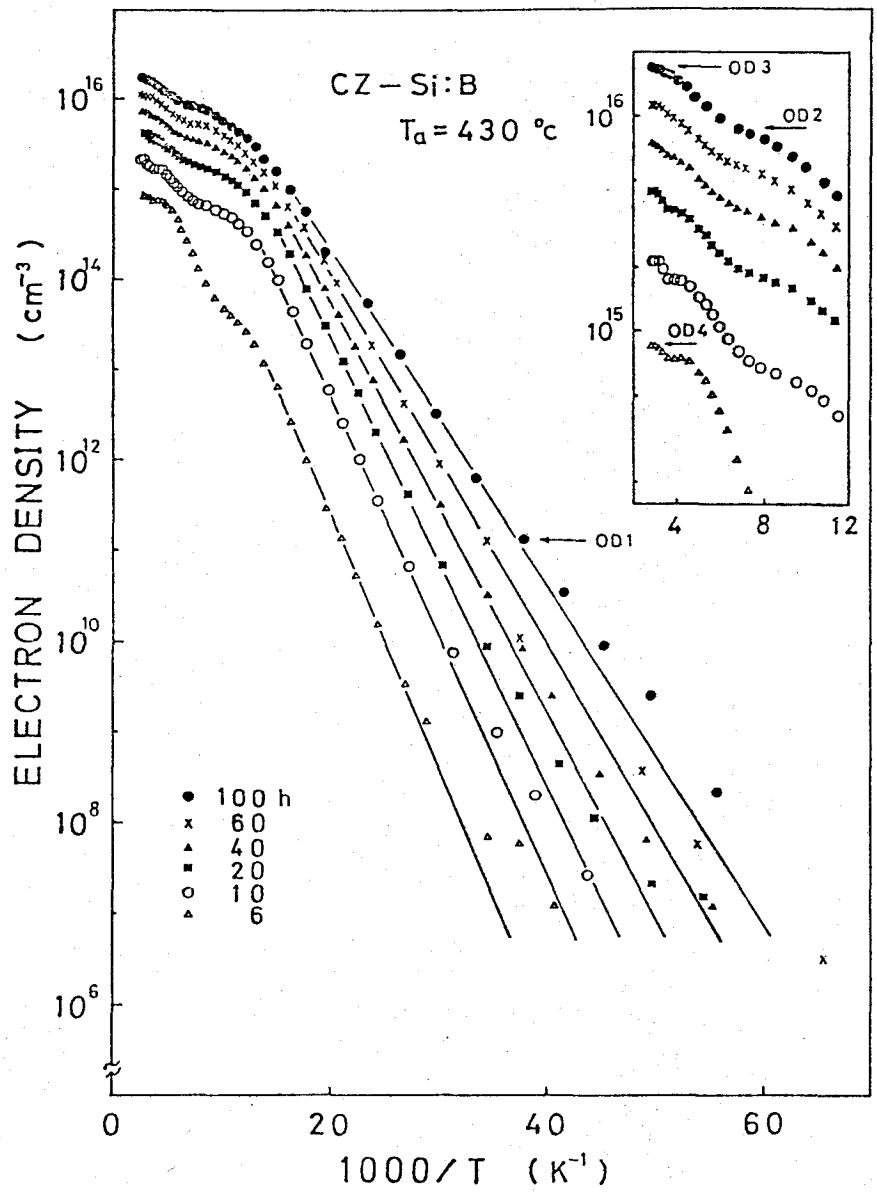

Fig. 27 Temperature dependence of the electron density of CZ-silicon crystal type-converted by heat treatment at 430°C for several periods of heat treatment.

work revealed the existence of two donor states induced by heat treatment at about 450 °C in CZ-silicon crystals[107,111]. We think that some of the donor levels were obscured in earlier data, as observed in the data of Fig. 27. The ionization energies and densities of OD were obtained from the analysis of the data of Fig. 27, using the method recently proposed by Partain et al.[112] This method is very powerful for analyzing Hall-effect data of a sample containing several species of donor or acceptor, compared with the conventional method. In the analysis, the degeneracy of all the OD states are assumed to be 2.

The shallowest donor OD1 shows the ionization energy of 25-40 meV, which is shallower than usual group-III and V impurities in silicon. The density of OD1 is around 1.20×10^{15} cm^{-3} for all the samples and the change with t_a is small. For the donor states ODj (j=2,3, and 4) the variation of the ionization energies as a function of the corresponding donor density is shown in Fig. 28. The ionization energies of OD decrease with increasing the donor density for all the donor states. Especially, the ionization energy of OD2 varies approximately as $\Delta E_{OD2} \sim [N_{OD2}]^{-0.14}$. This result is similar to the decrease in ionization energy of group-III or V impurities in silicon and germanium, which was observed near the so-called intermediate-doping region[5,113]. These behaviors were explained as due to an inter-impurity interaction caused by the formation of impurity complexes. Such similarity suggests the presence of oxygen complexes which would form electrically active shallow impurity levels. It should be noted that the energy-level spacings and densities of OD2 and OD4 for all the samples annealed for longer periods than 40 h show characteristic features of those in a divalent donor in silicon. The divalent nature of OD has recently been

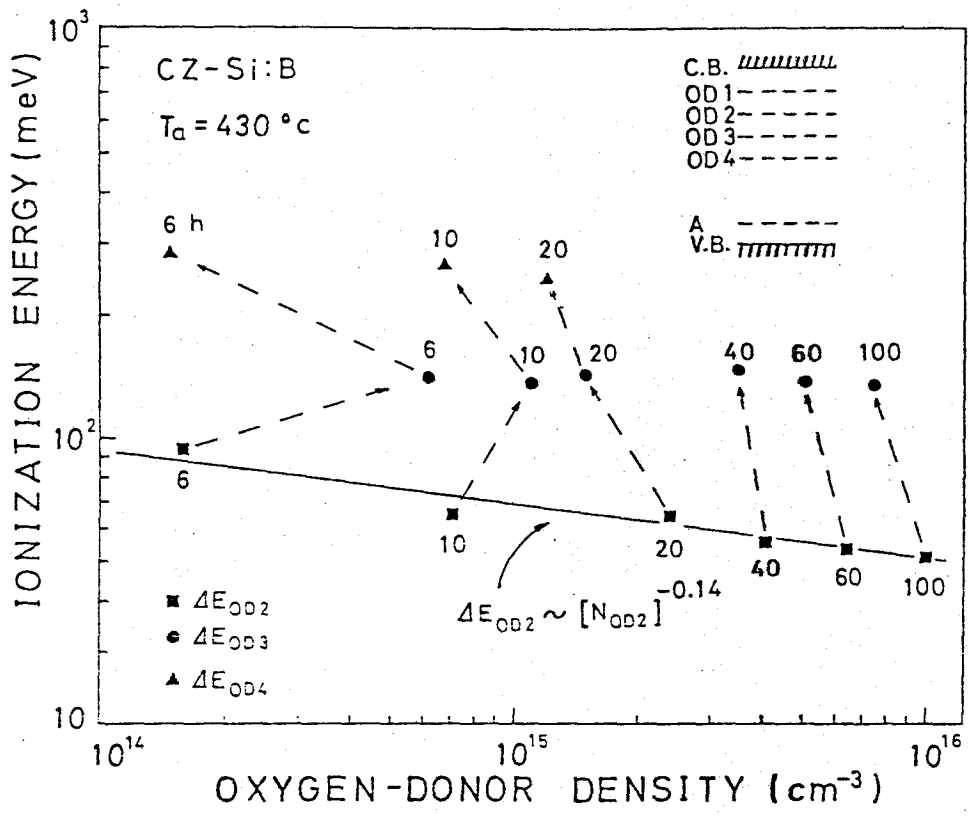

Fig. 28 Plots of the ionization energy of ODj(j=2,3 and 4) as a function of the corresponding donor density obtained from Hall-effect analysis. Data points from samples subjected to the same period annealing are combined by the dashed arrows.

observed by IR measurements for 450 °C annealed CZ-silicon[114]. We have also observed the relations of $\Delta E_{OD3} \sim 2.6 \times \Delta E_{OD2}$ and $N_{OD3} \sim 0.75 \times N_{OD2}$.

V-3. photoluminescence observation of oxygen donor states

Figure 29 shows a low-temperature photoluminescence spectrum for the CZ-silicon sample annealed at 430 °C for 100 h. The luminescence spectrum of the sample before annealing is also shown for comparison. The intensity in both the luminescence spectra is normalized at the BE luminescence lines. In the spectrum of as-received wafer, FE luminescence lines (FE_q, where q denotes a momentum-conserving phonon involved in the transition), boron-related BE lines ($BE_q(B)$) and their BMEC lines ($A^0X_q^m$, m=2,3,..) are clearly observed. Upon heat treatment, new broad luminescence bands described as O_q come to appear in the low-energy sides of the BE and BMEC luminescence lines. Similar luminescence bands have recently been observed for CZ-silicon crystal heat treated at 450 °C for 64 h, which has been assigned as due to OD[116]. We have found in this work some new features of those O_q luminescence bands. As can be seen in Fig. 29, the O_q luminescence bands accompany several additional luminescence lines denoted by arrows a, b and c in the TO-phonon region, which locate at 1086.7, 1085.6 and 1084.3 meV, respectively. These structures are also observed for the O_{TA} luminescence band, whereas they are not clearly resolved in the O_{NP} band.

It has been found that the O_q bands still remain without large intensity reduction when temperature increases from 4.2 K to 15 K, while BE and BMEC luminescence lines nearly disappear. This fact shows that

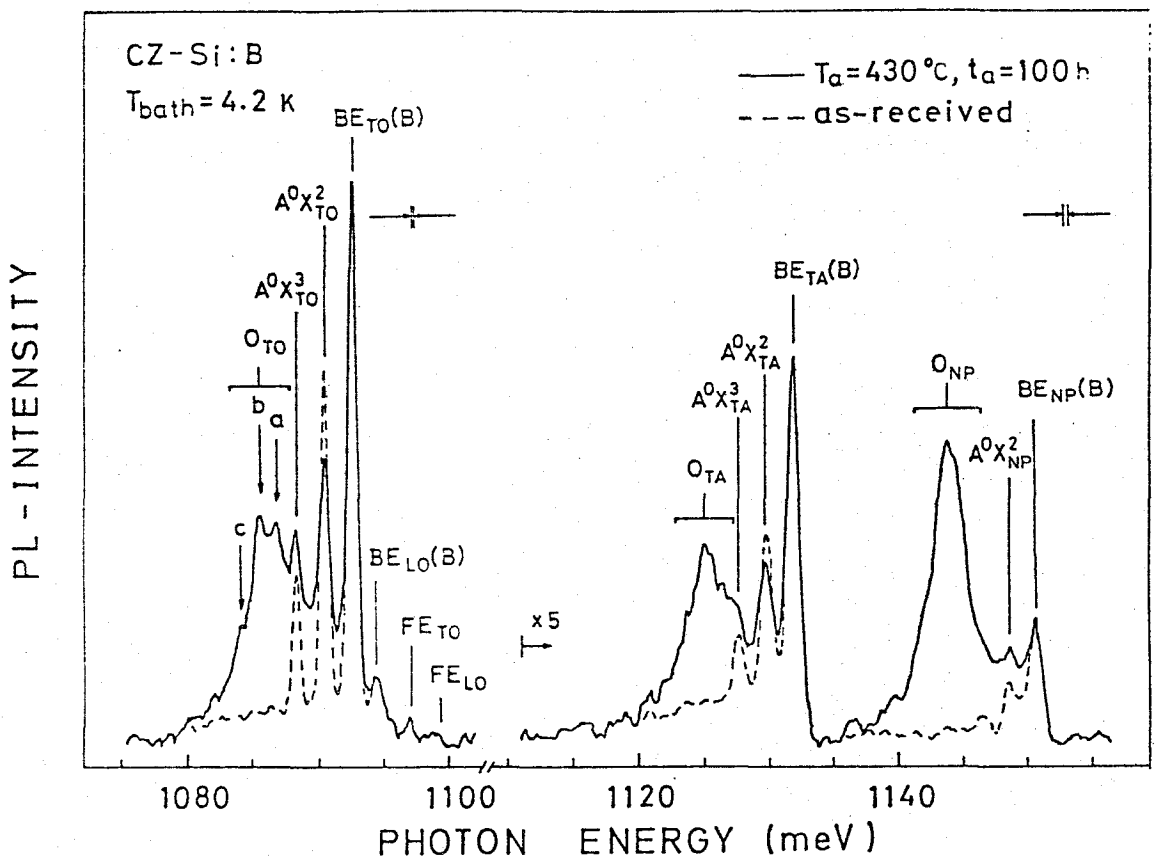

Fig. 29 Low-temperature luminescence spectrum of CZ-Si:B heat-treated at 430°C for 100h. Luminescence spectrum of the sample before annealing (as-received wafer) is also shown for comparison.

the O_q luminescence bands are due to radiative recombination of localized excitons whose localization energy is greater than that of the boron BE. The localization energy is spectroscopically estimated to be 10.6 meV from the energy shifts of the O_q bands from the corresponding FE thresh olds. This value is about two times larger than those of BE associated with common group-III and V impurities in silicon[48]. The intensity ratio of the O_{NP} band to the O_{TA} band in the spectrum of Fig. 29 is about 1.5, which is rather small compared with group-III and V impurities in silicon, considering that the localization energy obtained for the O_q bands is about two-times larger than those of group-III and V impurities. For example, the corresponding intensity ratio is 16 for the BE luminescence associated with an arsenic donor whose exciton-localization energy is 5.4 meV[48]. Such behavior seems to be characteristic of the luminescence from excitons localized at an impurity complex formed in heavily doped silicon[75-79].

Figure 30 shows the annealing time dependence of exciton luminescence spectra in the TA- and no-phonon regions for annealed CZ-Si:B samples. Heat treatment causes the decrease in BE and BMEC luminescence intensities, inducing new broad O_q luminescence bands. The O_q bands grow larger with increasing annealing time. The peak-energy positions of the O_q luminescence bands shift slightly with increase of annealing time.

To compare Hall-effect data with photoluminescence data related to OD, we plot in Fig. 31 the annealing time dependences of OD densities obtained from the analysis of Hall-effect data and the luminescence intensities of O_{NP} band normalized by that of the $BE_{NP}(B)$ line. The densities of OD2 and OD3, and the sum $\sum N_{ODj}$ increase rapidly by initial

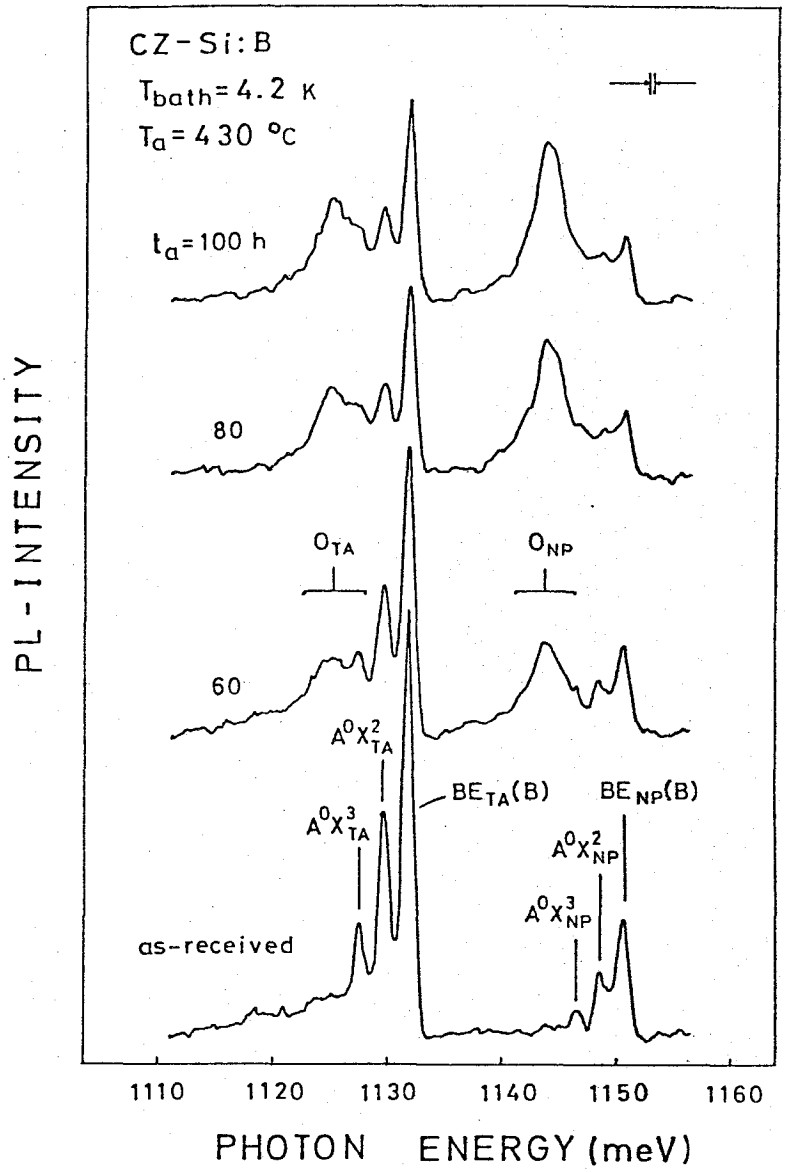

Fig. 30 Annealing-time dependence of exciton luminescence spectra in the TA- and no-phonon spectral regions.

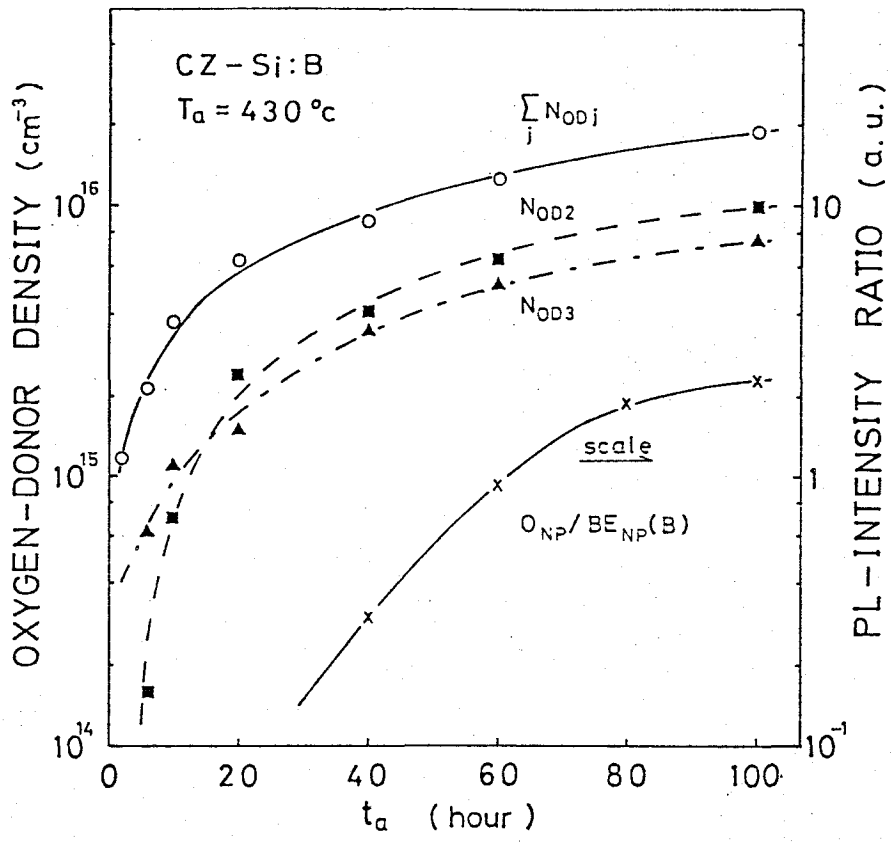

Fig. 31 Annealing time dependence of Oxygen-donor densities obtained from Hall-effect analysis. Plots of the intensity of O_{NP}-luminescence band relative to that of $BE_{NP}(B)$-luminescence line are also presented.

annealing, t_a < 20 h, and in the long-time annealing they gradually increase and saturate. As can be seen in the figure, the intensity of the O_{NP} luminescence band increases with increase of annealing time, similarly to the behavior of the density of OD. However, the density of OD1 does not show such an annealing-time dependence as of OD2 and OD3, and also OD4 states disappear in long-time annealing where the O_q luminescence bands come to appear. Therefore, we conclude that OD2 and OD3, which show characteristic behaviors similar to divalent donors in silicon, are closely related to the O_q luminescence bands.

V-4. thermally induced luminescent centers

In this section we present a luminescence characterization study for thermally induced defects related to carbon and/or oxygen impurities in silicon crystals annealed at relatively low temperatures around 500 °C. Defects generated at these low temperatures, which are considered to be an embryo of microdefects induced by high-temperature annealing around 1000 °C, cannot be observed by the conventional methods such as electron microscopy and optical microscopy combining a chemical etching, but they are observed by luminescence spectroscopy[30,116].

Figure 32 shows the exciton luminescence of four kinds of phosphorus-doped silicon crystals annealed at 500 °C for 100 hours. Clear difference in the spectra among the samples can be seen in the figure. The sample FZ-3 with low oxygen and carbon contents indicates the FE and BE luminescence lines related to dopant phosphorus. Their BMEC lines are also observed. The spectral shape and the intensity are same as

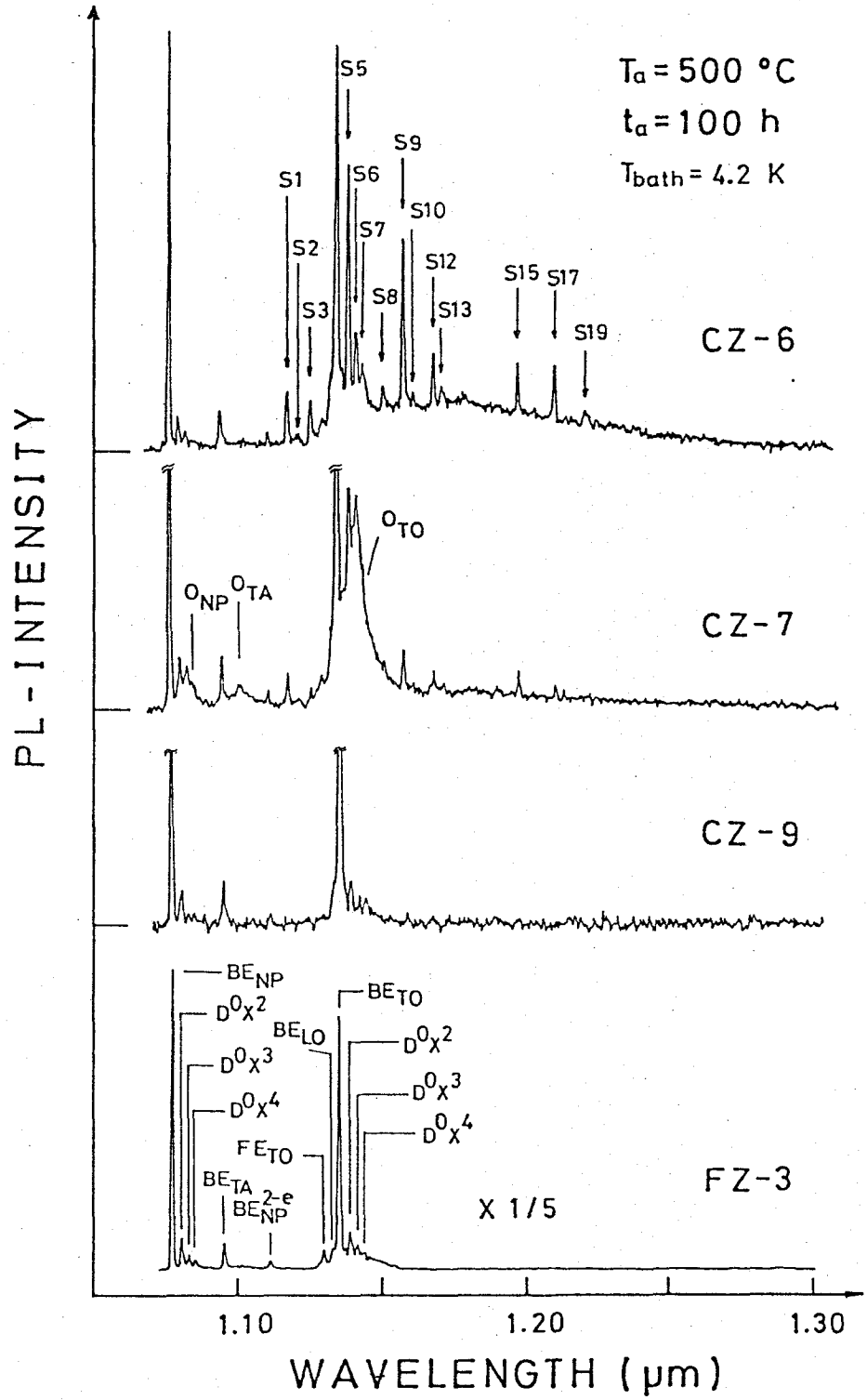

Fig. 32 Exciton luminescence spectra of four kinds of silicon crystals annealed at 500°C for 100h. Peak-energy positions of Sj lines observed at 4.2K are indicated by arrows in the spectrum of CZ-6. In addition to the lines shown here, luminescence lines S4, S11, S14, S16 and S18 come to appear at higher temperatures around 10K.

those of FZ-silicon crystal before annealing. The luminescence spectrum of CZ-9 containing a very high carbon content and a moderate oxygen content is essentially same as that of FZ-3 except for the large luminescence intensity reduction. The reduction in luminescence intensity suggests the introduction of nonradiatve recombination centers by heat treatment at 500 °C. The sample CZ-7 having a high oxygen content and a low carbon content shows broad luminescence bands in the low-energy sides of phosphorus BE luminescence lines. As was shown in the previous section these broad luminescence bands well correlate with thermally induced oxygen donors. In addition to the O_q bands the luminescence spectrum of CZ-7 contains several sharp luminescence lines, described hereafter as Sj-lines, are more strongly observed for the sample CZ-6 containing high oxygen and carbon contents. We can also find the increase of background luminescence component from 1.15 to 1.25 μm. In the luminescence spectrum of CZ-6, there exist at least nineteen new luminescence lines as indicated in the figure as Sj (j=1,2,...), whose peak-energy positions and/or temperature dependence are quite different from those of the usual BE and BMEC luminescence lines associated with group-III or V impurities.

To analyze the densities of luminescent centers related to the O_q luminescence bands or Sj lines observed for annealed silicon crystals, we consider the intensity ratio of these thermally induced luminescence lines relative to the dopant BE luminescence lines. Then, we have to take into account the difference in the values of recombination parameters between boron-and phosphorus-related BE as well as the difference in the dopant concentrations. Using the recombination parameters obtained in the present work, which are shown in Tables II-V, we define

provisional densities of the luminescent centers for O_q bands, $\tilde{N}_{ox}$, and for Sj lines, $\tilde{N}_{Sj}$. These values are given by

$$\tilde{N}_{ox} = \gamma_q N_I [\ I(O_{TA})/I(BE_q)\ ] \quad , \tag{5.1}$$

$$\tilde{N}_{Sj} = \gamma_q N_I [\ I(Sj)/I(BE_q)\ ] \quad , \tag{5.2}$$

where the factor γ_q is a correction factor taking into account the difference in recombination parameters. The γ_{TA} value for phosphorus-doped silicon and γ_{NP} value for boron-doped silicon were estimated to be 2.46 and 1.03, respectively.[117] N_I is the dopant impurity content. "I" denotes the luminescence intensity of the indicated luminescence componet. It is considered that $\tilde{N}_{ox}$ and $\tilde{N}_{Sj}$ are approximately proportional to the real densities of the corresponding luminescent centers. The obtained values of $\tilde{N}_{ox}$ and $\tilde{N}_{S9}$ of the samples annealed at 500 °C for 100 h are presented in Table VII. From the data shown in Table VII, we have obtained the following results. (a) The density $\tilde{N}_{ox}$ is high for silicon crystals having a high content of oxygen and strongly reduced for carbon-rich samples. This is consistent with results of IR and electrical measurements by Bean and Newman, showing that the presence of a high content of carbon strongly inhibits the formation of thermally induced oxygen donors. (b) The density $\tilde{N}_{S9}$ is high for samples having a high content of carbon and increased by the presence of a high content of oxygen.

V-5. sharp luminescence lines of carbon-rich CZ-silicon

Table. VII Dopant impurity, resistivity ρ, interstitial-oxygen content $[O_i]$ and substitutional carbon content $[C_s]$ of the samples before annealing . Experimental values of $\tilde{N}_{ox}$ and $\tilde{N}_{sj}$ of the S9 line for the samples annealed at 500°C for 100h are also shown.

sample	dopant	ρ (Ωcm)	$[O_i]$ ($10^{17}cm^{-3}$)	$[C_s]$ ($10^{16}cm^{-3}$)	$\tilde{N}_{ox}$ ($10^{14}cm^{-3}$)	$\tilde{N}_{Sj}$ ($10^{14}cm^{-3}$)
CZ-1	B	4.5	10.3	≤ 1	30.8	-
CZ-2	B	4.5	7.4	≤ 1	25.5	-
CZ-3	B	20.0	9.8	≤ 1	13.2	-
CZ-6	P	4.5	9.6	10.2	≤ 5.6	111.0
CZ-7	P	5.3	9.0	≤ 1	9.4	13.4
CZ-9	P	2.9	5.8	42.8	-	-
CZ-10	B	26.6	7.5	10.6	≤ 1.0	6.2
CZ-11	B	5.7	7.2	8.2	≤ 4.2	3.7
CZ-12	P	4.5	8.4	4.6	≤ 5.5	4.3
FZ-2	B	19.0	≤ 1	≤ 1	-	-
FZ-3	P	9.5	≤ 1	≤ 1	-	-

In this section, the properties and the origin of sharp luminescence lines observed for annealed carbon-rich CZ-silicon are studied in detail. Figure 33 shows the low-temperature luminescence spectra of CZ-6 sample isochronally annealed for 100 h at several annealing temperatures. As can be seen in the figure, Sj lines are most strongly observed in the sample annealed at 500 °C. The S1 and S3 luminescence lines remain strongly also in the sample of 550 °C annealing, showing that the origin of S1 and S3 lines is different from other Sj lines. The peak-energy position of S1 line is very close to the R line observed previously by Michard et al. for indium-doped CZ silicon[118]. It should be also noted that the intensities of the lines S5, S6 and S7 located at the low-energy side of the BE_{TO} line, whose energy positions are very close to those of phosphorus-related BMEC lines, increase with heat treatment at 500 and 550 °C compared with the intensities of the BMEC lines for the sample before annealing. Therefore, it seems that these Sj lines are superposed on the BMEC lines.

Luminescence spectra related to Sj lines have been measured at temperatures ranging from 4.2 to 50 K. The typical data of the temperature behaviors of Sj lines are presented in Fig. 34. As can be seen in this figure, the luminescence intensities of Sj lines initially increase with increasing the sample temperature from 4.2 K and subsequently are quenched at higher temperatures, while phosphorus-BE luminescence lines monotonously decrease with increasing temperature. Most Sj lines disapper around 50 K. The temperature T_{max} at which the intensities of Sj lines become maximum is shown in Table VIII. From an analysis of the temperature behaviors shown in Fig. 34 we have obtained the thermal-activation energies (ΔE_1) and the quenching-activation

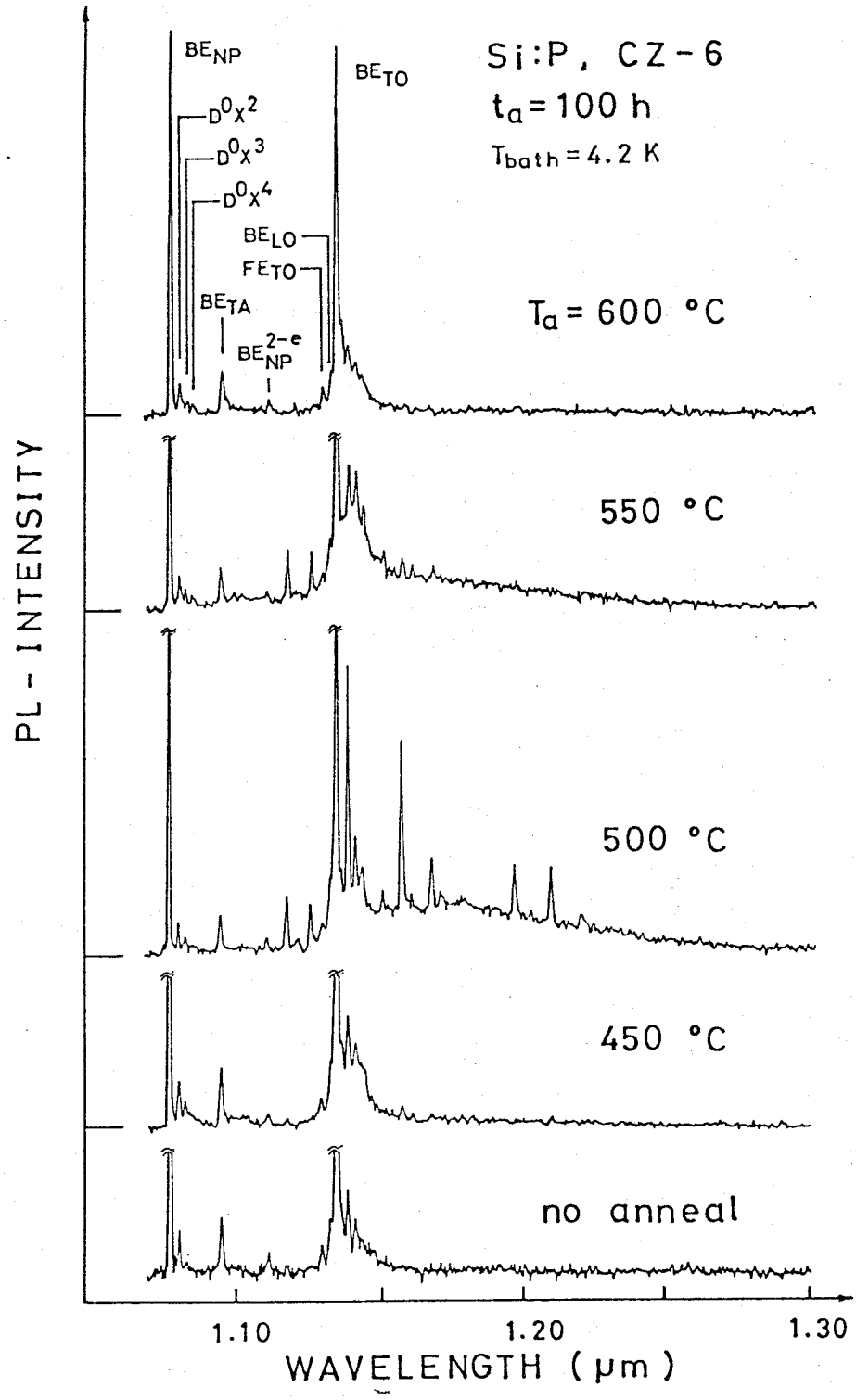

Fig. 33 Photoluminescence spectra of CZ-6 sample isochronally annealed for 100h. at several annealing temperatures.

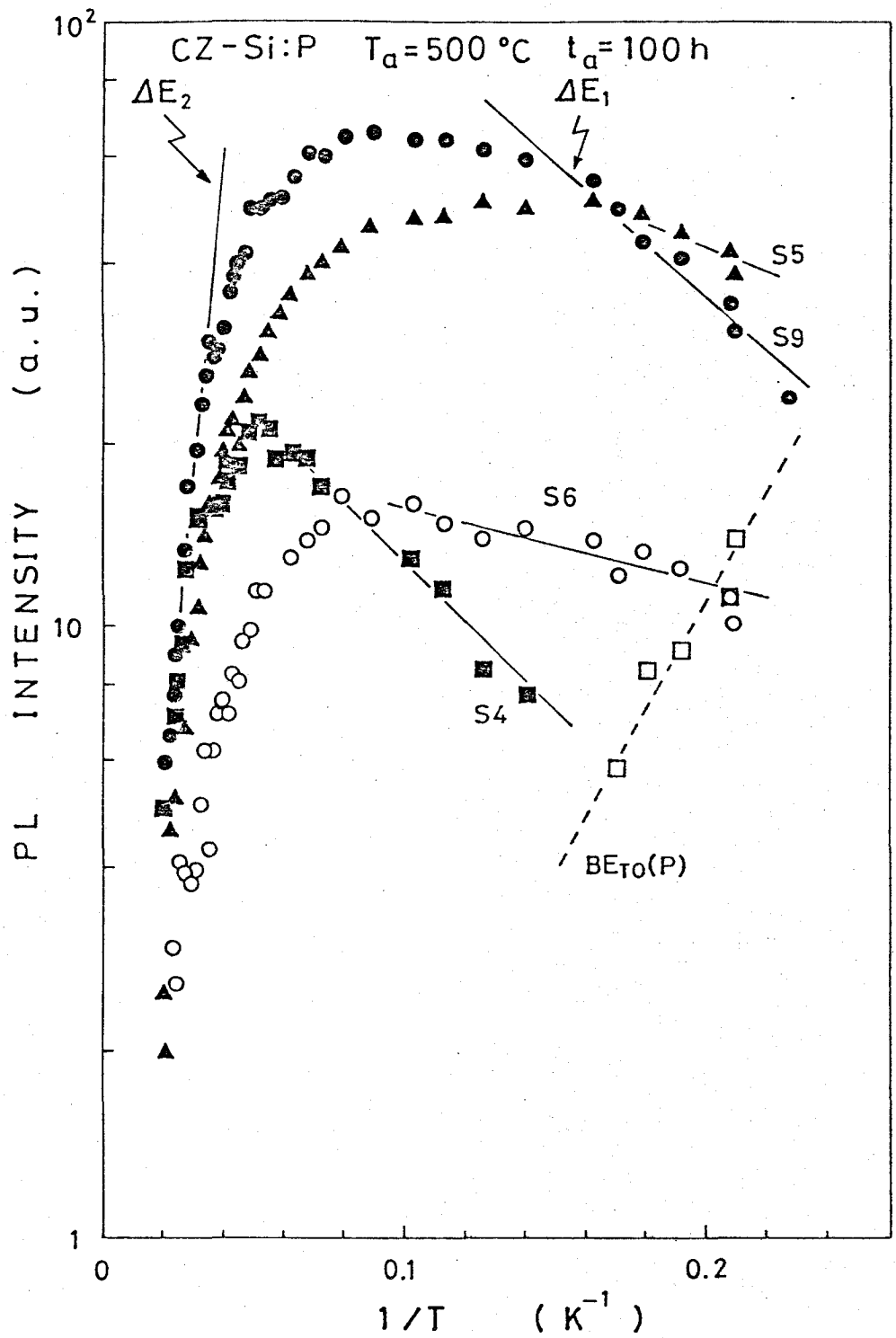

Fig. 34 Temperature dependence of luminescence intensity due to Sj lines observed in annealed carbon-rich CZ-silicon.

Table. VIII Properties of Sj-luminescence line observed for carbon-rich CZ-silicon.

line	$\hbar\omega$ (meV)	E_{bx} (meV)	T_{max} (K)	ΔE_1 (meV)	ΔE_2 (meV)
S1	1108.4	46.1	7		
S2	1104.7	49.8	∿15		
S3	1100.5	54.0	8		
S4	1091.2	63.3	19	1.06	10.50
S5	1088.1	66.4	7	0.44	11.69
S6	1085.5	69.0	10	0.39	4.79
S7	1083.3	71.2	6		
S8	1075.5	79.0	18		
S9	1070.5	84.0	11	0.94	8.08
S10	1067.3	87.2	——		
S11	1064.4	90.1	18	1.39	——
S12	1060.6	93.9	7	1.05	4.70
S13	1058.4	96.1	11	1.69	4.48
S14	1037.5	117.0	25		
S15	1034.2	120.3	8		
S16	1029.5	125.0	25		
S17	1023.3	131.2	9		
S18	1017.9	136.6	11		
S19	1014.5	140.0	7		

energies (ΔE_2) for Sj lines. The quenching-activation energies are ranging from 5 to 12 meV and are much smaller than the exciton-binding energy (E_{bx}) of these lines obtained spectroscopically by assuming that all of the Sj lines are due to no-phonon recombination of localized excitons. The exciton-binding energies are distributed in the range of 46-140 meV. Detailed data of transition energies, E_{bx}, T_{max}, ΔE_1 and ΔE_2 are presented in Table VIII.

It should be noted here that these temperature behaviors are characteristic of localized excitons bound to an isoelectronic trap in semiconductors[119]. That is, the fact that luminescence intensity of the Sj lines initially increase with increasing sample temperature from 4.2 to 10-20 K suggests the existence of a thermal activation process from a dipole-forbidden ground state of the localized excitons to the dipole-allowed excited state which is the origin of Sj line. The possibility of the presence of such a dipole-forbidden localized exciton state comes from a total angular momentum J=2 state composed from a j-j coupling of a j=1/2 electron and a j=3/2 hole localized at the isoelectronic center[120]. Secondly, the fact that the quenching activation energy is smaller than the spectroscopically obtained exciton-binding energy also suggests that a weakly trapped carrier, probably hole since the isoelectronic carbon impurity possesses larger electron negativity than the host silicon, is initially released by the small dissociation energy from the localized exciton complex through the thermal-quenching process presented in Fig. 34. Another tightly trapped carrier, probably electron, is left behind at the isoelectronic center. Therefore the latter fact is well consistent with the exciton-binding mechanism of an iselectronic trap, where a hole (electron) is captured weakly by a Coulombic attractive

potential around the negatively (positively) charged pseudo-acceptor (donor) center composed of a tightly bound electron (hole) at the center through the characteristic short-range potential[121-123].

These isoelectronic-trap like states observed here might be originated from impurity complexes, consisting of carbon and oxygen, formed during heat treatment around 500 °C. The existence of such kinds of carbon-oxygen complexes formed by annealing at low temperatures has been already identified in IR absorption spectra by Bean and Newman[124].

Based on the results of a thermal quenching study on the Sj lines observed for carbon-rich silicon, we show the energy diagram and the transition scheme for S9 line, which is one of the strongest Sj line observed, assuming that the S9 line is originated from excitons bound to an isoelectronic electron trap, in Fig. 35. In this figure, I^0X_g and I^0X_e are the ground (forbidden) state and the excited (allowed) BE state, respectively. I^0 denotes the isoelectronic trap center. I^0e indicates the pseudo-acceptor state composed of a highly localized electron and a I^0 center. From this picture, we can easily estimate the electron dissociation (binding) energy E_{be} of the I^0e complex concerned with the S9 line, which is estimated to be 90.6 meV. This value is given by the relation; $E_{be} = E_{bx} + E_x - \Delta E_2$. The value of E_{be} is about two times larger than those of common group-V donors in silicon.

V-6. evidence for an isoelectronic luminescence center in silicon

Luminescence from an isoelectronic center in silicon has recently been reported by Weber et al.[125,126] in FZ-silicon crystals having high

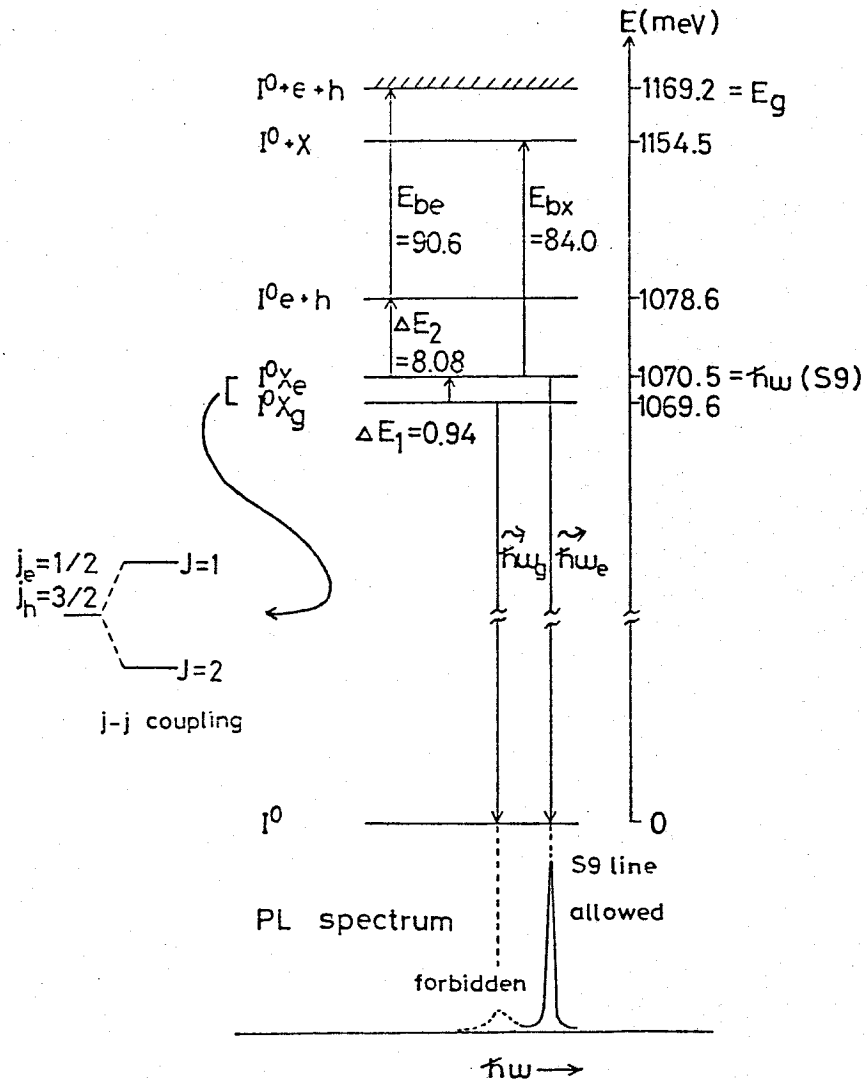

Fig. 35 Schematic representation of energy level diagram and transition scheme concerned with S9 luminescemce line.

carbon and low oxygen contents, with one exception of the weak luminescence from antimony-doped CZ silicon. Their Zeeman measurements showed that the isoelectronic trap has the axial symmetry in the (111) crystalographic axis, suggesting the association of at least two constituents located along the (111) axis. They also considered that one of the constituents is probably carbon impurity.

Another observation of such an isoelectronic trap by luminescence measurements has been reported by Michard et al.[118] in indium-doped CZ-silicon. They considered that the isoelectronic trap involves indium impurity and also may involve carbon or oxygen as an additional partner. In both cases, the observed isoelectronic center is not an isolated impurity such as the substitutional carbon, but rather it is an impurity complex probably consisting of carbon and other impurity such as indium or oxygen.

We have been trying to observe luminescence lines associated with the isoelectronic center for several kinds of as-grown crystals having the high carbon content. However, we have not been able to observe such luminescence lines as reported by the above-mentioned authors for as-grown crystals. In the present work, we have succeeded in finding strong luminescence lines, which are probably related to isoelectronic traps in silicon, for annealed CZ-silicon crystals with high contents of oxygen and carbon. This result suggests that the thermal history of silicon crystal during the crystal growth or thermal annealing process plays an important role for the formation of isoelectronic traps. Namely, we consider that an impurity complex consisting of carbon and other chemical impurity such as oxygen formed by the chemical reaction during the heat-treatment process can act effectively as an

isoelectronic trap. Therefore, as-grown crystals, even if they contain the high content of carbon, do not always show luminescence lines associated with isoelectronic traps. This problem is still open for future investigations.

CHAPTER VI

CONCLUSIONS

The conclusions obtained by this thesis work on the exciton luminescence of impurities and thermally induced defects are summarized as follows:

(1) We have systematically studied excitation-level and impurity-concentration dependence of the exciton luminescence for phosphorus-, boron- and lithium-doped crystalline silicon, with particular emphasis on the BMEC luminescence related to these impurity species. In the low impurity concentration range below 10^{16} cm^{-3}, sharp luminescence lines of FE, BE and BMEC dominate over the exciton luminescence spectra of silicon, and their impurity-content and excitation behaviors have been interpreted by the formation and decay kinetics of the FE, BE and BMEC system. On the other hand, at high doping levels beyond 10^{17} cm^{-3}, such sharp luminescence lines associated with isolated shallow impurities come to disappear, and instead anomalously broad luminescence bands appear in the low-energy side of the principal BE luminescence lines. The peak-energy position of the broad luminescence bands shift toward the low-energy side with increasing impurity concentration. It has been also found from the temperature dependence measurements that the broad luminescence bands shift toward the high-energy side and the principal BE luminescence lines come to appear as temperature increases. These impurity-content and temperature behaviors led to the conclusion that such broad luminescence bands are originated from radiative

recombination of excitons localized at impurity complexes formed by the inclusion of a large amount of dopant impurities near the so-called intermediate-doping range. These broad luminescence bands have been observed for highly doped silicon with several species of donor (phosphorus, antimony, arsenic and lithium) and acceptor (boron and aluminum)

(2) Dynamical processes of BMEC have been investigated in detail for the first time, with particular emphasis on the exciton-capture and Auger-recombination processes. In the exciton-capture process of BMEC, several modes of processes appear, reflecting the existence of the shell structure characteristic of BMEC. Two types of exciton-capture processes have been considered. First, an exciton is captured into the inner ground shells of electron and hole leaving the resultant BMEC in the ground state. Second, an exciton is captured into the excited shells leaving BMEC in the excited states and the resultant BMEC subsequently relaxes to the ground state. As for the decay process, the Auger-recombination process has been considered to be the dominant recombination channel of BMEC at low temperatures around liquid helium temperature. This is due to the fact that BMEC possesses many electrons and holes localized around an impurity center at the high local density and this makes the Auger-recombination process quite probable, which is essentially nonradiative recombination accompanied by an inter-band carrier scattering induced by carrier-carrier Coulomb interaction. In the Auger-recombination process of BMEC, an electron-hole pair localized in BMEC recombines with exciting a second bound carrier into the conduction or valence band, leaving a charged and unstable complex having the residual carrier. This charged and unstable state relaxes rapidly,

releasing the residual carrier. Hence, a two-orders lower complex is formed by the Auger-recombination process of BMEC.

(3) Based on considerations on the exciton-capture and Auger-recombination processes of BMEC, coupled rate equations in the FE, BE and BMEC system have been proposed. Using the rate equations, we have derived a theoretical formula of the BMEC luminescence intensity as a function of excitation intensity and impurity concentration. From a simple analysis of the excitation-level and impurity-content dependence data of the BE and BMEC luminescence by using the theoretical formula, we have determined for the first time the exciton-capture and Auger-recombination rates of BE and BMEC for Si:P, Si:B and Si:Li. It has been found that the obtained values of exciton-capture and Auger-recombination rates, especially their dependences on the order of BMEC, are closely related to the shell structure of these impurity species.

(4) The exciton-capture rate (cross section) on a neutral impurity center in silicon has been formulated. In the formulation, the exciton LA-phonon interaction is taken into account on the basis of the deformation potential approximation. The calculated results show that the exciton-capture cross section decreases with increasing temperature, which is consistent with the experimental observation.

(5) We have investigated photoluminescence characterization methods to estimate a small amount of impurity contents and the compensation ratio in high-purity silicon as an application of results obtained from the study on the recombination kinetics of the FE, BE and BMEC system.

As a result, we have succeeded in developing a new method to characterize a small amount of impurities and the compensation ratio. This method is based on theoretical considerations on the excitation-level and dopant-content dependence of the luminescence intensity ratio of BE to FE. Using the values of the exciton-capture rate at a neutral impurity and the Auger-recombination rate of BE, the dopant content in the sample can be directly determined in this characterization method from the observed luminescence-intensity ratio of BE to FE. We have also developed a photoluminescence method to characterize the dopant compensation ratio of the sample from a simple analysis of the BE-luminescence intensity ratio of compensating impurity to majority dopant impurity. These photoluminescence characterization mehtods are essentially nondestructive and highly sensitive to a small amount of dopant and compensating impurities.

(6) We have also performed a photoluminescence characterization study for thermally induced defects in silicon single crystals used in LSI technology. In this study, so-called thermally induced oxygen donors generated by low-temperature annealing around 400-500 °C have been investigated in detail by the photoluminescence technique combining IR absorption and Hall-effect measurements. We have observed a characteristic change in the ionization energy of the oxygen donors with annealing period, this suggesting the formation of several species of oxygen clusters distributed in the crystals. Photoluminescence spectra related to these oxygen donors reveal some new features characteristic of the luminescence from excitons localized at such oxygen clusters.

(7) In the annealing study for various kinds of silicon crystals having several different oxygen and carbon contents, we have found many sharp luminescence lines for the first time, whose transition energies and temperature behaviors are quite different from those of the usual BE, for carbon-rich CZ silicon annealed around 500 °C. Temperature and annealing effects on these sharp luminescence lines have been measured in detail, the results showing that the sharp luminescence lines are due to the recombination of an exciton localized at an isoelectronic center possibly composed of carbon and oxygen.

Appendix. Derivation of Eq. (3.7)

Using Eqs. (3.3) and (3.4), the full description of the rate equations is given by

$$\left.\begin{aligned}
0 &= \frac{\partial n_m}{\partial t} = C_{m-1}\, N\, n_{m-1} - C_m\, N\, n_m + W_{m+2}\, n_{m+2} - W_m\, n_m \\
&\qquad\qquad\qquad\qquad\qquad\qquad\qquad\qquad \text{for } 1 \le m \le k-2, \\
0 &= \frac{\partial n_{k-1}}{\partial t} = C_{k-2}\, N\, n_{k-2} - C_{k-1}\, N\, n_{k-1} - W_{k-1}\, n_{k-1}\,, \\
0 &= \frac{\partial n_k}{\partial t} = C_{k-1}\, N\, n_{k-1} - C_k\, N\, n_k - W_k\, n_k\,, \\
0 &= \frac{\partial N}{\partial t} = g - W_f\, N - \sum_{m=0}^{k} C_m\, N\, n_m + \sum_{m=2}^{k} W_m\, n_m\,.
\end{aligned}\right\} \quad \text{(A.1)}$$

If we define a matrix P as

$$P = \begin{bmatrix}
d_o & e_1 & 0 & W_3 & 0 & \cdots & \cdots & 0 \\
0 & d_1 & e_2 & 0 & W_4 & \cdot & & \cdot \\
\cdot & \cdot & \cdot & \cdot & \cdot & \cdot & \cdot & \cdot \\
\cdot & & \cdot & \cdot & \cdot & \cdot & \cdot & 0 \\
\cdot & & & \cdot & d_{k-3} & e_{k-2} & 0 & W_k \\
\cdot & & & & & d_{k-2} & e_{k-1} & 0 \\
0 & \cdots & \cdots & \cdots & \cdots & 0 & d_{k-1} & e_k \\
d_o & d_1 & d_2-W_2 & \cdots & \cdots & \cdots & \cdots & d_k-W_k
\end{bmatrix}, \quad \text{(A.2)}$$

Eq. (A.1) is reduced to

$$P \begin{pmatrix} n \\ \cdot \\ \cdot \\ \cdot \\ n_{k-1} \\ n_k \end{pmatrix} = \begin{pmatrix} 0 \\ \cdot \\ \cdot \\ \cdot \\ 0 \\ G \end{pmatrix}, \quad \text{(A.3)}$$

where $d_m = C_m N$, $e_m = -(d_m + W_m)$ and $G = g - W_f N$. From Eq.(A.3), n_m is given as a function of N by

$$n_m = \frac{G}{|P|}\Big[\{ d_o d_1 \cdots\cdots d_{m-1}(d_{m+1}+W_{m+1}) \cdots\cdots\cdots\cdots\cdots\cdots (d_k+W_k) \}$$
$$-\{ d_o d_1 \cdots\cdots d_{m-1}(d_{m+1}+W_{m+1}) \cdots\cdots\cdots (d_{k-3}+W_{k-3}) d_{k-2} d_{k-1} W_k \}$$
$$-\{ d_o d_1 \cdots\cdots d_{m-1}(d_{m+1}+W_{m+1}) \cdots (d_{k-4}+W_{k-4}) d_{k-3} d_{k-2} W_{k-1} (d_k+W_k) \}$$
$$-\{ d_o d_1 \cdots\cdots d_{m-1}(d_{m+1}+W_{m+1}) \cdots (d_{k-5}+W_{k-5}) d_{k-4} d_{k-3} W_{k-2} (d_{k-1}+W_{k-1}) (d_k+W_k) \}$$
$$- \cdots\cdots\cdots \Big] \qquad \text{for} \quad m \leq k-2 \quad , \tag{A.4}$$

and also we have

$$n_{k-1} = \frac{G}{|P|} d_o d_1 \cdots\cdots\cdots d_{k-2}(d_k+W_k) \quad , \tag{A.5}$$

$$n_k = \frac{G}{|P|} d_o d_1 \cdots\cdots\cdots d_{k-1} \quad , \tag{A.6}$$

where $|P|$ indicates the determinant of the matrix P.

Here, in the case of $d_m = C_m N >> W_m$ the first term $\{ d_o d_1 \cdots\cdots d_{m-1}(d_{m+1}+W_{m+1}) \cdots\cdots (d_k+W_k) \}$ in the square bracket of eq.(A.4) dominates over the other terms because the first term is the order of k in N while other terms the order of k-1 in N. On the other hand, if $W_m >> d_m$, the first term is sufficiently large compared with the remaining terms since the first term is the oder of k-m in W, two orders larger than the remaining terms. Therefore n_m is generally apporoximated by

$$n_m \simeq \frac{G}{|P|} d_o d_1 \cdots\cdots d_{m-1}(d_{m+1}+W_{m+1}) \cdots\cdots\cdots (d_k+W_k) \qquad \text{for} \quad 1 \leq m \leq k-2 \ . \tag{A.7}$$

From Eqs.(A.5), (A.6) and (A.7), we obtain

$$\frac{n_m}{n_{m+1}} = \frac{d_{m+1} + W_{m+1}}{d_m} = \frac{W_{m+1}}{C_m}\frac{1}{N} + \frac{C_{m+1}}{C_m} \qquad \text{for} \quad 1 \leq m \leq k-1, \tag{A.8}$$

which is identical to Eq. (3.7).

REFERENCES

1. *Excitons at High Density*, ed. by H. Haken and S. Nikitine (Springer, Berlin, Heidelberg, New York, 1975).
2. L. V. Keldysh, *Proc. Int. Conf. Phys. Semicond, Moscow* (1968) p1303.
3. T. M. Rice, in *Solid State Physics*, ed. by H. Ehrenreich, D. Turnbul and F. Seitz. (Academic Press, New York, San Francisco, London,1977)Vol.32 p.1
4. J. C. Hensel, T. G. Philips and G. A. Thomas, ibid p.88
5 N. F. Mott, *Metal-Insulator Transitions* (Barnes and Nobles, New York, 1974).
6. G. A. Thomas, J. B. Mock and M. Capizzi, Phys. Rev. B18 (1978) 4250
7. A. S. Kaminskii and Ya. E. Pokrovskii, Zh. eksper. teor. Fiz. Pis. Red. 11 (1970) 381, translation: Soviet Physics - JETP Letters. 11 (1970) 255.
8. Ya. E. Pokrovskii, Phys. Status solidi (a) 11 (1972) 385.
9. P. J. Dean, D. C. Herbert, D. Bimberg and W. J. Choyke, *Proc. Int. Conf. Phys. Semicond., Rome* (1976) p. 1298.
10. P. J. Dean, D. C. Herbert, D. Bimberg and W. J. Choyke, Phys. Rev. Letters 37 (1976) 1635.
11. S. A. Lyon, D. L. Smith and T. C. McGill, Phys. Rev. Letters 41 (1978) 56.
12. R. Sauer and J. Weber, Phys. Rev. Letters 36 (1976) 48.
13. R. Sauer and J. Weber, Phys. Rev. Letters 39 (1977) 770.
14. M. L. W. Thewalt, J. A. Rostoworowski and G. Kirczenow, Canad. J. Phys. 57 (1979) 1898.
15. G. Kirczenow, Solid State Commun. 21 (1977) 713, Canad. J. Phys. 55 (1977) 1787.
16. H. - J. Wünsche, K. Henneberger and V. E. Khartsiev, Phys. Status solidi (b) 86 (1978) 505.

17. H. - J. Wünsche, K. Henneberger, V. E.Khartsiev, *Proc. Int. Conf. Phys. Semicond., Edinburgh* (1978) p. 615.

18. H. B. Shore and R. S. Pfeiffer, *Proc. Int. Conf. Phys. Semicond., Edinburgh* (1978) p. 627.

19. H. B. Shore and R. S. Pfeiffer, *Proc. Int. Conf. Phys. Semicond., Kyoto* (1980) p. 453.

20. H. Nakayama, K. Ohnishi, H. Sawada, T. Nishino and Y. Hamakawa, J. Phys. Soc. Japan 46 (1979) 553.

21. K. Ohnishi, H. Nakayama, T. Nishino and Y. Hamakawa, J. Phys. Soc. Japan 49 (1980) 1078.

22. H. Nakayama, T. Nishino and Y. Hamakawa, *Proc. Int. Conf. Phys. Semicond., Kyoto* (1980) p. 469.

23. A. J. R. de Kock, *Proc. Int. Conf. Phys. Semicond., Edinburgh* (1978) p. 103.

24. A. J. R. de Kock, Festkörperprobleme XVI (1976) 179.

25. H. J. Queisser, Appl. Phys. 10 (1976) 275.

26. A. M. White, *Proc. Int. Conf. Phys. Semicond., Edinburgh* (1978) p.123

27. H. Nakayama, T. Nishino and Y. Hamakawa, Jpn. J. Appl. Phys. 19 (1980) 501.

28. K. Yasutake, M. Umeno, H. Kawabe, H. Nakayama, T. Nishino and Y. Hamakawa, Jpn. J. Appl. Phys. 19 (1980) L544.

29. H. Nakayama, J. Katsura, T. Nishino and Y. Hamakawa, Jpn. J. Appl. Phys. 19 (1980) L547.

30. T. Nishino, H. Nakayama, J. Katsura and Y. Hamakawa, to be presented at SPIE Conf. on Optical Characterization Techniques for Semiconductor Technology, San Jose, 1981.

31. C. S. Fuller, J. A. Ditzenberger, N. B. Hannay and E. Buhler, Phys. Rev. 96 (1954) 833.

32. W. Kaiser, H. L. Frish and H. Reiss, Phys. Rev. 112 (1958) 1546.

33. R. S. Knox, *Theory of Excitons*, Solid State Physics, ed. by F. Seitz and D. Turnball, Suppl. 5 (Academic Press, New York, 1963).

34. J. O. Dimmock, *Semiconductors and Semimetals*, Vol. 3, ed. by R. K. Willardson and A. C. Beer (Academic Press, New York, 1967) p. 259.

35. *Polarons and Excitons*, ed. by G. C. Kuper and G. D. Whitefield (Oliver and boyd, Plenum Press, New York, 1963).

36. K. L. Shaklee and R. E. Nahory, Phys. Rev. Letters 24 (1970) 942.

37. K. Cho, in *Excitons*, ed. by K. Cho (Springer-Verlag, Berlin, Heidelberg, New York, 1979) p. 1, 15.

38. K. Cho, S. Suga, W. Dreybrodt and F. Willman, Phys. Rev. B 11 (1975) 1512.

39. R. B. Hammond, D. L. Smith and T. C. McGill, Phys. Rev. Letters 35 (1975) 1535.

40. D. L. Smith and T. C. McGill, Phys. Rev. B 14 (1976) 2448.

41. I. Balslev, Solid State Commun. 23 (1977) 205.

42. R. B. Hammond and R. N. Silver, Solid State Commun. 28 (1978) 993.

43. R. R. Parsons, U. O, Ziemelis and J. A. Rostworowski, Solid State Commun. 31 (1979) 5.

44. N. O. Lipari and A. Baldereschi, Phys. Rev. B 3 (1971)) 2497.

45. N. O. Lipari and M. Altarelli, Phys. Rev. B 15 (1977) 4883.

46. M. A. Lampert, Phys. Rev. Letters 1 (1958) 450.

47. J. R. Haynes, Phys. Rev. Letters 4 (1960) 361.

48. P. J. Dean, J. R. Haynes and W. F. Flood, Phys. Rev. 161 (1967) 711.

49. P. J. Dean, W. F. Flood and G. Kaminsky, Phys. Rev. 163 (1967) 721.

50. R. J. Elliot, Phys. Rev. 108 (1957) 1384.

51. P. J. Dean, J. D. Cuthbert, D. G. Thomas and R. T. Lynch, Phys. Rev. Letters 18 (1967) 122.

52. P. J. Dean, J. R. Haynes and W. F. Flood, *Proc. Int. Conf. Localized Excitations in solids, Irvine* (plenum, New York, 1968) p. 276.

53. R. Sauer, J. Lumi. 12/13 (1976) 495.

54. M. L. W. Thewalt, Solid State Commun. 23 (1977) 733.

55. E. F. Gross, B. V. Novikov and N. S. Sokolov, Fizika Trerdogo Tela 14 (1972) 443, translation: Soviet Phys.-Solid State 14 (1972) 368.

56. A. E. Mayer and E. C. Lightowlers, *Proc. Int. Conf. Phys. Semicond., Kyoto* (1980) p. 441.

57. R. Sauer, Phys. Rev. Letters, 31 (1973) 376.

58. K. Kosai and M. Gershenzon, Phys. Rev. B 9 (1974) 723.

59. T. N. Morgan, *Proc. Int. Conf. Phys. Semicond., Rome* (1976) p. 825.

60. M. L. W. Thewalt, Solid State commun. 21 (1977) 937.

61. M. L. W. Thewalt, Phys. Rev. Letters 38 (1977) 521.

62. M. L. W. Thewalt, Canad. J. Phys. 55 (1977) 1463.

63 M. L. W. Thewalt, Solid State Commun. 25 (1978) 513.

64. M. L. W. Thewalt, Solid State Commun. 28 (1978) 361.

65. R. R. Parsons, Solid State Commun. 22 (1977) 671.

66. M. L. W. Thewalt and J. A. Rostoworowski, Phys. Rev. Letters 41 (1978) 808.

67. M. L. W. Thewalt, *Proc. Int. Conf. Phys. Semicond., Edinburgh* (1978) p.605.

68. R. Sauer, W. Schmid and Weber, Solid State Commun. 24 (1977) 507.

69. S. A. Lyon, D. L. Smith and T. C. McGill, Phys. Rev. B 17 (1978) 2620.

70. K. R. Elliot and T. C. McGill, Solid State Commun. 28 (1978) 491.

71. S. A. Lyon, D. L. Smith and T. C. McGill, Solid State Commun. 28 (1978) 317.

72. Y. C. Chang and T. C. McGill, Phys. Rev. Letters 45 (1980) 471.

73. W. Kohn and J. M. Luttinger, Phys. Rev. 98 (1955) 915.

74. R. L. Aggarwal, P. Fisher, V. Mourzine and A. K. Ramdas, Phys. Rev. 138 (1965) A882.

75. T. Nishino, H.Nakayama and Y. Hamakawa, J. Phys. Soc. Japan 43 (1977) 1807.

76 H. Nakayama, T. Nishino and Y. Hamakawa, J. Phys. Soc. Japan 44 (1978) 497.

77. Y. Shiraki and H. Nakashima, Solid State Commun. 29 (1979) 295.

78. K. Narita, ibid 29 (1979) 299.

79. R. R. Parsons, Solid State Commun. 29 (1979) 1.

80. G. A. Thomas, M. Cappizzi, F. DeRosa, R. N. Bhatt and T. M. Rice, to be published.

81. W. Schmid, Phys. Status solidi (b) 84 (1977) 529.

82. W. Schmid, Solid-State Electron. 21 (1978) 1285.

83. M. H. Pilkuhn, J. Lumi. 18/19 (1979) 81.

84. W. Schmid, Ph. D. thesis, Stuttgart University, Stuttgart, FRG, 1977.

85. M. Lax, Phys. Rev. 119 (1960) 1502.

86. A. T. Hunter, S. A. Lyon, D. L. Smith and T. C. McGill, Phys. Rev. B 20 (1979) 2431.

87. K. R. Elliott, D. L. Smith and T. C. McGill, Solid State Commun. 24 (1977) 461.

88. R. B. Hammond and R. N. Silver, Appl. Phys. Letters 36 (1980) 68.

89. G. Ascarelli and S. Rodriguez, Phys. Rev. 124 (1961) 1321.

90. Y. Toyozawa, Progr. theor. Phys. 20 (1980) 53.

91. Y. Toyozawa, Progr. theor. Phys. Suppl. 12 (1959) 111.

92. J. Bardeen and W. Shokley, Phys. Rev. 80 (1950) 102.

93. A. G. Milnes, *Deep Impurities in Semiconductors* (John Wiley and Sons, New York, 1973).

94. P. Blood and J. W. Orton, Rep. Prog. Phys. 41 (1978) 157.

95. M. Tajima, Jpn. J. Appl. Phys. 16 (1977) 2263, 2265; Appl. Phys. Letters 32 (1978) 719.

96. E. W. Williams and H. B. Bebb, in *Semiconductors and Semimetals* (Academic Press, New York, 1972) Vol. 8, p.284.

97. T. Nishino, M. Takada and Y, Hamakawa, Solid State Commun. 12 (1973) 1137.

98. M. L. W. Thewalt, G. Kirczenow, R. R. Parsons and R. Barrie, Canad. J. Phys. 54 (1976) 1728.

99. G. C. Osbourn and D. L. Smith, Phys. Rev. B 16 (1977) 5426.

100. G. C. Osbourn, S. A. Lyon, K. J. Elliot, D. L. Smith and T. C. McGill, Solid State Electron. 21 (1978) 1339.

101. P. Norton, T. Braggins and H. Levinstein, Phys. Rev. B 8 (1973) 8.

102. S. Kishino, Y. Matsushita and M. Kanamori, Appl. Phys. Letters 35 (1979) 213.

103. S. Kishino, M. Kanamori, N. Yoshihiro, M. Tajima and T. Iizuka, J. Apppl. Phys. 50 (1979) 8240.

104. S. Kishino, *Proc. Int. Conf. Phys. Semicond., Kyoto* (1980) p. 49.

105. S. T. Pantelides, Solid State Commun. 14 (1974) 1255.

106. D. Helmreich and E. Sirtl, in *Semiconductor Silicon 1977*, ed. by H. R. Huff and E. Sirtl (Electrochem. Soc., Princeton, 1977) p. 626.

107. P. Gaworzewski and K. Schmalz, Phys. Status. solidi (a) 55 (1979) 699.

108. W. Kaiser and P. H. Keck, J. Appl. Phys. 28 (1957) 882.

109. R. C. Newman and J. B. Willis, J. Phys. Chem. Solids 26 (1965) 373.

110. L. J. van der Pauw, Philips. Res. Repts. 16 (1961) 187.

111. V. N. Mordkovich, Fizika Trerdogo Tela 6 (1964) 847; translation: Soviet Phys.-Solid State 6 (1964) 654.

112. L. D. Partain, M. R. Lakshminarayana and G. J. Sullivan, Phys. Rev. B 12 (1980) 2432.

113. H. Fritsche, J. Phys. Chem. Solids 6 (1958) 69.

114. D. Wruck and P. Gaworzewski, Phys. Status solidi (a) 56 (1979) 557.

115. M. Tajima, A. Kanamori and T. Iizuka, Jpn. J. Appl. Phys. 18 (1979) 1401.

116. H. Nakayama, T. Nishino and Y. Hamakawa, to be published in Appl. Phys. Letters.

117. These values for γ_q are calculated as $10^{21}(C_o/W_1)[M_{bx}(q)]^2$ in the unit of $cm^3(h/A)^2$, where the values of C_o and W_1 are presented in Tables II and III. $M_{bx}(q)$ is the transition matrix element of radiative BE recombination with an emission of phonon q, the value of which is also shown in Table V.

118. G. S. Michard, S. A. Lyon, K. R. Elliot and T. C. McGill, Solid State Commun. 29 (1979) 425.

119. F. A. Trumbore, M. Gershenzon and D. G. Thmas, Appl. Phys. Letters 9 (1966) 4.

120. P. J. Dean and D. C. Herbert, in *Excitons*, ed. by K. Cho (Springer-Verlag, Berlin, Heidelberg, New York, 1979) p. 55.

121. R. A. Faulkner and J. J. Hopfield, *Proc. Int. Conf. Localized Excitations in Solids, Irvin* (Plenum, New York, 1968) p. 218.

122. P. J. Dean, J. Lumi. 7 (1973) 51.

123. A. Baldereschi, ibid 7 (1973) 79.

124. A. R. Bean and R. C. Newman, J. Phys. Chem. Solids 33 (1972) 255.

125. J. Weber, W. Schmid and R. Sauer, J. Lumi. 18/19 (1979) 93.

126. J. Weber, W. Schmid and R. Sauer, Phys. Rev. B 21 (1980) 2401.

139
46
5105